This manuscript is **a non-peer reviewed preprint submitted to EarthArXiv.** Subsequent versions of this manuscript may have slightly different content.

submitted to *Geophys. J. Int.*

The Effect of Rayleigh-Love Coupling in an Anisotropic Medium

Xiongwei Liu and Michael H. Ritzwoller,

Department of Physics, University of Colorado Boulder

SUMMARY

It is well known that for a weakly anisotropic medium, at angular frequency ω and propagation azimuth ψ Rayleigh and Love wave phase speeds are given approximately by $V(\omega, \psi) = A_0 + A_{2c} \cos 2\psi + A_{2s} \sin 2\psi + A_{4c} \cos 4\psi + A_{4s} \sin 4\psi$. Previous theories of the propagation of surface waves in anisotropic media based on non-degenerate perturbation theory predict that the dominant components are expected to be 2ψ for Rayleigh waves and 4ψ for Love waves. This paper is motivated by recent observations of previously unexpected anisotropy: the 2ψ component for Love waves and 4ψ for Rayleigh waves. To illuminate this phenomenon, we present a quasi-degenerate theory of Rayleigh-Love coupling based on the application of Hamilton's Principle to Rayleigh and Love waves propagating in a weakly anisotropic medium. We show that the unexpected components are actually expected in the presence of strong Rayleigh-Love coupling and recent observations of Rayleigh and Love wave 2ψ and 4ψ anisotropy can be fit successfully with physically plausible models of a depth-dependent tilted transversely isotropic (TTI) medium. In addition, the ellipticity parameter η_X, introduced here, is better constrained and we present evidence that the mantle should be modeled as a tilted orthorhombic medium rather than a TTI medium. We also provide information about the polarization of the quasi-Love waves, coupling between fundamental mode Love and overtone Rayleigh waves in both continental and oceanic settings, and practical suggestions for observers.

For comparison, we present a theory of SV-SH coupling for horizontally propagating body waves, with particular emphasis on results for a TTI medium.

Key words: Theoretical seismology; Seismic anisotropy; Body waves; Surface waves and free oscillations

1 INTRODUCTION

Based on non-degenerate perturbation theory, Smith & Dahlen (1973) showed that the azimuthal variation of Rayleigh and Love wave phase and group speeds at angular frequency ω in a slightly anisotropic medium is of the well-known form

$$V(\psi) = A_0 + A_{2c}\cos 2\psi + A_{2s}\sin 2\psi + A_{4c}\cos 4\psi + A_{4s}\sin 4\psi \tag{1.1}$$

where ψ is the azimuth of propagation. They also provided expressions for the sensitivity of each of the coefficients in this expansion to the depth dependence of 13 independent elastic parameters. They argued that the azimuthal dependence of Rayleigh wave speeds will be dominated by the 2ψ terms in equation (1.1), whereas the Love wave phase speeds will be dominated by the 4ψ terms. In non-degenerate perturbation theory, the Rayleigh and Love waves propagate independently and do not couple. Therefore, according to this theory the polarization of the quasi-Rayleigh and quasi-Love waves in the anisotropic medium is unchanged by anisotropy. Following Smith & Dahlen (1973), Montagner & Nataf (1986) presented straightforward integral expressions for each of the coefficients in equation (1.1) to be used to invert observations of the coefficients as a function of frequency for the depth-dependent components of the elastic tensor.

The aforementioned studies have strongly influenced the subsequent observation and interpretation of surface wave anisotropy. In particular, focus has been placed on observing and interpreting the 2ψ component of Rayleigh wave anisotropy and to a lesser extent the 4ψ component of Love wave anisotropy. Many studies have presented and interpreted the 2ψ component of Rayleigh wave anisotropy, dating back to the mid-1970s (e.g. Forsyth 1975; Tanimoto & Anderson 1985; Montagner & Jobert 1988; Nishimura and Forsyth 1988, etc) and more recently many recent studies have been presented based on ambient noise observations (e.g. Yao *et al*. 2010; Lin *et al*. 2011, etc). Observations of the 4ψ component of Love wave anisotropy are much more rare (e.g. Montagner & Tanimoto 1990; Trampert & Woodhouse 2003; Russell *et al*. 2019). Much less effort has been devoted to the study of the 2ψ component of Love wave anisotropy or the 4ψ component of Rayleigh wave anisotropy. We refer to the 2ψ component for Rayleigh waves and the 4ψ component for Love waves as "ex-

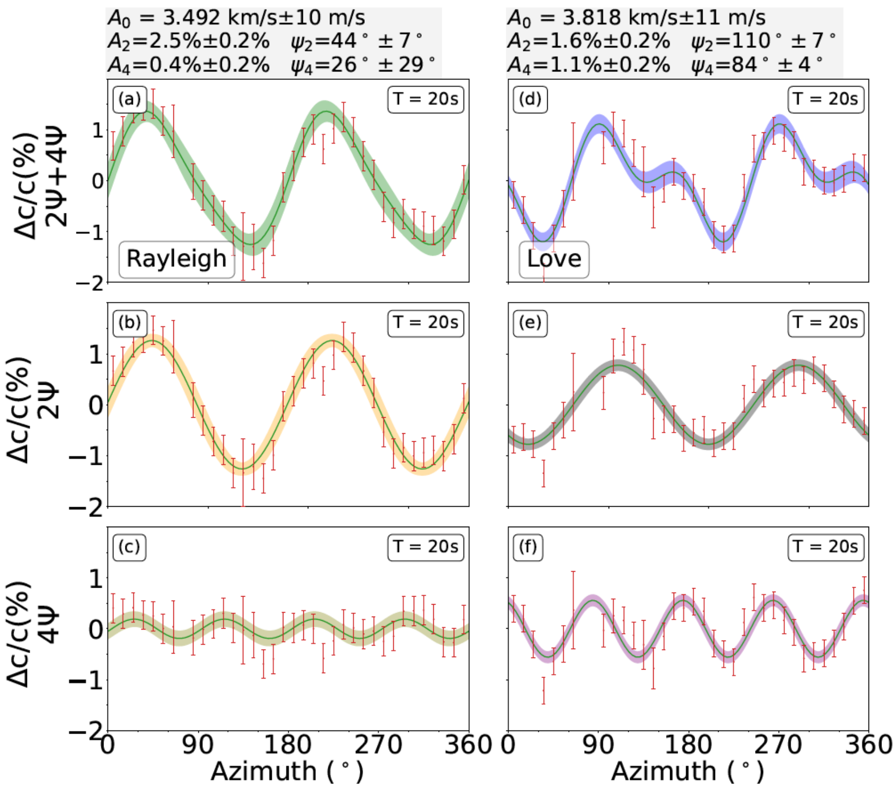

Figure 1. Observations of azimuthal anisotropy for the 20 s Rayleigh (left column) and Love (right column) waves based on ambient noise observations in western Alaska (64°N, 159°W, Data Source 4). Total azimuthal variation is shown in the top row and 2ψ and 4ψ variations are shown in the middle and bottom rows, respectively. The series $V(\psi) = A_0 + A_2\cos(\psi - \psi_2) + A_4\cos(\psi - \psi_4)$ is fit to the total variation, and fit values with uncertainties are presented at the top of each column. Errors bars are 1σ variations in each of the 36 azimuthal bins.

pected" anisotropy, according to non-degenerate perturbation theory. Similarly, the 4ψ component for Rayleigh waves and the 2ψ component for Love waves are referred to here as "unexpected".

Based on ambient noise data, a recent study in an oceanic setting presented strong evidence for the observation of unexpected anisotropy (Russell *et al*. 2019). They show that the 2ψ component of Love wave anisotropy is observable and is commensurate in amplitude with the 4ψ component of Love wave anisotropy and the 2ψ component of Rayleigh wave anisotropy, at least at short periods. Broader band ambient noise methods are also being employed in a continental setting based on eikonal tomography (Lin *et al*. 2009) to observe unexpected anisotropy. **Figure 1** presents an example for a point in western Alaska (X. Liu *et al*. 2024). Strong 2ψ Love wave anisotropy is observed at 20 s period as well as the weaker 4ψ component of Rayleigh wave anisotropy. As expected, the 2ψ component of the Rayleigh wave and the 4ψ component of the Love wave anisotropy are also observed at this point.

Such strong Love wave 2ψ and Rayleigh wave 4ψ anisotropy cannot be explained by the non-

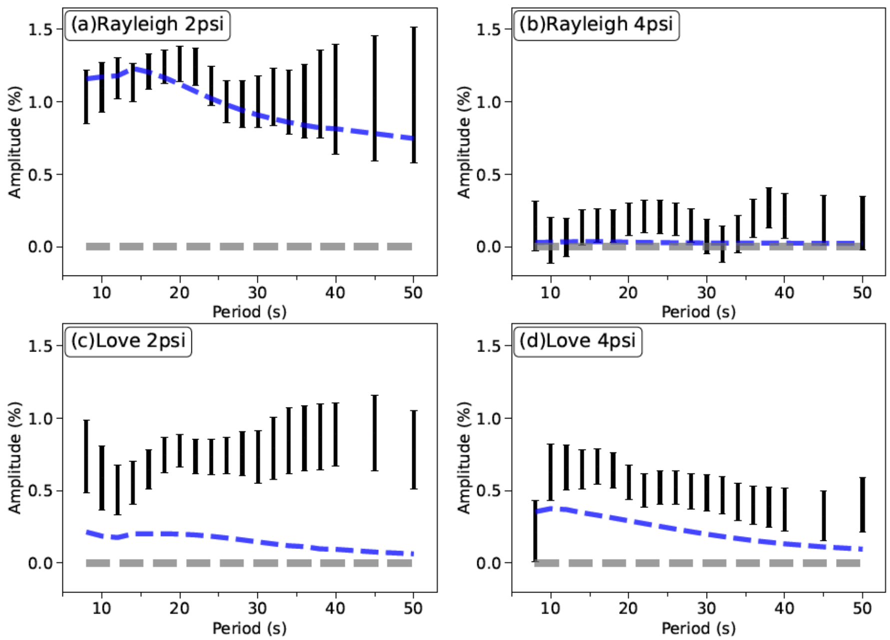

Figure 2. Comparison of observations of the amplitude of the 2ψ and 4ψ components of Rayleigh and Love wave anisotropy (black 1σ error bars) from 8 s to 50 s period at location (64°N, 159°W) in western Alaska with predictions using the elastic tensor model of the crust and uppermost mantle of C. Liu & Ritzwoller (2024), Data Source 2. Predictions (blue dashed lines) are computed using non-degenerate perturbation theory (Smith & Dahlen 1973; Montagner & Nataf 1986), which does not include Rayleigh-Love coupling. The amplitudes of the Love wave 2ψ observations are too large to be fit with non-degenerate perturbation theory.

degenerate perturbation theory applied by Smith & Dahlen (1973). **Figure 2** illustrates this by applying non-degenerate perturbation theory to the model of the depth-varying elastic tensor estimated by C. Liu & Ritzwoller (2024). C. Liu and Ritzwoller inverted these observations of the Rayleigh wave 2ψ component of anisotropy along with the isotropic components of both Rayleigh and Love waves for a tilted transversely isotropic (TTI) model of the crust and uppermost mantle. As expected, this model and theory predict the 2ψ component of Rayleigh wave anisotropy well but strongly under-predict the amplitude of the 2ψ component of Love wave anisotropy.

We argue in this paper that the unexpected signals arise from Rayleigh-Love coupling. Tanimoto (2004) presented an update to the theory of Smith & Dahlen (1973) based on a quasi-degeneracy condition that introduces Rayleigh-Love coupling. Formally, Tanimoto does not apply quasi-degenerate perturbation theory, but consistent with Maupin (1989) applies Hamilton's Principle valid for weak anisotropy based on the quasi-degeneracy condition that the Love and Rayleigh waves that couple have the same wavenumber but slightly different frequencies. The polarizations of the resulting quasi-Rayleigh and quasi-Love waves in an anisotropic medium are then superpositions of the polarizations in the reference medium ($\hat{\mathbf{a}}_R$, $\hat{\mathbf{a}}_L$):

$$\tilde{\mathbf{a}} = a_R \hat{\mathbf{a}}_R + a_L \hat{\mathbf{a}}_L \tag{1.2}$$

where a_L and a_R are coupling coefficients following the notation of Tanimoto (2004). Tanimoto (2004) set the coupling coefficients to be real and argued that the strength of coupling for realistic anisotropy in the Earth will be small. Therefore, his quasi-degenerate theory also is unable to explain observations of strong 2ψ Love wave or 4ψ Rayleigh wave anisotropy and types of anisotropy remained unexpected.

In this paper, we present a quasi-degenerate theory that does explain observations of strong 2ψ Love wave or 4ψ Rayleigh wave anisotropy. This renders them to be expected, although the 4ψ Rayleigh wave anisotropy is weaker than the others. We follow the methods of Tanimoto (2004), with the principal revision that the coupling coefficients are set to be complex because the polarization vectors are complex for surface waves and because, as we shall see, the vertical derivatives of the eigenfunctions add further complexity. As we show, this greatly enhances Rayleigh-Love coupling and allows observations, such as those presented in **Figure 1**, to be fit with physically plausible models of the depth-variation of the elastic tensor.

The data sources we use for examples and computations are described in section 2. Because of their similarity, the theoretical preliminaries for both body waves and surface waves are presented together in section 3. Like Smith & Dahlen (1973), for purposes of comparison and to provide guidance about interpreting the surface wave results, we reproduce results for horizontally propagating body waves in an infinite, homogeneous anisotropic medium. To further tighten the comparison between the body wave and surface wave treatments, however, in section 4 we apply Hamilton's Principle based on a quasi-degeneracy condition to derive the body wave formalism, which models SV-SH coupling. We believe that this is the first time this approach has been taken, but the results are identical to those produced by the degenerate perturbation theory of Jech & Pšenčík (1989). In section 5, we then present expressions for the phase speeds and polarizations of coupled Rayleigh and Love waves and use them in section 6 to show that the simultaneous observation of expected and unexpected anisotropy can be fit with physically plausible models of the depth-dependent elastic tensor. We also highlight new information that results from using Love wave 2ψ and 4ψ and Rayleigh wave 4ψ observations in the inversion and discuss several other issues in section 6. These include evidence that a tilted orthorhombic elastic tensor in the mantle should be used in place of the TTI elastic tensor, differences in the nature of Rayleigh-Love coupling in oceanic and continental settings with focus on the role of overtones, and the utility of polarization measurements for quasi-Love waves to constrain anisotropy, which was a point emphasized by Tanimoto (2004). Finally, we discuss expected differences between measurements of the various fast directions (Rayleigh 2ψ, 4ψ and Love 2ψ, 4ψ) to provide guidance for observers. Principal derivations are presented in the supplementary materials.

2 DATA SOURCES

Four different data compilations or models are used here for computation and inversion, as examples of the effect of anisotropy on body wave and surface wave speeds and polarizations.

Data Source 1. We use the database of elastic tensor measurements of crustal rocks presented by Brownlee *et al*. (2017). The full elastic tensor is presented in the database for 93 samples along with the vertical transversely isotropic (VTI) or effective transversely isotropic component (Browaeys & Chevrot 2004). The VTI component of the elastic tensor for sample #20 is shown in **Table 1**. We use the database primarily to present examples of body wave calculations.

Table 1. Transversely isotropic component of the elastic tensor from sample #20, Data Source 1.

A	C	N	L	F	η	η_K	η_X	ρ
159.6 GPa	143.7 GPa	47.5 GPa	43.2 GPa	62.0 GPa	0.85	0.97	0.97	3×10^3 kg/m^3

Data Source 2. We also use the model of the depth-dependent TTI elastic tensor in the crust and uppermost mantle at a location in western Alaska (64°N, 159°W), taken from C. Liu & Ritzwoller (2024), which is based on fitting only the isotropic Love and Rayleigh wave phase speed curves and 2ψ Rayleigh wave anisotropy. This model is used to present preliminary comparisons between surface wave observations and theoretic predictions.

Data Source 3. We use another model of the depth-dependent elastic tensor in the crust and uppermost mantle at a location in the central Pacific at the NoMelt ocean-bottom seismic array, taken from Russell *et al*. (2019). We revise this model and use it to compute the strength of Rayleigh-Love coupling in an oceanic setting.

Data Source 4. Finally, we use a new preliminary database of Rayleigh wave and Love wave 2ψ and 4ψ azimuthal phase speed variations measured across Alaska (X. Liu *et al*. 2024). We apply the data primarily at the same point in western Alaska (64°N, 159°W) as in Data Source 2 to perform a number of inversions with different data subsets and theories, but also produce a new model in eastern Alaska for comparison (64°N, 147°W). We make use of the resulting models to compute the strength of Rayleigh-Love coupling in a continental setting.

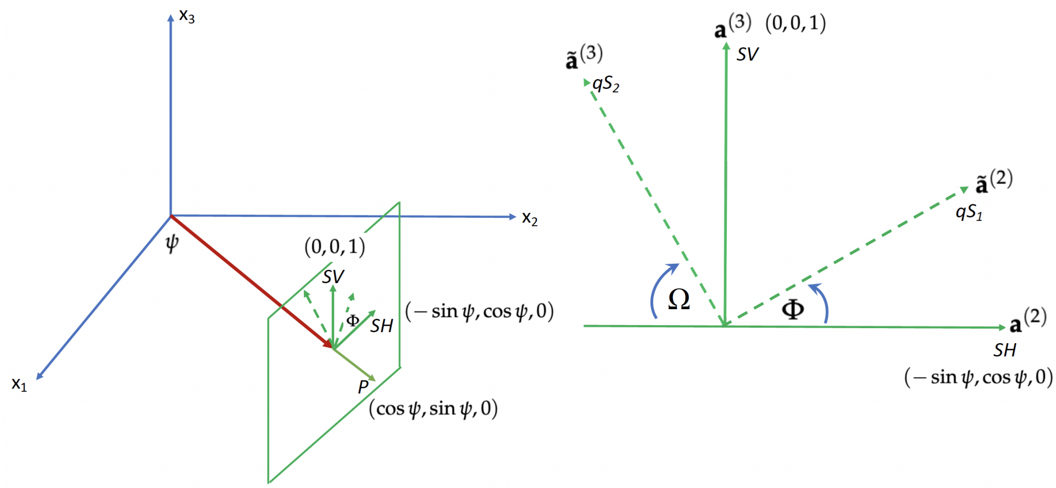

Figure 3. Geometry of horizontal body wave propagation in the direction defined by the azimuthal angle ψ relative to the x_1-axis, showing the waves in the reference isotropic medium, P, SH, and SV, as well as the quasi-S waves (${}_qS_1$, ${}_qS_2$) in the perturbed anisotropic medium. SV-SH coupling rotates the polarization of the quasi-shear waves through angle Φ in the plane perpendicular to the direction of propagation. We define Ω as the negative of the complement of Φ and x_2 is the "strike axis".

3 QUASI-DEGENERATE THEORY FOR BODY AND SURFACE WAVES

3.1 Polarization and displacement basis vectors

In Cartesian coordinates $(x_1, x_2, x_3) = (x, y, z)$, the plane wave displacement for horizontally propagating body waves at depth z can be written

$$\vec{\mathbf{u}}_{BW}(\vec{\mathbf{r}}, t) = A\hat{\mathbf{a}}e^{i(\vec{\mathbf{k}}\cdot\vec{\mathbf{r}}-\omega t)} \tag{3.1}$$

where $\hat{\mathbf{a}}$ is the direction of particle motion or the polarization vector, the components of the position vector $\vec{\mathbf{r}}$ are x_i $\left((x_1, x_2, x_3)^T = (x, y, z)^T\right)$ and of the horizontal wavenumber vector $\vec{\mathbf{k}}$ are $\omega n_i/V$ where n_i is the unit vector in the direction of propagation (perpendicular to the wavefront) and V is the phase speed of the wave. Surface wave displacement can be written similarly as

$$\vec{\mathbf{u}}_{SW}(\vec{\mathbf{r}}, z, t) = A\hat{\mathbf{s}}(z)e^{i(\vec{\mathbf{k}}\cdot\vec{\mathbf{r}}-\omega t)} \tag{3.2}$$

where $z = 0$ is the free surface, surface location $\vec{\mathbf{r}} = (x, y, 0)^T$, and $\hat{\mathbf{s}}(z)$ is the vector displacement eigenfunction.

We set the basis vectors for body waves propagating horizontally at azimuth ψ relative to the x-axis to be in the the direction of motion for P, vertical for SV, and perpendicular to both P and SV

for SH, as depicted in **Figure 3**. Therefore the polarization basis vectors are

$$\begin{aligned}
\hat{\mathbf{a}}_P(\vec{\mathbf{r}},t) &= \hat{\mathbf{a}}^{(1)} = (\cos\psi, \sin\psi, 0)^T && (3.3)\\
\hat{\mathbf{a}}_{SH}(\vec{\mathbf{r}},t) &= \hat{\mathbf{a}}^{(2)} = (-\sin\psi, \cos\psi, 0)^T && (3.4)\\
\hat{\mathbf{a}}_{SV}(\vec{\mathbf{r}},t) &= \hat{\mathbf{a}}^{(3)} = (0, 0, 1)^T && (3.5)
\end{aligned}$$

which we denote with the overscript $\hat{}$ and T means transpose. The displacement vectors in the reference medium are

$$\begin{aligned}
\hat{\mathbf{u}}_P(\vec{\mathbf{r}},t) &= \hat{\mathbf{a}}^{(1)} f(\vec{\mathbf{r}},t) && (3.6)\\
\hat{\mathbf{u}}_{SH}(\vec{\mathbf{r}},t) &= \hat{\mathbf{a}}^{(2)} f(\vec{\mathbf{r}},t) && (3.7)\\
\hat{\mathbf{u}}_{SV}(\vec{\mathbf{r}},t) &= \hat{\mathbf{a}}^{(3)} f(\vec{\mathbf{r}},t) && (3.8)
\end{aligned}$$

which we also denote with an overscript $\hat{}$. The propagation term for horizontal propagation is

$$f(\vec{\mathbf{r}},t) = \exp\left[i(\vec{\mathbf{k}}\cdot\vec{\mathbf{r}} - \omega t)\right] = \exp\left[i(k(x\cos\psi + y\sin\psi) - \omega t)\right] \tag{3.9}$$

where phase speed $V = \omega/k$. The S-wave basis vectors could be in any pair of orthogonal directions in the vertical plane perpendicular to the direction of travel of the wave, but we choose the horizontal (transverse) and vertical directions for simplicity.

Similarly, the basis vectors for surface wave displacement in the reference medium are Rayleigh and Love waves in a laterally homogeneous medium for a wave propagating at azimuth ψ. The polarization vectors are

$$\begin{aligned}
\hat{\mathbf{a}}_R(\vec{\mathbf{r}},z,t) &= \left[(\cos\psi, \sin\psi, 0)^T V(z) + (0, 0, i)^T U(z)\right] && (3.10)\\
\hat{\mathbf{a}}_L(\vec{\mathbf{r}},z,t) &= (-\sin\psi, \cos\psi, 0)^T W(z) && (3.11)
\end{aligned}$$

with displacement vectors

$$\begin{aligned}
\hat{\mathbf{u}}_R(\vec{\mathbf{r}},z,t) &= \hat{\mathbf{a}}_R(\vec{\mathbf{r}},z,t) f(\vec{\mathbf{r}},t) && (3.12)\\
\hat{\mathbf{u}}_L(\vec{\mathbf{r}},z,t) &= \hat{\mathbf{a}}_L(\vec{\mathbf{r}},z,t) f(\vec{\mathbf{r}},t) && (3.13)
\end{aligned}$$

$U(z)$ and $V(z)$ are the vertical and horizontal (radial) displacement eigenfunctions for Rayleigh waves and $W(z)$ is the Love wave horizontal (transverse) eigenfunction, which are normalized as follows

$$\begin{aligned}
1 &= \int_0^\infty \rho(z) W^2(z) dz && (3.14)\\
1 &= \int_0^\infty \rho(z) \left(U^2(z) + V^2(z)\right) dz && (3.15)
\end{aligned}$$

Example eigenfunctions are plotted later, in **Figure 10a**.

3.2 Coupling caused by anisotropy

In anisotropic media, the displacement of the resulting waves will be a mixture of the displacements of the basis vectors. P, SV, and SH waves will couple to produce a quasi-P wave ($_qP$) and two quasi-S waves ($_qS_1, {}_qS_2$) and Rayleigh and Love waves will couple to produce quasi-Love and quasi-Rayleigh waves ($_qL, {}_qR$).

For body waves with general coupling between P, SH, and SV, the polarization vectors in the perturbed (anisotropic) medium would be written

$$qP : \tilde{\mathbf{a}}^{(1)} = a_{11}\hat{\mathbf{a}}^{(1)} + a_{12}\hat{\mathbf{a}}^{(2)} + a_{13}\hat{\mathbf{a}}^{(3)} \tag{3.16}$$

$$qS_1 : \tilde{\mathbf{a}}^{(2)} = a_{21}\hat{\mathbf{a}}^{(1)} + a_{22}\hat{\mathbf{a}}^{(2)} + a_{23}\hat{\mathbf{a}}^{(3)} \tag{3.17}$$

$$S_2 : \tilde{\mathbf{a}}^{(3)} = a_{31}\hat{\mathbf{a}}^{(1)} + a_{32}\hat{\mathbf{a}}^{(2)} + a_{33}\hat{\mathbf{a}}^{(3)} \tag{3.18}$$

We denote quantities in the perturbed medium with an overscript $\tilde{}$. Because the basis vectors for body waves are real and depth-independent, the expansion coefficients a_{ij} are also real; i.e., $a_{ij} \in \mathbb{R}$.

In real Earth media, the quasi-P wave phase speed is much more different from the two quasi-S wave speeds than they are from one another. Thus, we consider only coupling between the SH and SV waves and will ignore the weaker coupling between P and SV and SH. Thus, we set $a_{11} = 1$ and $a_{12} = a_{21} = a_{13} = a_{31} = 0$. Therefore

$$qP : \tilde{\mathbf{a}}^{(1)} = \hat{\mathbf{a}}^{(1)} \tag{3.19}$$

$$qS_1 : \tilde{\mathbf{a}}^{(2)} = a_{SH}\hat{\mathbf{a}}^{(2)} + a_{SV}\hat{\mathbf{a}}^{(3)} = \cos\Phi\hat{\mathbf{a}}^{(2)} + \sin\Phi\hat{\mathbf{a}}^{(3)} \tag{3.20}$$

$$qS_2 : \tilde{\mathbf{a}}^{(3)} = -a_{23}\hat{\mathbf{a}}^{(2)} + a_{33}\hat{\mathbf{a}}^{(3)} = -a_{SV}\hat{\mathbf{a}}^{(2)} + a_{SH}\hat{\mathbf{a}}^{(3)} = -\sin\Phi\hat{\mathbf{a}}^{(2)} + \cos\Phi\hat{\mathbf{a}}^{(3)} \tag{3.21}$$

where we have introduced notation for the expansion coefficients a_{SH} and a_{SV}, such that $a_{SH}^2 + a_{SV}^2 = 1$. The second equalities in the latter two equations follow from the fact that the relationship between the polarizations of the quasi-S waves and the S waves in the reference medium is a rotation through polarization angle Φ, as **Figure 3** illustrates. Thus, $a_{22} = \cos\Phi, a_{23} = \sin\Phi, a_{32} = -\sin\Phi$, and $a_{33} = \cos\Phi$, where Φ is the angle between the reference SH polarization vector and the polarization vector for quasi-S_1. It is also the angle from the reference SV polarization vector and the polarization vector for quasi-S_2. To find the polarizations of the quasi-S waves we need only find Φ.

Body wave displacement associated with the perturbed polarizations in equations (3.19) - (3.21) is

$$\tilde{\mathbf{u}}^{(m)} = \tilde{\mathbf{a}}^{(m)} f \tag{3.22}$$

By solving the Christoffel equation (section 4) numerically, we can compute the effect of coupling the quasi-S waves to the quasi-P wave exactly, as illustrated in **Figure 4**. This shows that for the rock samples in the elastic tensor database of Brownlee *et al*. (2017), the average maximum tilt out of the

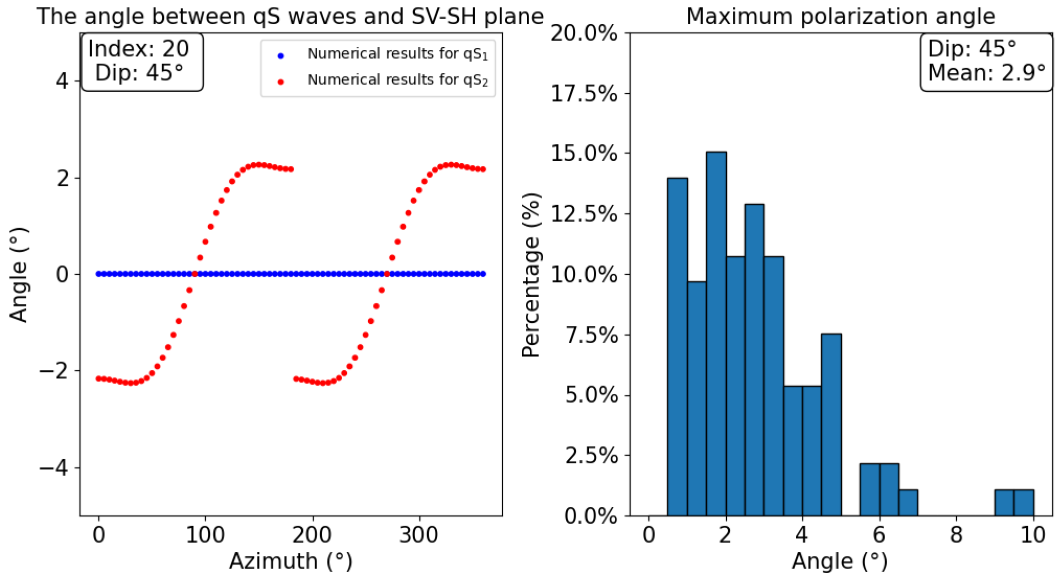

Figure 4. Numerical (non-approximate) computation of the coupling with the quasi P-wave on the polarizations of the two quasi-S waves. (a) Deflection of the quasi-S_1 and quasi-S_2 eigenvectors out of the vertical plane due to coupling to the quasi-P wave, presented as a function of azimuth of propagation. Result is for the transversely isotropic component of sample #20 from the elastic tensor database in Data Source 1, tilted through a dip angle $\theta = 45°$, which produces the strongest coupling to the P-wave. In this sample, the maximum effect is about $2°$ for quasi-S_2, with no effect on quasi-S_1. (b) Histogram of maximum out of vertical plane tilt angles for the quasi-S_2 polarizations for all 93 samples in Data Source 1 tilted by a dip angle $\theta = 45°$. The mean maximum deflection is about $3°$.

vertical plane of the eigenvector for the quasi-S_2 wave is about $3°$. The eigenvector of the quasi-S_1 wave is unaffected by coupling to the quasi-P wave.

For surface waves, the displacement for the fundamental mode in an anisotropic medium is a superposition of all modes in the reference medium. The theory we present can be applied based on any reference medium, but for simplicity we choose a VTI medium as the reference, including Rayleigh and Love waves, fundamental and overtone modes. Here, we reduce the superposition to only two modes, a Rayleigh mode and a Love mode. We focus on fundamental modes but any pair of Rayleigh and Love modes could be used in the theory we present. In this case, displacement in an anisotropic medium is the following superposition

$$\tilde{\mathbf{u}} = a_R \hat{\mathbf{u}}_R + a_L \hat{\mathbf{u}}_L \tag{3.23}$$

The expansion coefficients a_R and a_L define the Rayleigh-Love coupling and are complex mainly because the basis vectors are complex: $a_R, a_L \in \mathbb{C}$, such that $a_L a_L^* + a_R a_R^* = 1$. Tanimoto (2004) set a_R and a_L to be real, which, as we discuss below, typically yields very weak Rayleigh-Love coupling.

Therefore, the fundamental mode displacement in an anisotropic medium for a wave propagating

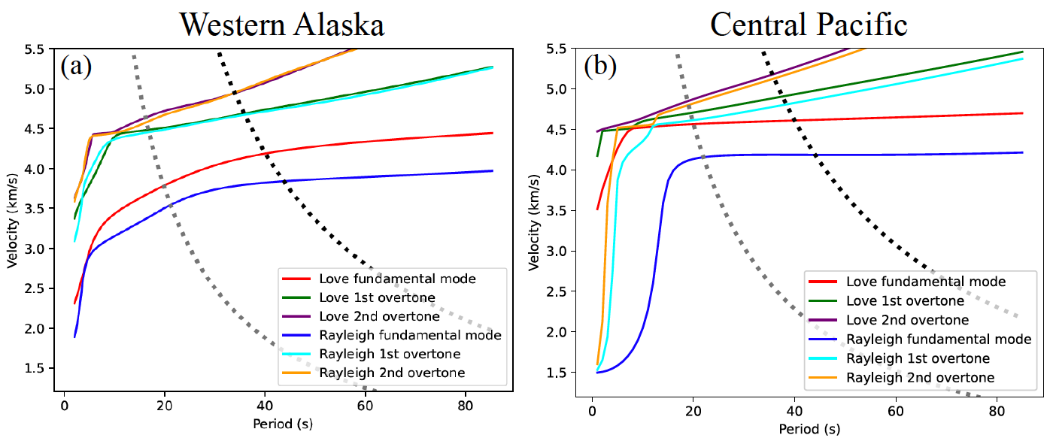

Figure 5. Phase speed curves for Rayleigh and Love wave fundamental modes and first two overtone modes for a continental and an oceanic transversely isotropic model, illustrating the quasi-degeneracy condition. (a) Produced using the transversely isotropic component of the 1D model from Data Source 2, at (64°N, 159°W) in western Alaska. (b) Produced using the transversely isotropic component of the 1D model from Data Source 3, southeast of Hawaii in the central Pacific. The dashed lines are lines of constant wavenumber passing through the fundamental Love wave phase speed curve at periods of 20 s and 40 s. Under the quasi-degeneracy condition, modes couple along these lines.

at azimuth ψ is:

$$\tilde{\mathbf{u}}(\vec{\mathbf{r}}, z, t) = \left(a_R V(z) \cos\psi - a_L W(z) \sin\psi, a_R V(z) \sin\psi + a_L W(z) \cos\psi, i a_R U(z)\right)^T f(\vec{\mathbf{r}}, t) \tag{3.24}$$

3.3 Quasi-Degeneracy

Under the quasi-degeneracy condition, waves and modes are coupled that have the same wavenumber k, but the resulting waves and modes will have slightly different frequencies ω and phase speeds V. For slight anisotropy, the frequencies will be similar but not identical, which is why this is referred to as a quasi-degeneracy approximation, or in the context of perturbation theory as "quasi-degenerate perturbation theory". The quasi-degeneracy condition is illustrated in **Figure 5** for surface waves, presenting dashed lines with common k values linking potentially coupling modes. In particular, the figure illustrates which quasi-degenerate Rayleigh and Love modes will couple under this assumption for the Love wave at periods of 20 s and 40 s.

3.4 The Lagrangian and Hamilton's Principle

For a linear elastic body, the Lagrangian density is the difference between the kinetic energy and elastic strain energy, which for body and surface waves, respectively, are given by

$$L_{BW}(\dot{u}_i, u_{i,j}) = T_{BW} - V_{BW} = \frac{1}{2}\omega^2 \rho u_i u_i^* - \frac{1}{2} c_{ijkl}\epsilon_{ij}\epsilon_{kl}^* \tag{3.25}$$

$$L_{SW}(\dot{u}_i, u_{i,j}) = T_{SW} - V_{SW} = \frac{1}{2}\omega^2 \int_0^\infty \rho u_i u_i^* dz - \frac{1}{2}\int_0^\infty c_{ijkl}\epsilon_{ij}\epsilon_{kl}^* dz \tag{3.26}$$

where $c_{ijk\ell}$ is the elastic tensor, $\epsilon_{ij} = (u_{i,j} + u_{j,i})/2$, the subscript "$, j$" represents a spatial derivative in the x_j direction, and $*$ denotes complex conjugation. Displacement appears in equations (3.25) and (3.26) as a product with its complex conjugate, therefore because $ff^* = 1$ the propagation term f and all time-dependent terms disappear from further equations. For the anisotropic medium, u_i is replaced by $\tilde{u}_i$.

Expressions for T and V are derived in section 4.2 for body waves and Supplementary Materials section S.6 for surface waves.

In Supplementary Materials section S.5 we show that Hamilton's Principle implies that $\partial L/\partial a_{SH} = \partial L/\partial a_{SV} = 0$ for body waves and that $\partial L/\partial a_L = \partial L/\partial a_R = 0$ for surface waves. The latter for surface waves was first applied by Tanimoto (2004). Applying these derivatives results in an eigenvalue-eigenvector equation for the frequencies or phase speeds of the three quasi-body waves and two quasi-surface waves as well as their polarizations, which is the subject of sections 4 and 5.

4 THE EFFECT OF SV-SH COUPLING

Before considering Rayleigh-Love coupling for surface waves, as an analogy we consider SV-SH coupling for horizontally propagating body waves. One approach would be to apply non-degenerate perturbation theory like Jech & Pšenčík (1989). As discussed above, we apply Hamilton's Principle to the Lagrangian to be consistent with the approach we take for surface waves.

4.1 The Christoffel equation and non-degenerate perturbation theory

Before applying Hamilton's principle to SV-SH coupling, we review the application of non-degenerate perturbation theory to the Christoffel equation, which does not include SV-SH coupling. This solution provides a touchstone for the more accurate quasi-degenerate theory presented in subsequent sections.

The seismic equation of motion in Cartesian coordinates for a homogeneous anisotropic medium is

$$\rho \ddot{u}_i = c_{ijk\ell} u_{k,j\ell} \tag{4.1}$$

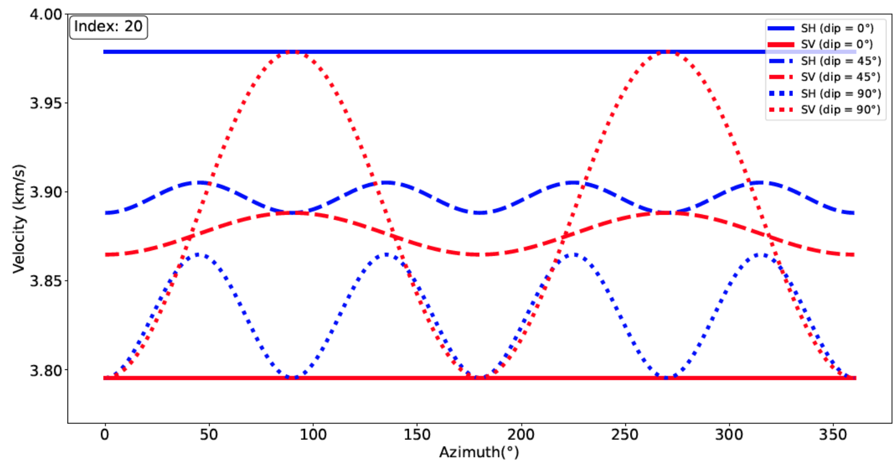

Figure 6. Azimuthal variation of phase speed from Rayleigh's Principle (or non-degenerate perturbation theory) assuming horizontal and vertical polarizations for the quasi-SH and quasi-SV waves, respectively. The transversely isotropic component of the elastic tensor index #20 from Data Source 1 is used (Table 1), where the symmetry axis is tilted through three different dip angles ($\theta = 0°$, VTI medium; $\theta = 45°$, TTI medium; $\theta = 90°$, HTI medium.)

where the summation convention is assumed. Substituting the equation of the displacement for a horizontally propagating body wave, equation (3.1), into (4.1) we get the Christoffel equation

$$M_{ik}a_k^{(m)} = V_{(m)}^2 \delta_{ik} a_k^{(m)} \tag{4.2}$$

where

$$\rho M_{ik} \equiv c_{ijk\ell} n_j n_\ell \tag{4.3}$$

and $m \in \{1, 2, 3\}$ is not subject to the summation convention. Each eigenvalue $V_{(m)}^2$ is the squared phase speed and each associated eigenvector $\tilde{\mathbf{a}}^{(m)}$ is the polarization of the m-th wave. We refer to M_{ik} as the Christoffel matrix, which can be visualized as the following symmetric matrix

$$\rho M_{ik} = \begin{bmatrix} c_{1j1\ell} n_j n_l & c_{1j2\ell} n_j n_l & c_{1j3\ell} n_j n_l \\ c_{2j1\ell} n_j n_l & c_{2j2\ell} n_j n_l & c_{2j3\ell} n_j n_l \\ c_{3j1\ell} n_j n_l & c_{3j2\ell} n_j n_l & c_{3j3\ell} n_j n_l \end{bmatrix} \tag{4.4}$$

The symmetry of M_{ik} guarantees that the eigenvalues are real and the eigenvectors form an orthogonal set.

Equation (4.2) can be solved directly numerically or analytically, for example with Mathematica, although the analytical solution can become quite messy. It can also be solved by approximate methods such as perturbation theory or the application of Hamilton's Principle to the Lagrangian, as we do here. It is valuable to compare the approximate solutions to the numerical solutions, such as in **Figure 4**.

Rayleigh's Principle states that the eigenvalues of a physical system are stationary relative to perturbations in the eigenvectors. This variational principle can be exploited to estimate the eigenvalues of the system by assuming approximate eigenvectors. Assuming the reference eigenvectors are in the direction of motion for P, vertical for SV, and perpendicular to both P and SV for SH, as depicted in **Figure 3**, the eigenvectors are given by equations (3.3) - (3.5). Contracting equation (4.2) with equations (3.3) - (3.5) gives the approximate phase speed of the quasi-P, quasi-SH, and quasi-SV waves:

$$\rho V_{qP}^2 = \mathcal{A} + B_c \cos 2\psi - B_s \sin 2\psi + E_c \cos 4\psi - E_s \sin 4\psi \tag{4.5}$$

$$\rho V_{qSH}^2 = \mathcal{N} - E_c \cos 4\psi + E_s \sin 4\psi \tag{4.6}$$

$$\rho V_{qSV}^2 = \mathcal{L} + G_c \cos 2\psi - G_s \sin 2\psi \tag{4.7}$$

where the coefficients are defined in Appendix B and the polarizations are fixed and equal to equations (3.3) - (3.5). The choice of different reference eigenvectors will produce different azimuthal distributions of phase speed. The choice of equations (3.3) - (3.5) motivates the terminology of quasi-SH and quasi-SV, as the polarizations associated with the phase speed distributions in equations (4.6) and (4.7) are assumed to be fixed. Backus (1965) applied Rayleigh's Principle to derive equation (4.5) for quasi-P. He applied degenerate perturbation theory for the quasi-S waves, which allows them to couple, but did not provide analytical expressions for the resulting quasi-S wave phase speed distributions with azimuth. Such expressions were provided by Jech & Pšenčík (1989).

Anisotropy lifts the degeneracy between the quasi-S wave speeds, so non-degenerate perturbation theory can also be applied (Jech & Pšenčík 1989). Non-degenerate perturbation theory is based on the assumption that the polarizations of the waves will be affected very little by anisotropy, the constituent waves are constrained to couple only weakly and do couple at all at first order, and the polarizations will be very close to equations (3.3) - (3.5). Thus, it produces the same results as Rayleigh's Principle, depending on the assumed orientations of the reference polarizations.

Under Rayleigh's Principle with polarizations given by equations (3.3) - (3.5), the quasi-P wave speeds display both 2ψ and 4ψ variability, but the quasi-SH shows only 4ψ and the quasi-SV only shows 2ψ variability. **Figure 6** presents phase speed as a function of azimuth for a transversely isotropic elastic tensor (**Table 1**) with a symmetry axis tilted through three dip angles (see Appendix A). These are: $\theta = 0°$ which has a vertical symmetry axis (VTI medium), $\theta = 45°$ which has a tilted symmetry axis (TTI medium), and $\theta = 90°$ which has a horizontal symmetry axis (HTI medium). For a VTI medium, there is no azimuthal anisotropy and quasi-SH and quasi-SV are strongly split. The amplitude of azimuthal anisotropy is increased systematically as dip angle increases, maximizing for a HTI medium.

For Rayleigh's Principle or non-degenerate perturbation theory to be accurate, the two quasi-S waves must have phase speeds that are much different from one another or they can couple to rotate the polarization vectors and modify their azimuthal variations. As **Figure 6** illustrates, degeneracies and near degeneracies between quasi-SH and quasi-SV occur, which may introduce SV-SH coupling, change the polarizations of the quasi-S waves, and revise their phase speed variation with azimuth. Modeling this behavior requires the application of a degenerate or quasi-degenerate theory, which is the subject of the rest of section 4.

4.2 Applying Hamilton's Principle

First, express the components of the Lagrangian density (eqn (3.25)) in index notation by using equations (3.1) for $\tilde{\mathbf{u}}$ and (3.20) for $\tilde{\mathbf{a}}$ expressed in index notation: $\tilde{u}_i^{(m)} = \tilde{a}_i^{(m)} f$ and $f = \exp(i(\omega n_i x_i/V - \omega t))$. Therefore, from equation (3.25) and temporarily suppressing the index m:

$$\begin{aligned} L(\dot{\tilde{u}}_i, \tilde{u}_{i,j}) &= \frac{1}{2}\rho\omega^2 \tilde{u}_i \tilde{u}_i^* - \frac{1}{2} c_{ijkl} \tilde{u}_{i,j} \tilde{u}_{k,l}^* = \frac{1}{2}\rho\omega^2 \tilde{u}_i \tilde{u}_i^* - \frac{1}{2} c_{ijkl} (k n_j \tilde{u}_i)(k n_l^* \tilde{u}_k^*) \\ &= \frac{1}{2}\rho\omega^2 \tilde{u}_i \tilde{u}_i^* - \frac{k^2}{2} \rho M_{ij} \tilde{u}_i \tilde{u}_k^* = \frac{1}{2}\rho\omega^2 \tilde{a}_i \tilde{a}_i - \frac{k^2}{2} \rho M_{ij} \tilde{a}_i \tilde{a}_k \end{aligned} \quad (4.8)$$

where $\rho M_{ik} = c_{ijkl} n_j n_l$ from equation (4.3), and $f f^* = 1$. We can replace $\epsilon_{ij}\epsilon_{kl}^*$ with $u_{i,j} u_{k,l}^*$ because of the symmetry $c_{ijk\ell} = c_{jik\ell} = c_{ij\ell k}$.

Here, we assume the quasi-P wave ($m = 1$) is uncoupled to the quasi-S waves, so the quasi-P wave solution is given by non-degenerate perturbation theory, equations (4.5) for phase speed and (3.19) for polarization.

To consider the coupled SV-SH waves, we start by considering the quasi-S$_1$ wave and setting $m = 2$ so

$$\tilde{a}_i^{(2)} = \alpha_2 \hat{a}_i^{(2)} + \alpha_3 \hat{a}_i^{(3)} \quad (4.9)$$

where $\alpha_2 = a_{SH} = \cos\Phi$ and $\alpha_3 = a_{SV} = \sin\Phi$. With $\hat{a}_i^{(2)}$ given by equation (3.4) and $\hat{a}_i^{(3)}$ by equation (3.5), we find

$$\tilde{a}_i^{(2)} \tilde{a}_i^{(2)} = \alpha_2^2 + \alpha_3^2 \quad (4.10)$$

$\alpha_2^2 + \alpha_3^2 = 1$, but we retain this term because of the partial derivatives to be computed later relative to α_2 and α_3.

For $\tilde{a}_i^{(2)} \tilde{a}_k^{(2)}$ in equation (4.8), we have

$$\tilde{a}_i^{(2)} \tilde{a}_k^{(2)} = \alpha_m \hat{a}_i^{(m)} \alpha_n \hat{a}_k^{(n)} \quad (4.11)$$

where there is no summation over m and n and both indices range over 2 and 3.

Defining

$$B_{mn} \equiv M_{ik} \hat{a}_i^{(m)} \hat{a}_k^{(n)} \quad (4.12)$$

we can rewrite the Lagrangian density as

$$L = \frac{1}{2}\rho\omega^2\alpha_m\alpha_m - \frac{1}{2}\rho k^2\alpha_m\alpha_n B_{mn} \tag{4.13}$$

where here there is a summation over m and n which ranges from 2 to 3. Writing this out in detail

$$L = \frac{1}{2}\rho\omega^2(\alpha_2^2 + \alpha_3^2) - \frac{1}{2}\rho k^2(\alpha_2^2 B_{22} + 2\alpha_2\alpha_3 B_{23} + \alpha_3^2 B_{33}) \tag{4.14}$$

In Supplementary Materials section S.5, we show that Hamilton's Principle implies $\partial L/\partial\alpha_2 = \partial L/\partial\alpha_3 = 0$, thus taking the derivatives and dividing by ρk^2, we find

$$0 = \frac{\partial L}{\partial\alpha_2} = V^2\alpha_2 - B_{22}\alpha_2 - B_{23}\alpha_3 \tag{4.15}$$

$$0 = \frac{\partial L}{\partial\alpha_3} = V^2\alpha_3 - B_{23}\alpha_2 - B_{33}\alpha_3 \tag{4.16}$$

which can be written in matrix form as the following eigenvalue problem

$$\begin{pmatrix} B_{22} & B_{23} \\ B_{23} & B_{33} \end{pmatrix} \begin{pmatrix} \alpha_1 \\ \alpha_2 \end{pmatrix} = V^2 \begin{pmatrix} \alpha_1 \\ \alpha_2 \end{pmatrix} \equiv V^2 \begin{pmatrix} a_{SH} \\ a_{SV} \end{pmatrix} \equiv V^2 \begin{pmatrix} \cos\Phi \\ \sin\Phi \end{pmatrix} \tag{4.17}$$

where the last two equalities follow by definition. Formally, this equation is for the $m = 2$ mode, but the same procedure can be applied to the $m = 3$ mode, which are the two solutions to this eigenvalue equation, one for $m = 2$ and one for $m = 3$. The two eigenvalues of equation (4.17), $V^2_{(2,3)}$, are the squared phase speeds of quasi-S_1 and quasi-S_2, respectively. The eigenvectors are the polarizations of these two waves: $\tilde{\mathbf{a}}^{(2)} = (\cos\Phi, \sin\Phi)^T$ and $\tilde{\mathbf{a}}^{(3)} = (-\sin\Phi, \cos\Phi)^T$.

4.3 Eigenvalues and eigenvectors

The solvability condition for equation (4.17) is

$$\det\begin{bmatrix} B_{22} - V^2_{(m)} & B_{23} \\ B_{23} & B_{33} - V^2_{(m)} \end{bmatrix} = 0 \tag{4.18}$$

Two solutions emerge, one for quasi-S_1 ($V^2_{(2)}$) and the other for quasi-S_2 ($V^2_{(3)}$):

$$V^2_{(2,3)} = \frac{1}{2}\left[B_{22} + B_{33} \pm B\right] \tag{4.19}$$

where

$$B \equiv \left[(B_{22} - B_{33})^2 + 4B_{23}^2\right]^{1/2} \tag{4.20}$$

We normally take the minus sign in equation (4.19) for quasi-S_1 ($m = 2$) and the plus sign for quasi-S_2 ($m = 3$), but this must be done after we remove the absolute value in B (as we do in equation (S32) in the Supplementary Materials). If we were to assign a single sign for one quasi-shear wave after applying the absolute value to B the results could be incorrect when the velocities of quasi-S_1 and quasi-S_2 are not well separated.

Note that if anisotropy is weak, V will vary with azimuth similarly to V^2. To see this, assume that $V \approx V_0 + \delta V$ where $\delta V / V_0 << 1$ and V_0 is the phase speed in an azimuthally invariant (e.g. isotropic or VTI) reference state. In this case, $V^2 \approx V_0^2 + 2V_0\delta V$ which implies that δV and therefore V will vary with azimuth similarly to V^2.

Supplementary Materials section S.3 shows that the polarization angle Φ is given by

$$\tan\Phi = \frac{B_{33} - B_{22} \pm B}{B_{23}} \tag{4.21}$$

where we use the minus sign for quasi-S_1 and

$$\tan 2\Phi = \frac{2B_{23}}{B_{22} - B_{33}} \tag{4.22}$$

Φ is typically non-zero ony if $B_{23} \neq 0$. Section 4.6 discusses a caveat to this for a HTI medium, in which $B_{23} = 0$ and $\Phi = 90°$. We refer to B_{23} as the $SV - SH$ coupling term.

If $B_{23} = 0$, then the polarization angle $\Phi = 0$ (except for a HTI medium) and the eigenvectors are the same as in the reference state.

Some researchers do not assign the two signs in B in equation (4.19) to particular quasi-S waves, but refer only to the faster and slower S-waves at each azimuth, forgoing the quasi-S_1 and quasi-S_2 terminology. Retaining this terminology, we assign the appropriate sign in B for quasi-S_1 and quasi-S_2.

If $B_{23} \neq 0$ there will be $SV - SH$ coupling, so that the eigenvalues of quasi-S_1 and quasi-S_2 share each other's azimuthal dependence with the additional azimuthal dependence provided by B. As discussed in section 4.1, in the absence of $SV - SH$ coupling, quasi-S_1 will vary azimuthally as 4ψ whereas the quasi-S_2 will vary as 2ψ. With $SV - SH$ coupling, both can vary as 2ψ and 4ψ.

With $SV - SH$ coupling, the eigenvectors $\tilde{\mathbf{a}}^{(2)}$ and $\tilde{\mathbf{a}}^{(3)}$ will be rotated through angle Φ. Depending on the relative values of B_{22} and B_{33}, $\tilde{\mathbf{a}}^{(2)}$ may be polarized more like the reference SH or like the reference SV wave. Numerical examples in Section 4.6 clarify this further.

4.4 General anisotropy

Supplementary Materials section S.1 presents derivations of B_{11}, B_{22}, B_{33}, and B_{23} for a general anisotropic medium:

$$B_{11}(\psi) = \rho^{-1}\left(\mathcal{A} + B_c\cos(2\psi) - B_s\sin(2\psi) + E_c\cos(4\psi) - E_s\sin(4\psi)\right) \tag{4.23}$$

$$B_{22}(\psi) = \rho^{-1}\left(\mathcal{N} - E_c\cos(4\psi) + E_s\sin(4\psi)\right) \tag{4.24}$$

$$B_{33}(\psi) = \rho^{-1}\left(\mathcal{L} + G_c\cos(2\psi) - G_s\sin(2\psi)\right) \tag{4.25}$$

$$B_{23}(\psi) = \rho^{-1}\left(-M_s\cos(\psi) - M_c\sin(\psi) + D_s\cos(3\psi) - D_c\sin(3\psi)\right) \tag{4.26}$$

where the coefficients ($\mathcal{A}, \mathcal{N}, \mathcal{L}$, etc) are defined in Appendix B. For quasi-P, we assume there is no coupling to the quasi-S waves and therefore its phase speed will be given by equation (4.5)

$$V_{(1)}^2 = V_{qP}^2 = B_{11} = \rho^{-1}\left(\mathcal{A} + B_c\cos(2\psi) - B_s\sin(2\psi) + E_c\cos(4\psi) - E_s\sin(4\psi)\right) \tag{4.27}$$

In the absence of SV-SH coupling, $B_{23} = 0$ and quasi-S$_1$ and quasi-S$_2$ have the following phase speeds

$$V_{(2)}^2 = V_{qS_1}^2 = B_{33} = \rho^{-1}\left(\mathcal{L} + G_c\cos(2\psi) - G_s\sin(2\psi)\right) \tag{4.28}$$

$$V_{(3)}^2 = V_{qS_2}^2 = B_{22} = \rho^{-1}\left(\mathcal{N} - E_c\cos(4\psi) + E_s\sin(4\psi)\right) \tag{4.29}$$

Equations (4.27) - (4.29), which emerge from the quasi-degenerate theory with $B_{23} = 0$, are the same as those from Rayleigh's Principle, equations (4.5) - (4.7). If one thinks of quasi-S$_1$ as quasi-SH and quasi-S$_2$ as quasi-SV, these equations have their polarizations switched relative to those from Rayleigh's Principle. This is not the case once the perturbed polarizations are considered, as will be discussed for a TTI medium in the following sections.

If $B_{23} \neq 0$, quasi-S$_2$ and quasi-S$_1$ will couple and both will share the azimuthal variation of B_{22} and B_{33}. Therefore, $V_{(2)}^2$ and $V_{(3)}^2$ both will display a mixture of 2ψ and 4ψ azimuthal variation. Although the coupling term B_{23} has an azimuthal dependence on 1ψ and 3ψ, it does not add odd-order azimuthal variation to the wave speed, which would not satisfy reciprocity. This is because the wave speed depends on $\sqrt{B_{23}^2} = |B_{23}|$. For example, although $\sin\psi$ has one maximum in $\psi \in [0, 2\pi]$ and $\sin 2\psi$ has two maxima separated by π on the same interval, $|\sin\psi|$ is quite similar to $(1 - \cos 2\psi)/2$ and has two maxima. Thus, a non-zero B_{23} term will satisfy reciprocity:

$$V(\psi) = V(\psi + \pi), \tag{4.30}$$

and will add both 2ψ and 4ψ azimuthal variability, not 1ψ and 3ψ. However, the 3ψ component does introduce a 6ψ contribution to V^2, but it is small enough to ignore.

4.5 TTI medium

As shown in Supplementary Materials section S.2, the eigenvalues and eigenvectors for the quasi-S waves in a general anisotropic medium simplify substantially when they are considered for a TTI medium. We define tilt through dip angle θ around the y-axis, which we refer to as the "strike axis".

For the quasi-S$_1$ and quasi-S$_2$ waves

$$\rho V_{qS_1}^2 = C_0 + C_2\cos 2\psi \tag{4.31}$$

$$\rho V_{qS_2}^2 = B_0 + B_2\cos 2\psi + B_4\cos 4\psi, \tag{4.32}$$

where

$$C_0 = \frac{1}{2}\left(L(1-\cos^2\theta)+N(1+\cos^2\theta)\right) \tag{4.33}$$
$$C_2 = \frac{1}{2}(L-N)\sin^2\theta \tag{4.34}$$
$$B_0 = L+E\left(\frac{1}{2}\sin^2\theta\cos^2\theta+\frac{1}{8}\sin^4\theta\right)\approx B_0^{HTI}\approx\frac{1}{8}(A+C-2F)(1+\eta_X) \tag{4.35}$$
$$B_2 = \frac{1}{2}E\sin^2\theta\cos^2\theta\approx\frac{1}{2}(A+C-2F)(1-\eta_X)\sin^2\theta\cos^2\theta \tag{4.36}$$
$$B_4 = -\frac{1}{8}E\sin^4\theta\approx-\frac{1}{8}(A+C-2F)(1-\eta_X)\sin^4\theta \tag{4.37}$$

and $E\equiv A+C-2F-4L$, as defined in the Supplementary Materials section S.2.

The relative peak-to-peak amplitude of the 2ψ component of quasi-S_1 is independent of E and approximately simplifes to:

$$\frac{|C_2|}{C_0} \approx \frac{|L-N|}{L+N}\sin^2\theta \tag{4.38}$$

The signs of B_2 and B_4 for quasi-S_2 and their relationship to the sign of C_2 for quasi-S_1, will be determined in part by the sign of E. This will specify the relative phase of the azimuthal variations of quasi-S_1 and quasi-S_2. The sign of E will depend on the relative size of $4L$ and $A+C-2F$. If $E=0$, $4L=A+C-2F$, then quasi-S_2 will show no azimuthal variation, its phase front will be spherical, and the quasi-P ($B_4=0$, $E_c=0$) and quasi-S_1 will both have elliptical phase fronts. This is so-called elliptical anisotropy.

As discussed further in Supplementary Materials S.4, this motivates the definition of a new ellipticity parameter

$$\eta_X=\frac{4L}{A+C-2F} \tag{4.39}$$

which for weak anisotropy is approximately equal to the parameter η_K introduced by Kawakatsu (2016), as illustrated by **Figure S2**. $\eta_X=1$ for elliptical anisotropy but is typically less than 1 for real Earth materials (Brownlee *et al*. 2017) as **Figure S2** shows, at least for crustal rocks.

As shown in Supplementary Materials S.4, the coefficients B_0, B_2 and B_4 for quasi-S_2 can be expressed approximately in terms of η_X according to the final expressions in equations (4.35) - (4.37). $A+C-2F$ is normally positive in Earth materials. The relative peak-to-peak amplitude of 2ψ and 4ψ anisotropy of quasi-S_2 can therefore be expressed as

$$\frac{|B_2|}{B_0} \approx 2|1-\eta_X|\sin^2\theta\cos^2\theta \tag{4.40}$$
$$\frac{|B_4|}{B_0} \approx \frac{1}{2}|1-\eta_X|\sin^4\theta \tag{4.41}$$

The polarization angle Φ for the coupled quasi-S waves is derived in Supplementary Materials S.3

as

$$\tan\Phi = \tan\theta\sin\psi \tag{4.42}$$

where $-\theta \leq \Phi \leq \theta$. $|\Phi|$ will be no larger than the dip angle θ, and will average about $\theta/2$.

4.6 Discussion of the TTI medium with numerical examples

Figure 7 shows phase speed versus azimuth for quasi-S_1 and quasi-S_2 from both degenerate and non-degenerate perturbation theory at three dip angles: $\theta = 20°, 45°$, and $70°$. Rock sample #20 from the elastic tensor compilation of Brownlee *et al*. (2017) is used for this figure as well as in **Figures 4** and **5a**. Anisotropy in this rock sample is non-elliptical ($\eta_X = 0.97$) so $E \neq 0$ and generally $B_{23} \neq 0$. Therefore, with this rock sample and most others in the compilation, there is SV-SH coupling.

The phase speed curves based on the quasi-degeneracy condition or degenerate perturbation theory for $\theta = 0°$ (VTI medium) and $\theta = 90°$ (HTI medium) are the same as those from non-degenerate theory or Rayleigh's Principle and are presented in **Figure 6**. Phase speed curves for $\theta \neq 0°$ and $\neq 90°$ from non-degenerate perturbation theory are inaccurate because they do not include the effect of SV-SH coupling. The phase speed curves shown in **Figure 6** for $\theta = 45°$ are inaccurate, therefore, as are the dashed lines in **Figure 7**, which are for non-degenerate perturbation theory.

At small dip angles where $\theta < 30°$ (e.g. **Figure 7a**), the quasi-S_1 phase speeds are similar to quasi-SH and quasi-S_2 speeds are similar to quasi-SV, where both are dominated by 2ψ azimuthal variations and $V_{qS_1} \approx V_{qSH}$ and $V_{qS_2} \approx V_{qSV}$. Both quasi-S_1 and quasi-S_2 possess more azimuthal variability under the quasi-degeneracy theory than under non-degenerate perturbation theory. Quasi-S_1 is always purely 2ψ but the 4ψ component of quasi-S_2 (B_4) is nearly zero when the dip angle is small (eqn (4.37)). In rock sample #20, there is slow axis symmetry, so $N - L > 0$ and $C_0 > B_0$ if we ignore E in equation (4.35) due to its small size. Therefore, $V_{qS_1} > V_{qS_2}$. About 80% of the rock samples in the compilation of Brownlee *et al*. (2017) have slow axis symmetry. Therefore, some crustal rocks have fast axis symmetry and there is evidence that the anisotropy of mantle rocks, when approximated with a transversely isotropic elastic tensor, may display fast axis symmetry on average (Becker *et al*. 2006). For a fast symmetry axis, $L - N > 0$ and $B_0 > C_0$, again ignoring E in equation (4.35). Therefore, $V_{qS_2} > V_{qS_1}$.

At intermediate dip angles such that $30° < \theta < 60°$ (e.g. **Figure 7b**), the azimuthal variations of quasi-S_1 and quasi-S_2 remain dominated by 2ψ and have much larger amplitudes than under non-degenerate perturbation theory. The difference in the azimuthal average of each shrinks and is closer to the average of quasi-SH and quasi-SV.

For steep dip angles where $\theta > 60°$ (e.g. **Figure 7c**), the quasi-S_1 phase speeds are now similar

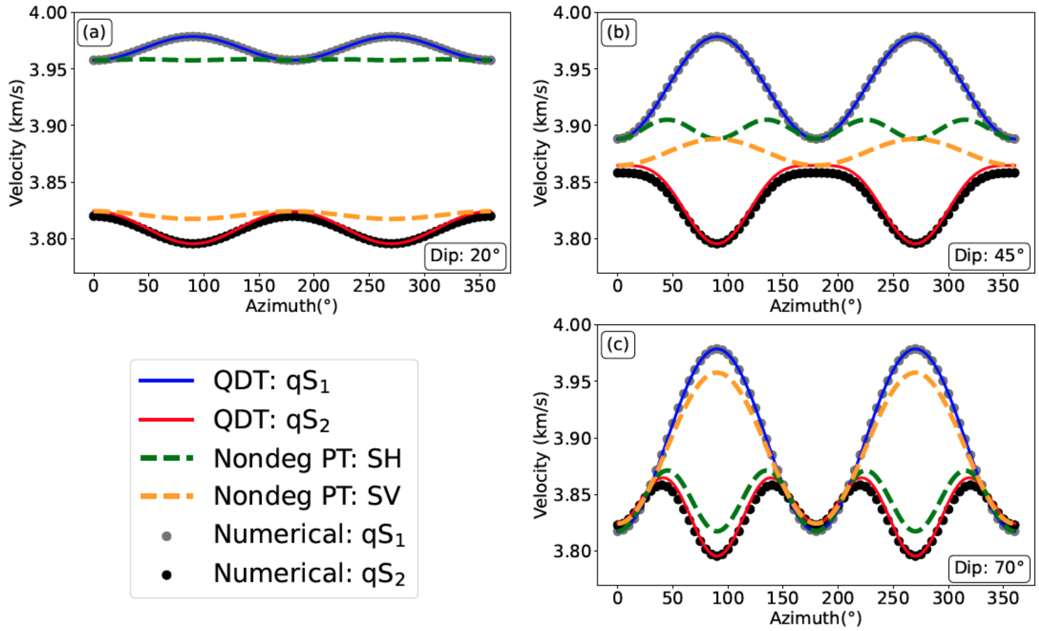

Figure 7. Comparison of azimuthal (ψ) variation of phase speed for non-degenerate perturbation theory (SH dashed green line, SV dashed yellow line) with quasi-S$_1$ and quasi-S$_2$ from quasi-degenerate theory (solid blue line, sold red line, respectively) and exact (i.e., numerical) solution (grey dots, black dots, respectively). The transversely isotropic component of sample #20 from Data Source 1 (Table 1) is used, tilted through dip angles of (a) $\theta = 20°$, (b) $\theta = 45°$, and (c) $\theta = 70°$. Dip angles of $0°$ and $90°$ are the same as from Rayleigh's Principle, **Fig. 6**.

to quasi-SV and quasi-S$_2$ speeds are similar to quasi-SH. Quasi-S$_1$ is dominated by 2ψ azimuthal variations with $V_{qS_1} \approx V_{qSV}$ from non-degenerate perturbation theory. Quasi-S$_2$ is dominated by 4ψ azimuthal variations with $V_{qS_2} \approx V_{qSH}$.

There are six curves shown in **Figure 7**. The two from the quasi-degenerate theory and the two from non-degenerate perturbation theory are approximate. The two that are computed numerically are exact (to numerical accuracy) based on the numerical solution of the Christoffel equation. Phase speed from the quasi-degenerate theory for quasi-S$_2$ deviates slightly from the exact phase speed due to unmodeled coupling to the quasi-P.

We see, therefore, that quasi-S$_1$ starts out for shallow dip angles as very similar to quasi-SH from non-degenerate perturbation theory, although with larger amplitudes of azimuthal variability. At intermediate dip angles, the character of quasi-S$_1$ changes and it becomes a strongly coupled mixture of quasi-SH and quasi-SV. At large dip angles, quasi-S$_1$ has become more similar to quasi-SV. This change in character is reflected in the polarization angles shown in **Figure 8**.

The amplitudes of the 2ψ variation for quasi-S$_1$ (C_2, eqn (4.34)) and 4ψ variation for quasi-S$_2$ (B_4, eqn (4.37)) grow monotonically with dip angle θ. The amplitudes of the 2ψ variation for quasi-

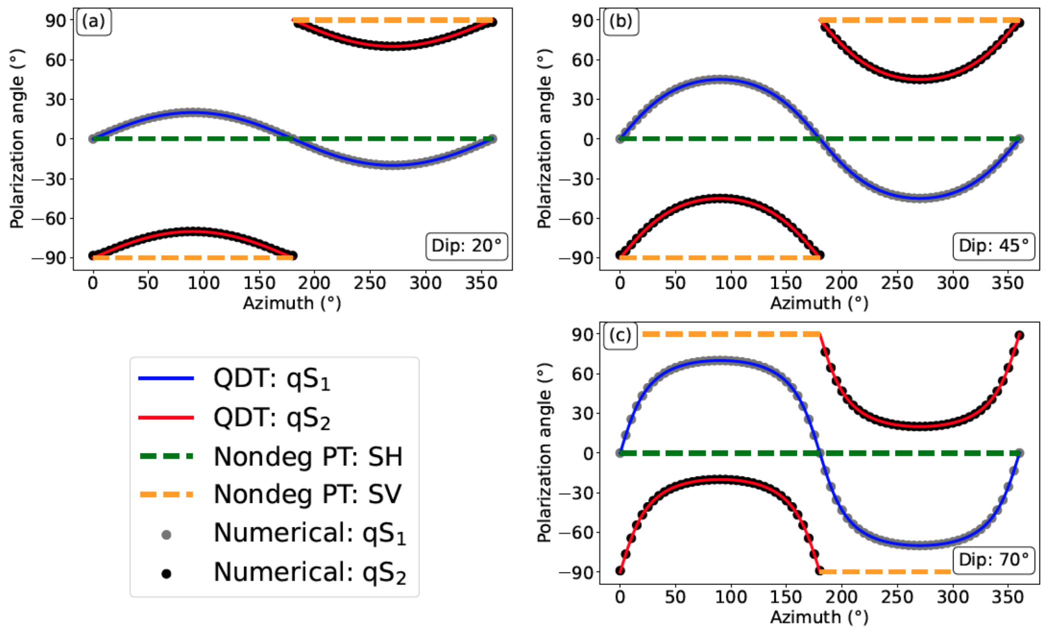

Figure 8. Same as **Figure 7**, except polarization angle Φ is presented. For quasi-S_1 and SH the polarization angle Φ is plotted and for quasi-S_2 and SV a range of 180° is plotted for clarity. See **Figure 3** for a definition of Φ.

S_2 (B_2, eqn (4.36) does not grow monotonically with dip angle, but maximizes at $\theta = 45°$. The dip angle can be inferred from the amplitude of the 2ψ and 4ψ variations for the quasi-S_2 wave as follows

$$\tan\theta = \sqrt{\frac{4|B_4|}{|B_2|}} \tag{4.43}$$

Once θ is estimated, the polarization angle of the coupled quasi-S waves (Φ) can be computed using equation (4.42). Also, $|1-\eta_X|$ can be estimated from either equation (4.40) or (4.41). **Figure 9** shows that when $\eta_X < 1$, the 2ψ (dashed purple line) and 4ψ (solid red line) components of qS_2 will be out of phase, whereas if $\eta_X > 1$ they will be in phase. This information allows the sign of $1 - \eta_X$ to be determined.

Different values of $L - N$ and η_X can result in the fast directions of quasi-S_1 and quasi-S_2 being either in phase, which we call “parallel”, or out of phase by 180°, which we call “perpendicular”.

Table 2. Alignment of 2ψ azimuthal anisotropy for quasi-S_1 and quasi-S_2.

	Slow axis ($L < N$)	Fast axis ($L > N$)
$\eta_X < 1$	perpendicular	parallel
$\eta_X > 1$	parallel	perpendicular

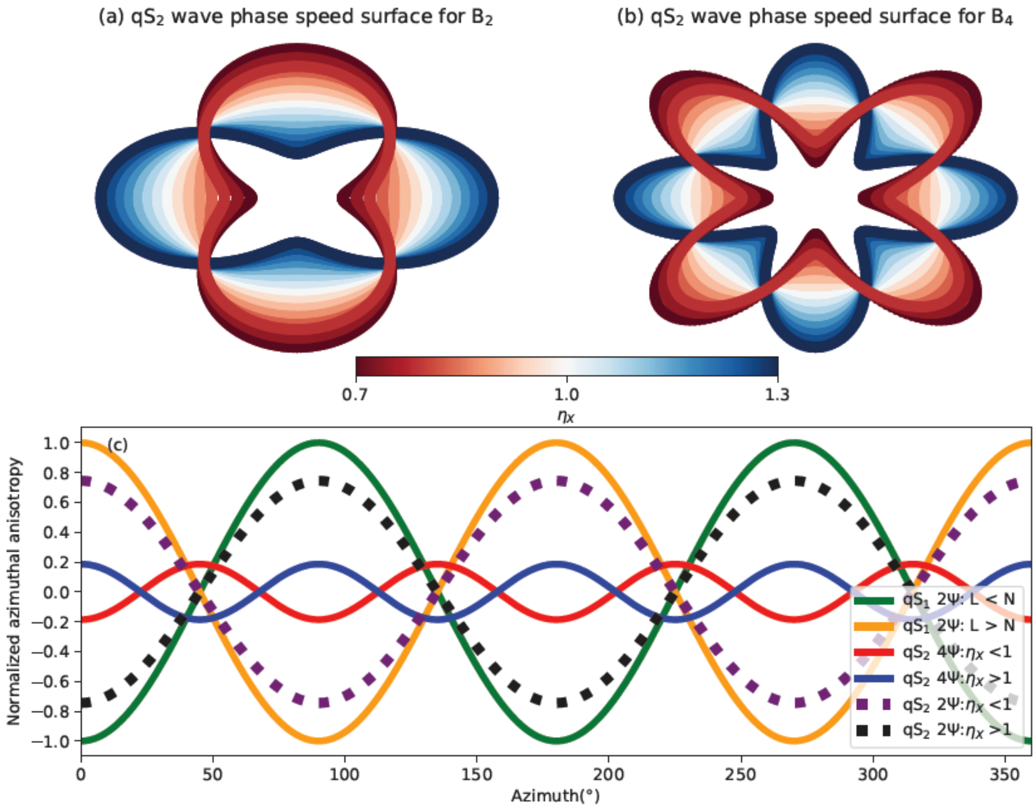

Figure 9. Azimuthal anisotropy with a dip angle $\theta = 45^\circ$ for quasi-S$_1$ and quasi-S$_2$: quasi-S$_1$ 2ψ (green solid line for slow axis and orange solid line for fast axis), quasi-S$_2$ 4ψ (red solid line for $\eta_X < 1$ and blue solid line for $\eta_X > 1$), and quasi-S$_2$ 2ψ (purple dashed line for for $\eta_X < 1$ and black dashed line for $\eta_X > 1$). The results are normalized by isotropic phase speed and $|B_2| = 4|B_4|$ by equation.(4.43).

Table 2 summarizes the circumstances in which a parallel or perpendicular relationship between the fast axes will occur, in which only the 2ψ anisotropy is considered.

Figure 9a,b illustrates how changing the value of the ellipticity parameter η_X changes the azimuth of the fast directions. For the 2ψ component of the quasi-S$_2$ wave, the orientation of the fast directions rotate 90° when $1 - \eta_X$ changes sign. For the 4ψ component, the rotation is 45°. **Figure 9c** includes how the variation of quasi-S$_1$ and quasi-S$_2$ with azimuth depends on the relationship with $L - N$ and η_X.

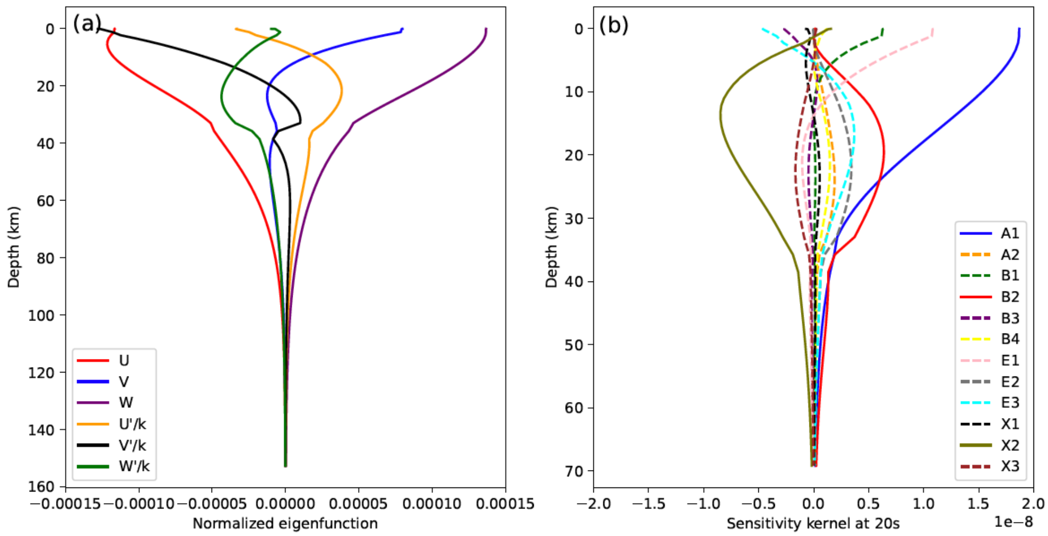

Figure 10. (a) Eigenfunctions for Rayleigh and Love wave fundamental modes at 20 s period computed using the effective transversely isotropic component of the 1D model in western Alaska at (64°N, 159°W) (Data source 2). (b) Sensitivity kernels composing the integrals in equations (5.3) - (5.6): $A1 = W^2$, $A2 = W'^2/k^2$ $B1 = V^2$, $B2 = (U - V'/k)^2$, $B3 = VU'/k$, $B4 = U'^2/k^2$, $E1 = WV$, $E2 = (U - V'/k)W'/k$, $E3 = WU'/k$, $X1 = VW'/k$, $X2 = W(U - V'/k)$, $X3 = U'W'/k^2$.

5 THE EFFECT OF RAYLEIGH-LOVE COUPLING

5.1 Theory

Most of the foundational equations are presented in section 3. In Cartesian coordinates $(x_1, x_2, x_3) = (x, y, z)$, for a laterally homogeneous isotropic or transversely isotropic medium, the displacements for Rayleigh and Love waves propagating at azimuth ψ are given by equations (3.12) and (3.13) where f is given by equation (3.9). Displacement $\vec{\mathbf{u}}$ in an anisotropic medium is given by equation (3.23). The displacement field in an anisotropic medium for a coupled Rayleigh and Love wave propagating at azimuth ψ is given by equation (3.24). For a linear elastic body, the Lagrangian density is given by equation (3.26).

Example phase speed curves for Rayleigh and Love modes are presented in **Figure 5a**. Example eigenfunctions are shown in **Figure 10a**.

Expressions for T and V are derived in Supplementary Materials S.6, and are

$$T = \frac{1}{2}\omega^2 \left(a_L a_L^* + a_R a_R^*\right) \tag{5.1}$$

$$V = \frac{1}{2}[a_L a_L^* A + a_R a_R^* B + (a_L a_R^* + a_L^* a_R)E + i(a_L a_R^* - a_L^* a_R)X] \tag{5.2}$$

In the expression for the potential energy, if a_L and a_R were real, the term in parenthesis before

X would be 0. X only contributes to Rayleigh-Love coupling if $a_R, a_L \in \mathbb{C}$. A, B, E, and X are

$$A = k^2 \int_0^\infty dz[(\mathcal{N} - E_c \cos 4\psi + E_s \sin 4\psi)W^2 + (\mathcal{L} - G_c \cos 2\psi + G_s \sin 2\psi)W'^2/k^2] \tag{5.3}$$

$$\begin{aligned} B =& k^2 \int_0^\infty dz[(\mathcal{A} + B_c \cos 2\psi - B_s \sin 2\psi + E_c \cos 4\psi - E_s \sin 4\psi)V^2 \\ &+ (\mathcal{L} + G_c \cos 2\psi - G_s \sin 2\psi)(U - \frac{V'}{k})^2 \\ &+ 2(\mathcal{F} + H_c \cos 2\psi - H_s \sin 2\psi)VU'/k + \mathcal{C}U'^2/k^2] \end{aligned} \tag{5.4}$$

$$\begin{aligned} E =& k^2 \int_0^\infty dz[(-\frac{1}{2}B_c \sin 2\psi - \frac{1}{2}B_s \cos 2\psi - E_c \sin 4\psi - E_s \cos 4\psi)WV \\ &+ (G_c \sin 2\psi + G_s \cos 2\psi)(U - \frac{V'}{k})W'/k + (-H_c \sin 2\psi - H_s \cos 2\psi)WU'/k] \end{aligned} \tag{5.5}$$

$$\begin{aligned} X =& k^2 \int_0^\infty dz\{[2(J_c - M_c)\sin\psi - 2(J_s + M_s)\cos\psi + D_c \sin 3\psi - D_s \cos 3\psi]VW'/k \\ &+ (M_c \sin\psi + M_s \cos\psi + D_c \sin 3\psi - D_s \cos 3\psi)W(U - \frac{V'}{k}) \\ &+ 2[(J_c - K_c)\sin\psi - (J_s - K_s)\cos\psi]W'U'/k^2\} \end{aligned} \tag{5.6}$$

We refer to the products of eigenfunctions in A, B, E, and X as "sensitivity kernels". **Figure 10b** shows examples of the 12 sensitivity kernels at 20 s period. The kernels W^2 in A, $(U - V'/k)^2$ in B, and $W(U - V'/k)$ in X dominate.

Hamilton's Principle implies that $\partial L/\partial a_R = \partial L/\partial a_L = 0$ (Supplementary Materials S.5.2), which is used in Supplementary Materials S.6 to derive the following eigenvalue problem that governs Rayleigh-Love coupling:

$$\begin{pmatrix} A & E + iX \\ E - iX & B \end{pmatrix} \begin{pmatrix} a_L^* \\ a_R^* \end{pmatrix} = \omega^2 \begin{pmatrix} a_L^* \\ a_R^* \end{pmatrix} \tag{5.7}$$

which is analogous to equation (4.17) for body waves.

The solvability condition yields the coupled quasi-Love ($m = 1$) and quasi-Rayleigh wave ($m = 2$) eigenfrequencies given by

$$\omega^2 = \frac{A + B \pm \sqrt{(A-B)^2 + 4(E^2 + X^2)}}{2} \equiv \frac{1}{2}[A + B \pm D] \tag{5.8}$$

or phase speed given by

$$V^2{}_{qL} = \frac{1}{2k^2}[A + B + D] \tag{5.9}$$

$$V^2{}_{qR} = \frac{1}{2k^2}[A + B - D] \tag{5.10}$$

where

$$D \equiv ((A - B)^2 + 4(E^2 + X^2))^{1/2}. \tag{5.11}$$

Because Love waves are consistently faster than Rayleigh waves, we assign the higher frequency or higher phase speed to the quasi-Love wave and the slower one to the quasi-Rayleigh wave.

Equation (5.8) is analogous to equation (4.19) for body waves. The first term A is analogous to SH waves (B_{22}) and the second term B is analogous to SV waves (B_{33}). The term $4(E^2 + X^2)$ is the Rayleigh-Love coupling term, analogous to $4B_{23}^2$, describing the coupling between SV waves and SH waves. E is typically quite small for fundamental mode Rayleigh-Love coupling, as Tanimoto (2004) discusses. When the medium is VTI or HTI, X is zero, which yields only weak coupling, as studied by Tanimoto (2004).

As with body waves, the $(E^2 + X^2)$ term (analogous to B_{23}^2) satisfies reciprocity and mostly contributes to the 2ψ and 4ψ variations in V^2. A small additional contribution to a 6ψ variation is ignorable.

5.2 Phase speeds and fast orientations

Figure 11 presents examples of phase speeds as a function of azimuth for the 45 s Rayleigh and and 40 s Love waves computed using models at two points in Alaska with different relationships between the fast orientations for Rayleigh and Love waves. The dashed lines are Rayleigh and Love wave curves (**Fig. 11**a,b,d,e) computed using the non-degenerate perturbation theory (NDPT) of Smith & Dahlen (1973). Based on NDPT, the Love wave is dominated by 4ψ azimuthal variations and the Rayleigh wave variations are dominantly 2ψ. The solid lines are quasi-Rayleigh and quasi-Love wave curves computed using the quasi-degenerate theory (QDT) presented here. The quasi-Rayleigh and quasi-Love wave azimuthal variations contain prominent contributions from both 2ψ and 4ψ. In western Alaska, the fast axis directions of quasi-Rayleigh and quasi-Love are out of phase by 180° and in eastern Alaska they are in phase.

The phasing between the fast directions of quasi-Rayleigh and quasi-Love waves reflects the relationship between the observed quasi-Rayleigh wave fast orientations and the strike of anisotropy, which at short periods is often observed to be aligned with faults (e.g. Xie *et al*. 2017; C. Liu & Ritzwoller 2024). The fast orientation of the 2ψ component of the Love wave azimuthal variation is usually oriented in the direction of the strike of anisotropy (see **Fig. 3** for definition). In western Alaska, the fast axis direction of the quasi-Rayleigh wave is perpendicular to the fast axis direction of the quasi-Love wave and therefore the strike of anisotropy, whereas in eastern Alaska it will be aligned with the strike direction. The sign of the G_c parameter (namely the relative size of C_{55} and C_{44}) determines the relationship between Rayleigh wave 2ψ and Love wave 2ψ fast axes. The above and later discussion of the strike angle assume Rayleigh-Love coupling does not change the sign of the 2ψ component of the Rayleigh wave, which is usually true for fundamental mode surface waves in Alaska (**Fig. 11**). We discuss later why the quasi-Love wave 2ψ fast axis typically aligns with the strike direction. It is noteworthy that for body waves (also coupling between overtones) the strike analysis is not valid because of near degeneracy and very strong mode coupling.

5.3 Amplitudes

Figure 11c,f illustrates how the phasing between the fast axis orientations of quasi-Love and quasi-Rayleigh waves affects the amplitude of their azimuthal variations. The right column of **Figure 11** for a point in eastern Alaska presents an example when the quasi-Rayleigh wave fast orientation aligns with the Love wave fast orientation. In this case, the Rayleigh-Love coupling transfers amplitude from the Rayleigh wave to the Love wave. By this we mean the amplitude of the quasi-Rayleigh wave under QDT is reduced relative to the Rayleigh wave under NDPT, whereas the quasi-Love wave amplitude is increased relative to NDPT. In contrast, when the quasi-Rayleigh and quasi-Love 2ψ fast orientations are out of phase by 180°, as they are in western Alaska, the amplitudes of both the quasi-Rayleigh and quasi-Love under QDT increase relative to NDPT. This transfer of 2ψ amplitude can be complicated for surface waves due to the lack of a similarly compact solution as for body waves, but the body waves provide guidance, as discussed in section 6.4.

These observations provide information about the effect of applying NDPT to data that should be modeled with QDT. For example, in western Alaska (**Fig. 11**c), it would be very hard to fit the amplitude of azimuthal variations at long periods. The tendency would be to overestimate the amplitude of anisotropy in the mantle.

5.4 Coupling strength

The strength of coupling depends on the relative size of $4(E^2 + X^2)$ and $(A - B)^2$ in D in equation (5.11). We define the coupling strength as follows

$$S = \frac{4(E^2 + X^2)}{(A - B)^2} \tag{5.12}$$

If $S << 1$, the Rayleigh-Love coupling term will be very small. **Figure 12**a presents an example of the relative size of the components of D at 40 s period. There is a broad range of azimuths where $X^2 >> E^2$ and where $4X^2$ is on the order of $(A - B)^2$. Rayleigh-Love coupling will be strong at those azimuths, which center on the Love wave 2ψ fast direction. The assumption here is that the Love wave is the faster surface wave, which is also assumed in the expression for polarization for quasi-

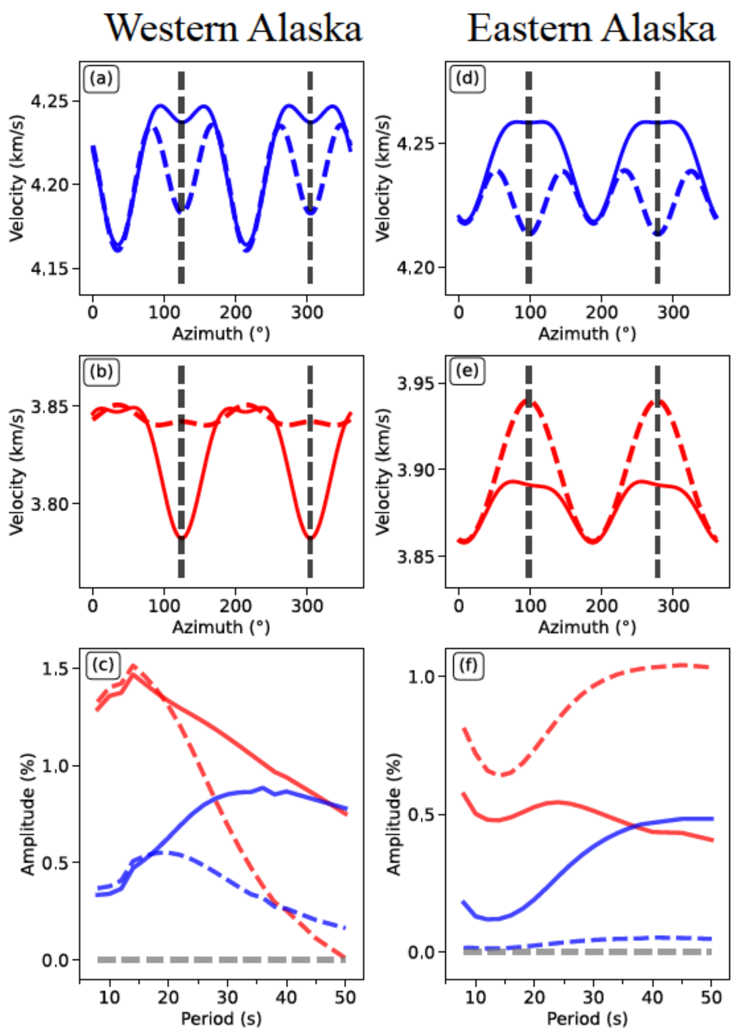

Figure 11. (Top Two Rows) Phase speed presented as a function of azimuth ψ for (blue lines) the 45 s Rayleigh wave and (red lines) the 40 s Love wave using two different theories: (solid lines) the quasi-degenerate theory (QDT) presented here and (dashed lines) the non-degenerate perturbation theory (NDPT) of Smith & Dahlen (1973). The model of anisotropy is Model 3 (discussed in section 6.1) using data from (left column) a point in western Alaska (64°N,159°W) and (right column) a point in eastern Alaska (64°N,147°W). The quasi-Love wave 2ψ fast axis orientations are shown with vertical dashed grey lines. (Bottom Row) The amplitude of the 2ψ component of anisotropy plotted as a function of period for (red lines) the 45 s Rayleigh wave and (blue lines) the 40 s Love wave. Solid lines are for QDT and dashed lines are for NDPT.

Love waves. If the Love wave were the slower one, strong Rayleigh-Love coupling would center on the Love wave 2ψ slow axis. As discussed further in section 6, at shorter periods X^2 typically reduces in size compared to $(A-B)^2$, so coupling weakens.

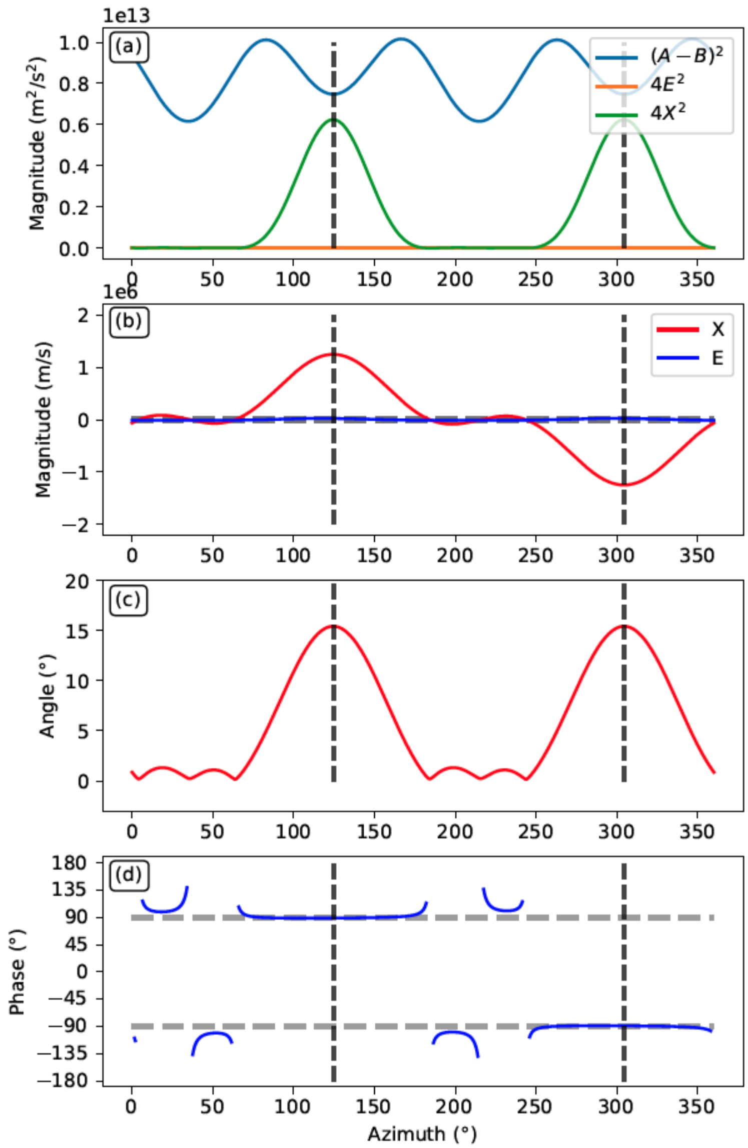

Figure 12. Effects of Rayleigh-Love coupling for a 45 s Rayleigh wave and a 40 s Love wave, computed with Model 3 (discussed in section 6.1) in western Alaska (64°N, 159°W). (a) Comparison of $(A-B)^2$ with $4E^2$ and $4X^2$, plotted as a function of azimuth. (b) X changes sign with azimuth. (c) Tilt angle Φ of the particle motion of the quasi-Love wave out of the horizontal plane. (d) Phase angle ϕ between the vertical and horizontal components of the quasi-Love (and quasi-Rayleigh) wave. Vertical dashed lines are the Love wave 2ψ fast axis directions, which illustrate that coupling effects maximizes in these directions.

5.5 Polarization and phase lag

In Supplementary Materials section S.6 we show that for the quasi-Love and quasi-Rayleigh waves, the non-normalized eigenvectors are

$$(a_L, a_R)_{qL} = (1, \Gamma e^{i\phi})^T \tag{5.13}$$

$$(a_L, a_R)_{qR} = (-\Gamma e^{-i\phi}, 1)^T \tag{5.14}$$

where $\Gamma \equiv (B - A + D)/2(E^2 + X^2)^{1/2}$. The vector eigenfunctions are therefore

$$\hat{\mathbf{s}}_{qL}(z) = (-\beta W(z) + \alpha\Gamma e^{i\phi} V(z), \alpha W(z) + \beta\Gamma e^{i\phi} V(z), \Gamma e^{i(\phi+\pi/2)} U(z))^T \tag{5.15}$$

$$\hat{\mathbf{s}}_{qR}(z) = (\alpha V(z) + \Gamma e^{-i\phi} \beta W(z), \beta V(z) - \alpha\Gamma e^{-i\phi} W(z), iU(z))^T \tag{5.16}$$

The polarization vector at the surface ($z = 0$) for the quasi-Love wave is rotated out of the horizontal plane by angle Φ, where

$$\tan\Phi = \Gamma \frac{U(0)}{W(0)} \tag{5.17}$$

or

$$\tan 2\Phi = \frac{2(E^2 + X^2)^{1/2}}{A - B} \frac{W(0)}{U(0)} \tag{5.18}$$

The quasi-Rayleigh wave is rotated from the vertical by nearly the same angle. **Figure 12**c presents an example of Φ at 40 s period, which maximizes near the Love wave 2ψ fast direction where coupling is strongest. In this example, the quasi-Love wave polarization will be tipped by a maximum angle $\Phi_{max} \sim 16°$ relative to the horizontal. At much shorter periods, the polarization angle away from horizontal will be smaller and would be difficult to observe. For Alaska, this example is typical.

The phase lag angle ϕ between the vertical and horizontal components is plotted for the same example in **Figure 12**d. At most azimuths, the lag is about $\pm 90°$. The lag angle changes sign from $90°$ to $-90°$ when X becomes negative, as shown in **Figure 12**b. The polarization anomalies of wave propagating in opposite directions will be opposite, therefore by observing polarization the anisotropy we are able to constrain the absolute dip direction of a medium and not just the relative dip angle. This is also revealed in the body wave numerical results (**Figure 8**). For $\phi = 90°$, the vector eigenfunction for the quasi-Love wave is

$$\hat{\mathbf{s}}_{qL}(z) \approx (-\beta W(z) + i\alpha\Gamma V(z), \alpha W(z) + i\beta\Gamma V(z), -\Gamma U(z))^T \tag{5.19}$$

Signs will be reversed if $\phi = -90°$.

To consider the particle motion it is useful to think of propagation in the x_1 direction ($\alpha = 1, \beta = 0$) such that $(x_1, x_2, x_3)^T$ are the radial, transverse, and vertical directions. In this case, the components of the vector eigenfunction become $(i\Gamma V, W, -\Gamma U)^T$. In this case, the transverse and vertical components of the vector eigenfunction are both real and in phase. Therefore, the particle motion for

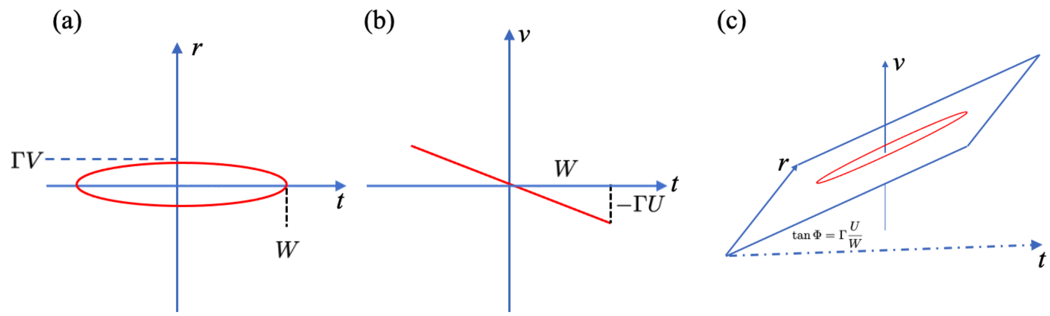

Figure 13. Visualization of particle motion when the phase angle between the vertical and horizontal components of the quasi-Love wave $\phi \sim 90°$, where the radial, transverse, and vertical directions are denoted r, t, and v and wave propagation is in the r direction. (a) Horizontal slice showing that the particle motion in the radial and transverse plane is elliptical.The radial component is typically much smaller than the transverse component because $\Gamma < 1$. (b) Vertical slice showing that the particle motion in the vertical and transverse plane is approximately linear. (c) Attempt at a 3D view, in which the plane of elliptical particle motion for the quasi-Love wave is tilted at an angle Φ relative to the transverse direction.

the vertical and transverse components will be linear and tilted by the angle Φ, which depends on Γ. However, the transverse and radial components will be out of phase by 90°, so the particle motion projected onto the horizontal plane will be an ellipse. **Figure 13** presents a visualization of this. The nearly linear particle motion in the transverse direction in the vertical plane can distinguish the quasi-Love wave from a diffracted Rayleigh wave, which will have an elliptical particle motion.

6 DISCUSSION OF RAYLEIGH-LOVE COUPLING

6.1 Inferring anisotropy in the presence of Rayleigh-Love coupling

For two principal reasons, most previous inversions of observations of surface wave azimuthal anisotropy have been based exclusively on the 2ψ component of the azimuthal variation of Rayleigh waves. First, early theoretical papers on Rayleigh and Love wave azimuthal anisotropy were based on non-degenerate perturbation theory (Smith & Dahlen 1973; Montagner & Nataf 1986), which predicted only 2ψ anisotropy for Rayleigh waves and 4ψ anisotropy for Love waves. Second, for practical reasons, Love wave anisotropy and the 4ψ anisotropy for Rayleigh waves have been more difficult to observe reliably. These two factors have combined to focus efforts on inferring anisotropy from isotropic phase speeds along with the 2ψ component of azimuthal variations in Rayleigh wave anisotropy (e.g. C. Liu *et al*. 2022).

As we show in section 5 theoretically, and has been increasingly observed in recent years (e.g. Russell *et al*. 2019; X. Liu *et al*. 2024), the 2ψ component of Love wave anisotropy may be quite large and the 4ψ component of Rayleigh wave anisotropy, although smaller, may also be observed. **Figure 1** presents an example for a point in western Alaska. These signals derive from Rayleigh-Love coupling which is modeled here through a quasi-degenerate theory. 4ψ Love wave anisotropy is also expected and observable (e.g. **Figure 1**), although it is rarely observed in practice.

Table 3. Models constructed using different observations and theoretical assumptions at point (64°N, 159°W) in western Alaska.

Model Number	Data Used	Theory Used
Model 1	Rayleigh 2ψ	NDPT
Model 2	Rayleigh 2ψ; Love 4ψ	NDPT
Model 3	Rayleigh 2ψ, 4ψ; Love 2ψ, 4ψ	QDT

Using observations at a location in western Alaska (64°N, 159°W), Data Source 4 in section 2, we present three inversion results to demonstrate the effect of using new (“unexpected”) signals (Love 2ψ, Rayleigh 4ψ) interpreted with and without Rayleigh-Love coupling. The three models are summarized in **Table 3**, where the theories used are the non-degenerate perturbation theory (NDPT) of Smith & Dahlen (1973) and Montagner & Nataf (1986) in which Rayleigh-Love coupling is absent and the quasi-degenerate theory (QDT) presented here, which models Rayleigh-Love coupling. Each inversion uses a different subset of the data but is performed with the same Bayesian Monte Carlo method, which is similar to that described by Xie *et al*. (2015, 2017) and C. Liu & Ritzwoller (2024). In this method, a posterior distribution of model variables is estimated, which we summarize with the

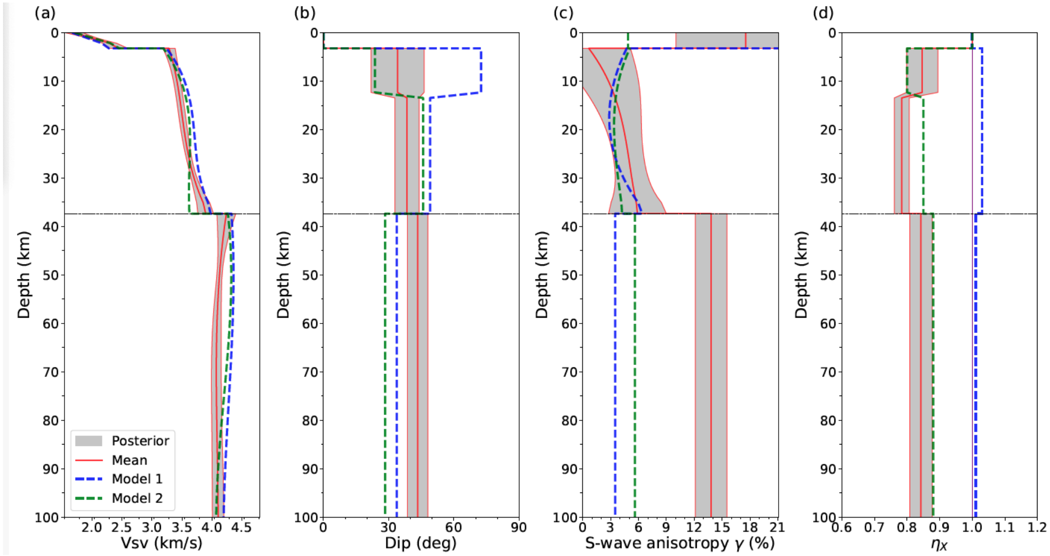

Figure 14. Four model variables presented for Models 1 - 3 at the location (64°N, 159°W) in western Alaska. $V_{SV} = \sqrt{L/\rho}$, dip angle θ for the TTI medium, S-wave anisotropy ($\gamma = (N - L)/2L$), and the ellipticity parameter η_X. Data and theory used in each inversion are listed in **Table 3**. The mean of the posterior distribution for Models 1 and Model 2 are shown with the blue and green dashed lines, respectively. The mean of the posterior distribution for Model 3 is shown with a solid red line, and the grey shading indicates the $\pm1\sigma$ corridor of the posterior distribution for Model 3.

mean and standard deviation of each model variable at each depth . The crust and mantle are both modeled as depth-dependent TTI media, where the dip angle θ can vary discontinuously with depth.

The set of observations at this location are presented in **Figure 14** also **Figure 2**), except for the Rayleigh and Love wave isotropic phase speed curves which we do not show. Model 1 is constructed using only the 2ψ component of Rayleigh wave azimuthal anisotropy using NDPT. This is similar to the data and theory used in current observational studies to infer the TTI elastic tensor as a function of depth (e.g. Xie *et al*. 2015, 2017; C. Liu & Ritzwoller 2024). Model 2 is constructed by augmenting the observations used in Model 1 with the 4ψ component of Love wave anisotropy, where the theory is still NDPT. Model 3 further augments these observations with Love wave 2ψ anisotropy and Rayleigh wave 4ψ anisotropy, and the theory used in the inversion is QDT presented here. The isotropic Rayleigh and Love wave phase speed curves are also used in the construction of all three models. The crust and mantle are both modeled as depth-dependent TTI media, where the dip angle θ of the upper crust, lower crust, and mantle are allowed to differ. Using the same data types and the quasi-degenerate theory, we also estimates a model in eastern Alaska at (64°, 147°W), which we also refer to as Model 3 but with the identifier "eastern Alaska". Examples of phase speed curves for Model

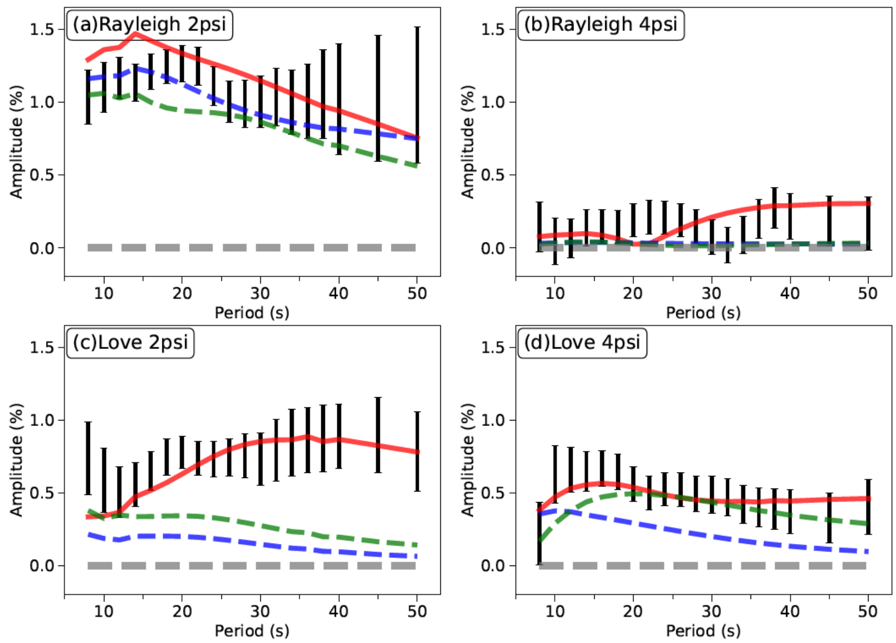

Figure 15. Comparison of observations (Data Source 4) of the amplitude of 2ψ and 4ψ components of Rayleigh and Love wave anisotropy (black 1σ error bars) from 8 s to 50 s period at location (64°N, 159°W) in western Alaska with predictions using the elastic tensor models Model 1 - Model 3 constructed here (**Table 3**). The blue dashed line is computed using Model 1 (based on Rayleigh wave 2ψ observations) and non-degenerate perturbation theory (Smith & Dahlen 1973; Montagner & Nataf 1986). The green dashed line is computed using Model 2 (based on Rayleigh wave 2ψ and Love wave 4ψ observations) and non-degenerate perturbation theory. The red line is computed using Model 3 (based on all observations) and using the quasi-degenerate theory we present here that includes Rayleigh-Love coupling. Using all data and the quasi-degenerate theory allows all data to be fit acceptably.

3 in western and eastern Alaska are presented in **Figure 11** using both non-degenerate perturbation theory and quasi-degenerate theory.

Figure 15 presents results from the inversions, showing four variables from the three models. These are the Love modulus L as $V_{SV} = \sqrt{L/\rho}$, the dip angle θ of the transversely isotropic elastic tensor, S-wave anisotropy $(N - L)/2L$, and the ellipticity parameter η_X (equation (4.39)) which is approximately equal to the "new" ellipticity parameter η_K of Kawakatsu (2016). All three models are represented as a posterior distribution with depth, but only the mean of the posterior distribution is shown for Models 1 and 2 whereas $\pm 1\sigma$ of the posterior distribution is shown for Model 3.

The introduction of observations of the 4ψ variation of Love wave phase speeds in Model 2 decreases the dip angle in the upper crust and, more significantly, reduces the ellipticity parameter in both the crust and mantle, compared to Model 1. This is illuminated by the body wave theory for a TTI medium, presented in section 4. Equation (4.37) shows that a large 4ψ component for quasi-S_2

will only occur if the ellipticity coefficient differs strongly from 1. Thus, to fit the Love wave 4ψ observations requires η_X to deviate from 1, which it does not in Model 1. Thus, the use of observations of the 4ψ component of Love wave anisotropy is particularly important to estimate the ellipticity of anisotropy accurately.

Figure 14 shows that all three models fit the Rayleigh 2ψ signal. In particular, the Rayleigh 2ψ signal can be fit with NDPT. Model 2 does fit the Love wave 4ψ signal, which shows that this signal can also be fit with NDPT. However, it typically will not be fit unless it is used in the inversion. Neither Model 1 nor Model 2 fits the Love wave 2ψ signal because quasi-degenerate theory is needed to produce large 2ψ amplitudes. Thus, applying all of the data and using the quasi-degenerate theory, which includes Rayleigh-Love coupling, allows all the data to be fit. Moreover, models produced with NDPT, such as the one presented by C. Liu & Ritzwoller (2024), will typically not produce strong enough Rayleigh-Love coupling to produce substantial 2ψ anisotropy for Love waves. Therefore, it is important to use quasi-degenerate theory in fitting anisotropy data to produce Rayleigh-Love coupling strong enough to produce the observed Love 2ψ signal.

Model 3 differs from Model 2 principally in the strength of anisotropy (γ), especially in the mantle. This results from the large amplitude of the Love wave 2ψ azimuthal variation. Since there is also a small observable Rayleigh wave 4ψ signal, these two models also differ somewhat in η_X. Although olivine samples in the laboratory may have S-wave anisotropy larger than 10% (e.g. Ismail & Mainprice 1998), anisotropy greater than 10% at the scale of seismic waves is probably not physically plausible due to spatial averaging. This calls into question the use of a TTI model to represent the elastic tensor in the mantle and highlights the need to revise the model to include a tilted orthorhombic elastic tensor in the mantle. Preliminary tests of inversions with a tilted orthorhombic elastic tensor in the mantle show that the strength of anisotropy reduces to between 4-6%, which is physically more plausible. When inverting Rayleigh and Love wave azimuthal anisotropy simultaneously in the presence of Rayleigh-Love coupling, it is important to model the mantle as a tilted orthorhombic medium although the crust can remain as a TTI medium.

6.2 Coupling between fundamental modes and overtones

Following the publication of Tanimoto (2004), Maupin (2004) commented that in oceanic settings the coupling of the Love wave fundamental mode to the Rayleigh wave 1st-overtone may be stronger than its coupling to the fundamental Rayleigh mode. We reconsider this comment for both continental and oceanic settings in light of the quasi-degenerate theory presented here, which produces stronger Rayleigh-Love coupling than the formalism of Tanimoto (2004).

In the foregoing, we have restricted ourselves to coupling between fundamental mode Love with

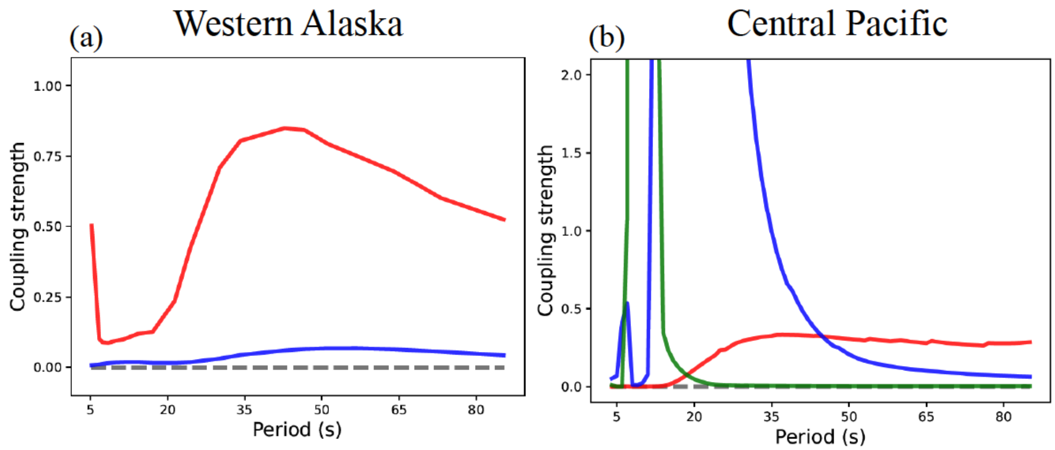

Figure 16. Coupling strength S (eqn (5.12)) plotted versus period for coupling between the fundamental mode Love wave and the fundamental (red lines) and overtone (1st overtone blue lines, 2nd overtone green line) Rayleigh wave. (a) Computed in a continental setting (western Alaska, 64°N, 159°W) using anisotropy Model 3, aspects of which are shown in **Figure 15**. (b) Computed in an oceanic setting southeast of Hawaii, using a revision of the anisotropy model from Data Source 3, aspects of which are shown in **Figure 17**.

fundamental mode Rayleigh waves. The quasi-degenerate theory we present can be also applied to any Rayleigh and Love modes, for example coupling between the fundamental mode Love wave and the 1st-overtone Rayleigh wave, coupling between the 1st overtone Love wave and 1st-overtone Rayleigh wave, and so on. We define coupling strength as S (equation (5.12)), which is plotted in **Figure 16**a for a continental location for coupling between the fundamental Love and fundamental Rayleigh modes (red line) and the fundamental Love and 1st-overtone Rayleigh modes (blue line). The fundamental mode coupling is much stronger than the overtone coupling in this continental location as it will be for most continental locations. This is because the Love wave and overtone phase speed curves are well separated as **Figure 5a** shows. The peak at short period ($\sim$5 s) is caused by the near degeneracy of the fundamental mode Rayleigh and Love curves at shorter periods. The coupling between the overtone Love and overtone Rayleigh modes is much stronger than the coupling between the fundamental Love and Rayleigh modes (not shown in **Figure 16**), because their phase speeds are almost degenerate. Analysis of overtones in continental areas should account for such strong coupling.

The relationship between the phase speed curves in oceans is quite different, as **Figure 5b** shows. To assess the effect on coupling strength we use the model of the elastic tensor in the crust and upper mantle southeast of Hawaii from Russell *et al.* (2019), although we revise it to increase the strength of anisotropy. We revise it by taking its effective transverse isotropic part, which is a VTI model and is included in their supplementary material, and increase N and A, by making (N-L)/2L = (A-C)/2C=7% across all depths. We then tilt the elastic tensor by 45°, which produces maximal coupling.

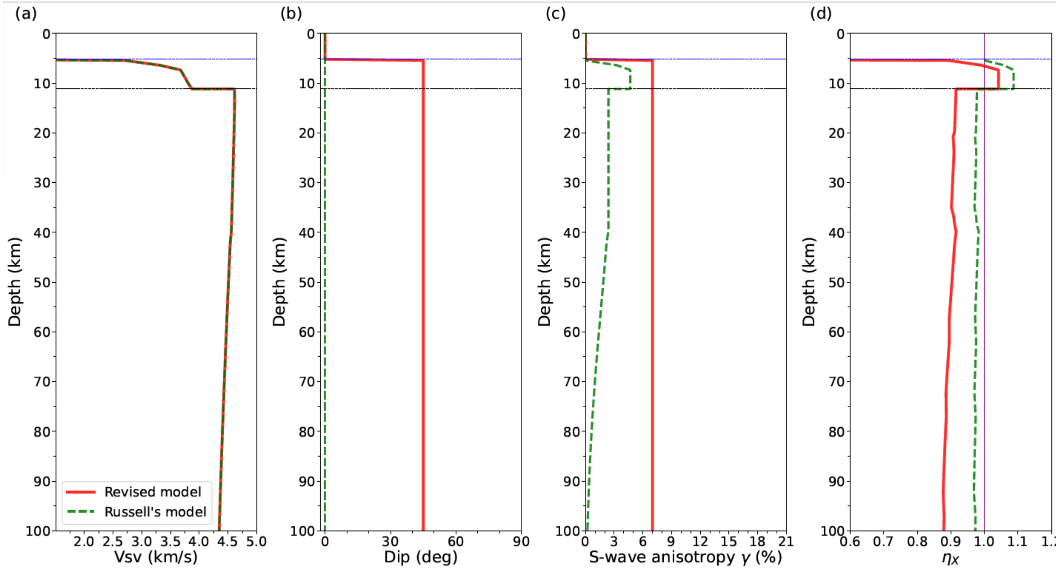

Figure 17. Aspects of the effective transverse isotropy (VTI) component of the oceanic anisotropy model from Data Source 3 is shown with the green dashed line. The red line is our revision of this model in which the moduli A and N are increased so that $(A - C)/2C = (N - L)/2L = 7\%$ and we tilt the elastic tensor through dip angle $\theta = 45°$. (a) $V_{SV} = L/\rho^2$. (b) Dip angle θ. (c) S-wave anisotropy, $\gamma = (N - L)/2L$. (d) Ellipticity parameter $\eta_X = 4L/(A + C - 2F)$.

We show aspects of Russell's model and our revisions in **Figure 17**. The increase in the strength of anisotropy moves η_X farther from 1, making the anisotropy less elliptical. The coupling strength S between fundamental Love and Rayleigh modes is weaker than in continental areas, but the coupling between the fundamental Love and 1st-overtone Rayleigh modes is much stronger from 10 - 40 s period (**Figure 16**b). Coupling strength between the fundamental Love and 2nd-overtone Rayleigh modes is also shown in **Figure 16**b, but strong coupling is confined to a narrower band between about 5 and 15 s period.

In conclusion, at most continental locations, fundamental Loves waves will be coupled principally to fundamental mode Rayleigh waves, and Love wave - overtone coupling can be safely ignored. At oceanic locations, however, fundamental mode Loves waves will be coupled principally to overtone Rayleigh waves, at least below 40 s period, and coupling to the fundamental mode Rayleigh wave will be weaker but still substantial.

6.3 Polarization

Tanimoto (2004) stressed the potential importance of measuring the polarization angle Φ, the tilt angle out of the horizontal plane of the particle motion for quasi-Love waves, as a new constraint on anisotropy. The polarization angle will vary with azimuth and maximize in the fast direction for the

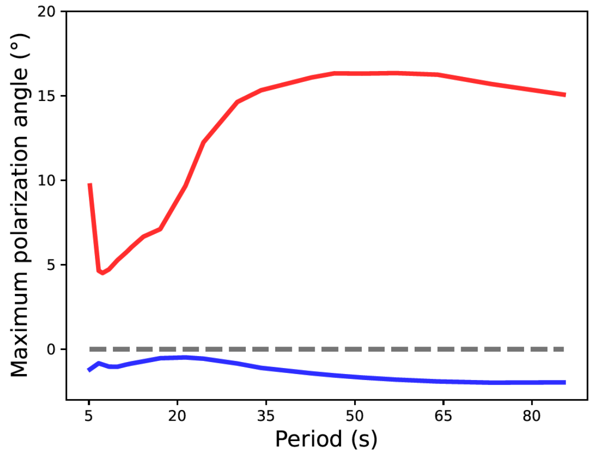

Figure 18. Maximum polarization angle Φ plotted versus period for coupling between the fundamental mode Love wave and the fundamental mode Rayleigh wave (red line) and 1st overtone Rayleigh wave (blue line). Computed in a continental setting (western Alaska, 64°N, 159°W) using anisotropy Model 3, aspects of which are shown in **Figure 15**.

2ψ quasi-Love wave (if the Love wave is faster than the Rayleigh wave). The maximum polarization angle is expected to coincide with the maximum coupling between the Rayleigh and Love waves as shown in **Figure 12**. Its measurement, at the very least, would be a valuable consistency check on anisotropy constrained by phase speeds, with its maximum aligning with the quasi-Love 2ψ fast direction. Its measurement, however, could be used directly in inversions for the depth-dependent elastic. As mentioned in section 5.5, a unique constraint from polarization anisotropy is to infer the absolute tilt direction of a medium.

Figure 18 presents the maximum polarization angle plotted as a function of period for Model 3 in western Alaska for the quasi-Love wave coupled to the fundamental mode Rayleigh wave and the 1st overtone Rayleigh wave. Not surprisingly, these curves look similar to the coupling strength plotted in **Figure 16**a. A polarization anomaly of 15° is expected at this location at periods longer than about 30 s. The polarization anomaly for coupling the Love wave to the first-overtone Rayleigh wave is much smaller and we believe it can be safely ignored in most cases. We believe this is a typical result for Alaska and probably for other continental locations as well.

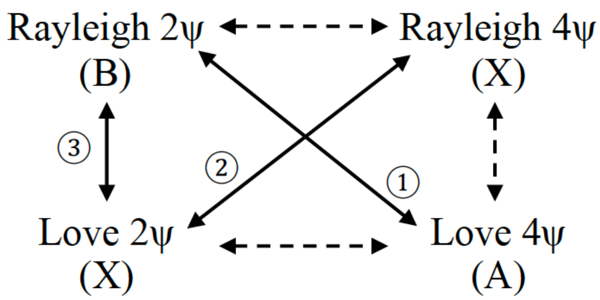

Figure 19. Possible comparisons of fast-axis orientations for different anisotropy measurements from Rayleigh and Love waves. Solid lines numbered 1 - 3 indicate the most informative comparisons. The letters in parentheses refer to integral kernels in equations (5.3) - (5.6) and indicate the dominant sensitivity of each type of measurement.

6.4 Lessons from body waves and observations that may benefit observers

We discuss here three principal lessons that may help to illuminate surface wave observations, where we particularly seek guidance from the body wave theory.

(1) The body waves qS_1 and qS_2 are similar to the quasi-Rayleigh and quasi-Love waves in their sensitivity to particular elastic parameters. Inspection of equations (4.27)-(4.29) for body waves shows that the phase speed of qS_1 will go as B_{33} modified by B_{23} through SV-SH coupling given by equation (4.28) and qS_2 will go like B_{22} modified by B_{23}. Because the anisotropy parameters $G_s = E_s = M_s = D_s$ = 0 in a TTI medium, and $M_c >> D_c$ in earth materials, the azimuthal variation of qS_1 is expected to be approximately governed by G_c and qS_2 by E_c with SV-SH coupling modifications governed by M_c. Surface waves are similar. Inspection of equations (5.3)-(5.6) for surface waves shows that the phase speed of quasi-Love waves will go like integral A modified by integral X through Rayleigh-Love coupling given by equation (5.8) and quasi-Rayleigh waves will go like integral B modified by integral X, recalling that $X >> E$. The A integral is dominated by the W^2 kernel, the B integral by $(U - V'/k)^2$, and the X integral by $W(U - V'/k)$. These kernels are multiplied by G_c, E_c, and M_c, respectively. Thus, the quasi-surface waves have similar sensitivities to the anisotropy parameters as the body waves. This similarity is complicated by the depth-integrals.

The principal motivation for this paper is to explain the existence of a 2ψ signal for quasi-Love waves as arising from Rayleigh-Love coupling. Another way to understand this is the transfer of 2ψ amplitude from Rayleigh to Love waves by considering the analytic results for body waves as the total amplitude of 2ψ G_c (equation (S25)) splitting into two components: C_2 for quasi-S_1 (equation (4.34)) and B_2 for quasi-S_2 (equation (4.36)).

(2) Useful information, particularly for observers, may be gathered by comparing the fast-axis

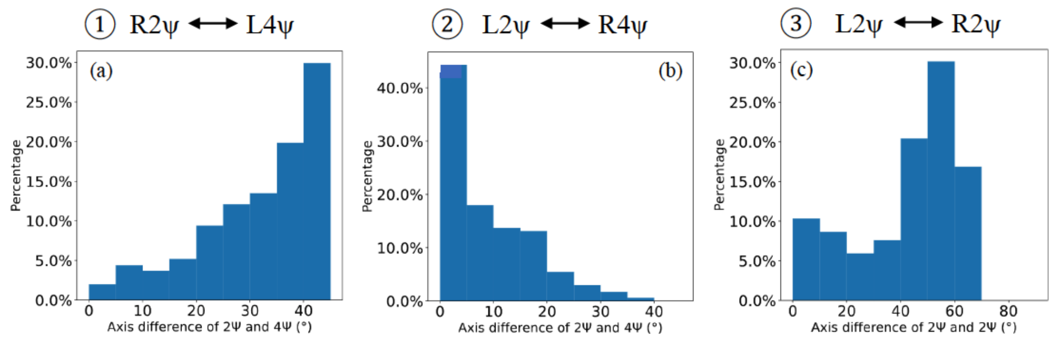

Figure 20. Histograms presenting the difference between the fast orientations of different measurements across Alaska, from Data Source 4. (a) 38 s period Love wave 2ψ fast direction compared with the 50 s period Rayleigh wave 4ψ fast direction. (b) 14 s Rayleigh wave 2ψ fast direction compared to the 20 s period Love wave 4ψ fast direction. (c) Rayleigh wave 2ψ fast direction compared to the Love wave 2ψ fast direction, both at 40 s period.

directions of different surface wave observations. In some of these comparisons, it is illuminating to compare quasi-Rayleigh to qS_1 and quasi-Love to qS_2 and use the body wave results as guidance.

Figure 19 schematically represents with arrows the six comparisons that can be made between the fast-axis directions of various observation types: Rayleigh 2ψ, Rayleigh 4ψ, Love 2ψ, and Love 4ψ denoted as $R_{2\psi}$, $R_{4\psi}$, $L_{2\psi}$, and $L_{4\psi}$. There are more comparisons because they can be made at different periods. The most interpretable comparisons are between measurement types that have similar vertical sensitivity kernels. As mentioned in the previous paragraph, the vertical sensitivity of $R_{2\psi}$ is dominated by the $(U - V'/k)^2$ kernel in integral B of equation (5.4). Similarly, the sensitivities of $R_{4\psi}$ and $L_{2\psi}$ are dominated by the $W(U - V'/k)$ kernel in integral X of equation (5.6) and $L_{4\psi}$ is dominated by the W^2 kernel in integral A of equation (5.3). These sensitivities are also represented in **Figure 19**.

Figure 19 identifies the suggested comparisons with solid lines, which allow $R_{4\psi}$, $L_{2\psi}$, and $L_{4\psi}$ to be assessed relative to $R_{2\psi}$. We present statistics here from a preliminary measurement of these quantities based on ambient noise tomography acoss Alaska from Data Source 4. **Figure 20** shows histograms of differences of fast axis estimates across Alaska for: (1) $R_{2\psi}$ and $L_{4\psi}$, (2) $R_{4\psi}$ and $L_{2\psi}$, and (3) $R_{2\psi}$ and $L_{2\psi}$. The differences are computed where the amplitude is greater than 0.5% for 2ψ anisotropy and greater than 0.3% for 4ψ anisotropy and the uncertainty in the fast axis direction is less than 15°.

The first comparison is between $R_{2\psi}$ and $L_{4\psi}$ which have different sensitivities, but the comparison is justified if both waves have their sensitivities compressed into the crust. Therefore, the comparison is most informative at short periods. This comparison is illuminated by the body wave results presented in **Figure 9**, which shows that for for a TTI medium, the absolute value of the fast axis direction between qS_1 2ψ and qS_2 4ψ will be either $0°$ or $45°$, and it will be governed by the sign of $1 - \eta_X$. If $\eta_X > 1$, then the difference in fast axis directions will be $0°$ and if $\eta_X < 1$ it will be $\pm 45°$. We show a histogram of the difference in fast axis directions for $R_{2\psi}$ and $L_{4\psi}$ across Alaska in **Figure 20**a for the 14 s Rayleigh wave and 20 s Love wave. The comparison illustrates that the fast axis differences of these observations cluster near 45°. This observation is consistent with $\eta_X < 1$ in the crust, which is what is expected for crustal materials (**Fig. S.2**, supplementary materials).

The second comparison is between $R_{4\psi}$ and $L_{2\psi}$ both with sensitivities that are dominated by integral X. This comparison should be performed between waves with approximately the same wavelength (the quasi-degeneracy condition). We find that across Alaska, **Figure 20**b, differences in the quasi-Rayleigh 4ψ and quasi-Love 2ψ fast directions cluster near 0°. Thus, in Alaska these fast axes align (or are parallel) predominantly. Because qS_1 does not have a 4ψ component, we are not guided directly by the body wave results for this comparison. Rather we note that when integral X is squared, the $L_{2\psi}$ coefficient will depend largely on M_c^2 and the $R_{4\psi}$ amplitude on $M_c D_c$, which may differ in sign from M_c^2. Thus, the difference in fast axis directions between $R_{4\psi}$ and $L_{2\psi}$ may be either $0°$ or $45°$. Our observations are consistent with this prediction, but in this case we obtain no information about η_X. However, as argued earlier, ignoring Love wave 2ψ will have a strong impact on estimates of radial anisotropy, while ignoring Rayleigh wave 4ψ will have a significant impact on estimates of η_X. So this observation and comparison is useful to check the reliability of the observations.

The third comparison between $R_{2\psi}$ and $L_{2\psi}$ is the most difficult, but is still informative. This might appear to be the most obvious comparison, but it is complicated for practical reasons. It will be most useful at long periods because Love wave 2ψ observations are strongest there. At long periods, however, the differences between the sensitivity kernels are accentuated. In **Figure 20**c, the comparison is performed at 40 s period. At this period, observations show that the fast axis directions for $R_{2\psi}$ and $L_{2\psi}$ are neither parallel nor perpendicular, but mostly appear at intermediate angles between these extremes. Inversion results, which we do not include here, show that these observations can be reconciled with the strike direction varying in a physically reasonable way with depth. Therefore, the comparison of these observations cannot be used simply to test the $L_{2\psi}$ observation, but the use of the fast axes observations simultaneously in the inversion provides important information to constrain the depth variation of the strike direction.

The guidance from body waves is that if anisotropy is constant with depth, then their fast directions should be either parallel or perpendicular, with the Love wave 2ψ fast axis aligned with the strike direction. The results are summarized in **Table 4** with the assumption that Rayleigh-Love coupling does not change the sign of Rayleigh wave 2ψ variation. The left column holds for Western Alaska and the right column holds for Eastern Alaska. Assuming that the quasi-Love wave is faster than the quasi-Rayleigh wave, that $M_s = D_s = 0$, and that for a TTI medium azimuth ψ is measured relative to the x-axis and the strike direction is along the y-axis (ψ =90°), we have from equation (4.17)

$$B_{23}^2 \approx \frac{1}{2}(M_c^2 + D_c^2) - (\frac{1}{2}M_c^2 - M_c D_c)\cos 2\psi + \text{higher order terms} \tag{6.1}$$

In Data Source 1, $\frac{1}{2}M_c^2 - M_c D_c > 0$ in 82 of the 93 samples with a dip angle $\theta = 45°$ and for all points across Alaska. This indicates the fast axis inferred from equation (6.1) is mostly at 90° and therefore the Love wave 2ψ fast axis always aligns with the strike direction (y-axis). If $G_c > 0$, as in Western Alaska, the 2ψ term in $(A - B)^2$ will minimize at 0° azimuth, be perpendicular to Love wave 2ψ fast axis (black dashed line in **Figure 12**a), and cause an overestimation of Rayleigh wave 2ψ amplitude (as shown in **Figure 11**b and c). If $G_c < 0$, as in Eastern Alaska, the 2ψ term in $(A - B)^2$ will minimize at 90° azimuth, be parallel to Love wave 2ψ fast axis (B_{23}^2 or X^2) (black dashed line in **Figure 12**d), and cause an underestimation of Rayleigh wave 2ψ amplitude (as shown in **Figure 11**e and f). For a tilted orthorhombic elastic tensor, the fast axes of Rayleigh wave 2ψ and Love wave 2ψ should align with the principal axes of the orthorhombic medium.

Table 4. Fast axis relationship of 2ψ azimuthal anisotropy and strike direction.

Axis difference	Rayleigh $2\psi (G_c > 0)$	Rayleigh 2ψ $(G_c < 0)$
Love 2ψ	perpendicular	parallel
Strike	perpendicular	parallel

(3) The third lesson concerns coupling between Rayleigh and Love overtones. As shown in **Figure 5**, in both continental and oceanic regions Rayleigh and Love wave overtones are nearly degenerate. This means that they have very similar sensitivity kernels with $|W| \approx |U - V'/k|$. In this case, the application of body wave theory will be much more straightforward than for coupling between the fundamental modes. Further analysis may discover constraints to estimate η_X and the dip angle θ in certain depth intervals for a TTI medium directly from observations similar to body waves. Also, in near-degenerate cases, we cannot simply assign a plus or minus sign to a single quasi-surface wave (equation (5.8)). Dealing with this complicated situation should follow a similar derivation as we do for body waves in a TTI medium (Supplementary Materials section S.2).

7 CONCLUSIONS

We present a quasi-degenerate theory of Rayleigh-Love coupling based on the application of Hamilton's Principle to Rayleigh and Love waves. This theory explains the observation of 2ψ phase velocity anisotropy for Love waves and 4ψ anisotropy for Rayleigh waves. Previous theories based on non-degenerate perturbation theory (Smith & Dahlen 1973; Montagner & Nataf 1986) do not explain these observations, and for this reason we refer to 2ψ anisotropy for Love waves and 4ψ anisotropy for Rayleigh waves as "unexpected". The reason for this is that these theories do not model the coupling of Rayleigh and Love waves by anisotropy. The quasi-degenerate theory we present here does model Rayleigh-Love coupling and succeeds to explain observations of 2ψ anisotropy for Love waves. In addition, it allows for these observations to be included in inversions simultaneously with "expected" observations, such as the 2ψ anisotropy for Rayleigh waves and the 4ψ anisotropy for Love waves.

For comparison, we also present a theory of SV-SH coupling for horizontally propagating body waves to help illuminate Rayleigh-Love coupling. We apply Hamilton's Principle to develop this theory, too, which generates the same results as the degenerate perturbation theory of Jech & Pšenčík (1989). However, we specialize the results by applying them to a tilted transversely isotropic (TTI) medium, which is commonly assumed in inversions for anisotropy (e.g. Xie *et al*. 2015), and present simple expressions for the anisotropy of the quasi-S waves based on the dip angle θ of anisotropy and the ellipticity parameter η_X, which we introduce here. We show how observations of phase speed anisotropy of the quasi-S waves can be used to infer η_X and θ as well the polarization angle Φ for the coupled quasi-S waves.

We present examples that illustrate that when the unexpected 2ψ anisotropy for Love waves is included in inversions for a depth-dependent TTI medium along with observations of expected anisotropy, better constraints are placed on the ellipticity parameter η_X, but the amplitude of anisotropy in the mantle may become so large as to be physically unrealistic. We find that using an orthorhombic tensor in the mantle greatly reduces the amplitude of anisotropy, and advise that future inversions should use a tilted orthorhombic tensor in the mantle.

Tanimoto (2004) suggested that polarization measurements for coupled quasi-Love and quasi-Rayleigh waves should be considered as new information to constrain anisotropy within the Earth. We would like to second this suggestion, particularly because the quasi-degenerate theory we present predicts stronger Rayleigh-Love coupling and therefore stronger polarization anomalies than the theory presented by Tanimoto (2004). We present evidence that polarization anomalies, or tilts of the quasi-Love wave's particle motion out of the horizontal plane of 15° should be common in a continental setting, in particular at periods sensitive to the mantle.

Maupin (2004) raised the important point that the coupling between the fundamental mode Love wave and the first and higher overtone Rayleigh waves may also be important, particularly in oceanic settings. We provide evidence that coupling between the fundamental Love wave and Rayleigh overtones can probably be ignored in continental settings. However, coupling between the fundamental Love wave and both fundamental and overtone Rayleigh waves are likely to be strong in oceanic settings.

Our results indicate that greater efforts are needed in both continental and oceanic settings to observe unexpected anisotropy such as Love wave 2ψ anisotropy. Such observations would be important to improve models of anisotropy that are deriving from the inversion of isotropic Rayleigh and Love wave phase speeds along with the 2ψ component of Rayleigh wave anisotropy (e.g. Xie *et al*. 2015, 2017; C. Liu & Ritzwoller 2024).

The theory presented in this paper is derived in Cartesian coordinates and ignores finite frequency effects, for example arising from Rayleigh-Love scattering away from the receiver (e.g. Maupin 2001; Sieminski *et al*. 2007, 2009). Non-degenerate perturbation theory has been derived in spherical coordinates (e.g. Larson *et al*. 1998) and the typical method to deal with finite-frequency effects is the first Born approximation (e.g. Snieder 1986; Snieder & Nolet 1987). However, due to the strong mode coupling between Rayleigh and Love waves discussed in this paper, this standard Born approximation needs to be revised to account accurately for strong interactions caused by quasi-degeneracy. This problem is solved in normal modes by considering coupling between multiplets (e.g. Park 1990; Tromp & Dahlen 1990; Su *et al*. 1993). Future efforts in this topic should consider extension to spherical coordinates, the inclusion of finite frequency effects, and coupling between multiple modes (> 2) because surface waves can strongly couple to fundamental modes and overtone surface waves at the same time.

APPENDIX A: ELASTIC TENSOR IN VARIOUS MEDIA

The elastic tensor $c_{ijk\ell}$ can be written in abbreviated or Voigt notation as a symmetric 6×6 matrix C_{mn} such that each pair of indices (ij) is replaced with a single index m according to the following rule: if $i = j$ then $m = i$ and if $i \neq j$ then $m = 9 - (i + j)$. A general elastic tensor can then be visualized as follows

$$C_{mn} = \begin{bmatrix} C_{11} & C_{12} & C_{13} & C_{14} & C_{15} & C_{16} \\ C_{12} & C_{22} & C_{23} & C_{24} & C_{25} & C_{26} \\ C_{13} & C_{23} & C_{33} & C_{34} & C_{35} & C_{36} \\ C_{14} & C_{24} & C_{34} & C_{44} & C_{45} & C_{46} \\ C_{15} & C_{25} & C_{35} & C_{45} & C_{55} & C_{56} \\ C_{16} & C_{26} & C_{36} & C_{46} & C_{56} & C_{66} \end{bmatrix} \tag{A.1}$$

For an isotropic elastic tensor

$$c_{ijk\ell}^{isotropic} = \lambda \delta_{ij} \delta_{k\ell} + \mu(\delta_{ik}\delta_{j\ell} + \delta_{i\ell}\delta_{jk}), \tag{A.2}$$

the elastic tensor can be visualized as follows

$$C_{mn}^{isotropic} = \begin{bmatrix} \lambda + 2\mu & \lambda & \lambda & 0 & 0 & 0 \\ \lambda & \lambda + 2\mu & \lambda & 0 & 0 & 0 \\ \lambda & \lambda & \lambda + 2\mu & 0 & 0 & 0 \\ 0 & 0 & 0 & \mu & 0 & 0 \\ 0 & 0 & 0 & 0 & \mu & 0 \\ 0 & 0 & 0 & 0 & 0 & \mu \end{bmatrix} \tag{A.3}$$

Similarly, the elastic tensor for a transversely isotropic medium with a vertical symmetry axis, or a VTI medium, can be written as

$$C_{mn}^{VTI} = \begin{bmatrix} A & A - 2N & F & 0 & 0 & 0 \\ A - 2N & A & F & 0 & 0 & 0 \\ F & F & C & 0 & 0 & 0 \\ 0 & 0 & 0 & L & 0 & 0 \\ 0 & 0 & 0 & 0 & L & 0 \\ 0 & 0 & 0 & 0 & & N \end{bmatrix} \tag{A.4}$$

where A, C, N, L and F are the five Love moduli, and sometimes F is replaced by the form factor $\eta = F/(A - 2L)$. (In some places, η is defined as $(A - 2L)/F$.)

To produce a tilted transversely isotropic medium, the symmetry axis of the VTI medium is rotated through a dip angle θ around the y-axis as follows

$$\mathbf{C}^{TTI} = \mathbf{B}\mathbf{C}^{VTI}\mathbf{B}^T \tag{A.5}$$

where $\mathbf{B}$ is the Bond matrix and $\mathbf{B}^T$ is its transpose. Sometimes we refer to the y-axis as the "strike axis". The components of the elastic tensor for the TTI medium are

$$C_{11}^{TTI} = A\cos^4\theta + C\sin^4\theta + (2F+4L)\sin^2\theta\cos^2\theta \tag{A.6}$$

$$C_{22}^{TTI} = A \tag{A.7}$$

$$C_{33}^{TTI} = A\sin^4\theta + C\cos^4\theta + (2F+4L)\sin^2\theta\cos^2\theta \tag{A.8}$$

$$C_{44}^{TTI} = L\cos^2\theta + N\sin^2\theta \tag{A.9}$$

$$C_{55}^{TTI} = (A+C-2F)\sin^2\theta\cos^2\theta + L(\cos^2\theta - \sin^2\theta)^2 \tag{A.10}$$

$$C_{66}^{TTI} = L\sin^2\theta + N\cos^2\theta \tag{A.11}$$

$$C_{12}^{TTI} = C_{21}^{TTI} = (A-2N)\cos^2\theta + F\sin^2\theta \tag{A.12}$$

$$C_{13}^{TTI} = C_{31}^{TTI} = (A+C-4L)\sin^2\theta\cos^2\theta + F(\sin^4\theta + \cos^4\theta) \tag{A.13}$$

$$C_{15}^{TTI} = C_{51}^{TTI} = (F+2L-A)\sin\theta\cos^3\theta - (F+2L-C)\sin^3\theta\cos\theta \tag{A.14}$$

$$C_{23}^{TTI} = C_{32}^{TTI} = (A-2N)\sin^2\theta + F\cos^2\theta \tag{A.15}$$

$$C_{25}^{TTI} = C_{52}^{TTI} = (F+2N-A)\sin\theta\cos\theta \tag{A.16}$$

$$C_{35}^{TTI} = C_{53}^{TTI} = (F+2L-A)\sin^3\theta\cos\theta - (F+2L-C)\sin\theta\cos^3\theta \tag{A.17}$$

$$C_{46}^{TTI} = C_{64}^{TTI} = (L-N)\sin\theta\cos\theta \tag{A.18}$$

$$C_{14}^{TTI} = C_{16}^{TTI} = C_{24}^{TTI} = C_{26}^{TTI} = C_{34}^{TTI} = C_{36}^{TTI} = C_{45}^{TTI} = C_{56}^{TTI} = 0 \tag{A.19}$$

Only 13 of the 21 components of the elastic tensor for a TTI medium are independent. These 13 components form a monoclinic elastic solid.

For a transversely isotropic medium with a horizontal symmetry axis, $\theta = 90°$, so

$$C_{mn}^{HTI} = \begin{bmatrix} C & F & F & 0 & 0 & 0 \\ F & A & A-2N & 0 & 0 & 0 \\ F & A-2N & A & 0 & 0 & 0 \\ 0 & 0 & 0 & N & 0 & 0 \\ 0 & 0 & 0 & 0 & L & 0 \\ 0 & 0 & 0 & 0 & 0 & L \end{bmatrix} \tag{A.20}$$

APPENDIX B: THE 21 ANISOTROPIC PARAMETERS

Montagner & Nataf (1986) introduced linear recombinations of the elastic tensor components for surface waves. Chen & Tromp (2007) introduced others that also are needed for body waves. We follow Chen & Tromp (2007) by including the negative sign in the definition of G_s, B_s, H_s and E_s:

$$\begin{aligned}
\mathcal{A} &= \frac{1}{8}(3C_{11}+3C_{22}+2C_{12}+4C_{66}) && \text{(B.1)}\\
\mathcal{C} &= C_{33} && \text{(B.2)}\\
\mathcal{N} &= \frac{1}{8}(C_{11}+C_{22}-2C_{12}+4C_{66}) && \text{(B.3)}\\
\mathcal{L} &= \frac{1}{2}(C_{44}+C_{55}) && \text{(B.4)}\\
\mathcal{F} &= \frac{1}{2}(C_{13}+C_{23}) && \text{(B.5)}\\
J_c &= \frac{1}{8}(3C_{15}+C_{25}+2C_{46}) && \text{(B.6)}\\
J_s &= \frac{1}{8}(C_{14}+3C_{24}+2C_{56}) && \text{(B.7)}\\
K_c &= \frac{1}{8}(3C_{15}+C_{25}+2C_{46}-4C_{35}) && \text{(B.8)}\\
K_s &= \frac{1}{8}(C_{14}+3C_{24}+2C_{56}-4C_{34}) && \text{(B.9)}\\
M_c &= \frac{1}{4}(C_{15}-C_{25}+2C_{46}) && \text{(B.10)}\\
M_s &= \frac{1}{4}(C_{14}-C_{24}-2C_{56}) && \text{(B.11)}\\
G_c &= \frac{1}{2}(C_{55}-C_{44}) && \text{(B.12)}\\
G_s &= -C_{45} && \text{(B.13)}\\
B_c &= \frac{1}{2}(C_{11}-C_{22}) && \text{(B.14)}\\
B_s &= -(C_{16}+C_{26}) && \text{(B.15)}\\
H_c &= \frac{1}{2}(C_{13}-C_{23}) && \text{(B.16)}\\
H_s &= -C_{36} && \text{(B.17)}\\
D_c &= \frac{1}{4}(C_{15}-C_{25}-2C_{46}) && \text{(B.18)}\\
D_s &= \frac{1}{4}(C_{14}-C_{24}+2C_{56}) && \text{(B.19)}\\
E_c &= \frac{1}{8}(C_{11}+C_{22}-2C_{12}-4C_{66}) && \text{(B.20)}\\
E_s &= -\frac{1}{2}(C_{16}-C_{26}) && \text{(B.21)}
\end{aligned}$$

We use the script notation for $\mathcal{A}, \mathcal{C}, \mathcal{N}, \mathcal{L}$ and $\mathcal{F}$ to distinguish them from the Love moduli A, C, N, L and F that define a VTI medium, which is the basis for producing the elastic tensor for a TTI medium in Appendix A.

J_c (J_s), K_c (K_s) and M_c (M_s) are body wave 1ψ azimuthal anisotropy parameters and D_c (D_s) is the body wave 3ψ azimuthal anisotropy parameter, which were not included by Montagner & Nataf (1986). G_c (G_s), B_c (B_s) and H_c (H_s) are 2ψ azimuthal anisotropic parameters for both body waves and surface waves. E_c (E_s) is the 4ψ azimuthal anisotropic parameter for both body waves and surface waves.

For a TTI medium, all parameters with the "s" subscript are zero, so 13 of the anisotropic parameters are non-zero, forming a medium with monoclinic symmetry.

Acknowledgements

We are grateful to Sarah Brownlee for valuable conversations and for providing the database of elastic tensor measurements (Brownlee *et al*. 2017). We also thank Chuanming Liu for many helpful conversations and for providing his model of the depth-dependent elastic tensor beneath Alaska (C. Liu & Ritzwoller 2024). XL also thanks Chuanming Liu for guidance in data processing. We greatly appreciate help from IRIS Data Services, which are funded through the Seismological Facilities for the Advancement of Geoscience and EarthScope (SAGE) Proposal of the National Science Foundation under Cooperative Agreement EAR-1851048. Aspects of this research were supported by EAR-1537868, EAR-1928395 and EAR-1952209 at the University of Colorado Boulder.

REFERENCES

Aki, K. & Richards, P. G., 2002. *Quantitative seismology*.

Backus, G. E., 1965. Possible forms of seismic anisotropy of the uppermost mantle under oceans, *Journal of Geophysical Research*, **70**(14), 3429–3439.

Becker, T. W., Chevrot, S., Schulte-Pelkum, V., & Blackman, D. K., 2006. Statistical properties of seismic anisotropy predicted by upper mantle geodynamic models, *Journal of Geophysical Research: Solid Earth*, **111**(B8).

Browaeys, J. T. & Chevrot, S., 2004. Decomposition of the elastic tensor and geophysical applications, *Geophysical Journal International*, **159**(2), 667–678.

Brownlee, S. J., Schulte-Pelkum, V., Raju, A., Mahan, K., Condit, C., & Orlandini, O. F., 2017. Characteristics of deep crustal seismic anisotropy from a compilation of rock elasticity tensors and their expression in receiver functions, *Tectonics*, **36**(9), 1835–1857.

Chen, M. & Tromp, J., 2007. Theoretical and numerical investigations of global and regional seismic wave propagation in weakly anisotropic earth models, *Geophysical Journal International*, **168**(3), 1130–1152.

Dahlen, F. & Tromp, J., 2020. Theoretical global seismology, in *Theoretical Global Seismology*, Princeton university press.

Forsyth, D. W., 1975. The early structural evolution and anisotropy of the oceanic upper mantle, *Geophysical Journal International*, **43**(1), 103–162.

Ismaıl, W. B. & Mainprice, D., 1998. An olivine fabric database: an overview of upper mantle fabrics and seismic anisotropy, *Tectonophysics*, **296**(1-2), 145–157.

Jech, J. & Pšenčík, I., 1989. First-order perturbation method for anisotropic media, *Geophysical Journal International*, **99**(2), 369–376.

Kawakatsu, H., 2016. A new fifth parameter for transverse isotropy, *Geophysical Journal International*, **204**(1), 682–685.

Larson, E. W., Tromp, J., & Ekström, G., 1998. Effects of slight anisotropy on surface waves, *Geophysical Journal International*, **132**(3), 654–666.

Lin, F.-C., Ritzwoller, M. H., & Snieder, R., 2009. Eikonal tomography: surface wave tomography by phase front tracking across a regional broad-band seismic array, *Geophysical Journal International*, **177**(3), 1091–1110.

Lin, F.-C., Ritzwoller, M. H., Yang, Y., Moschetti, M. P., & Fouch, M. J., 2011. Complex and variable crustal and uppermost mantle seismic anisotropy in the western United States, *Nature Geoscience*, **4**(1), 55–61.

Liu, C. & Ritzwoller, M. H., 2024. Seismic anisotropy and deep crustal deformation across Alaska, *Journal of Geophysical Research: Solid Earth*, **129**(5), e2023JB028525.

Liu, C., Zhang, S., Sheehan, A. F., & Ritzwoller, M. H., 2022. Surface wave isotropic and azimuthally anisotropic dispersion across Alaska and the Alaska-Aleutian subduction zone, *Journal of Geophysical Research: Solid Earth*, **127**(11), e2022JB024885.

Liu, X., Liu, C., & Ritzwoller, M. H., 2024. Observations of Rayleigh and Love wave anisotropy across

Alaska, *Manuscript in preparation*.

Maupin, V., 1989. Surface waves in weakly anisotropic structures: on the use of ordinary or quasi-degenerate perturbation methods, *Geophysical Journal International*, **98**(3), 553–563.

Maupin, V., 2001. A multiple-scattering scheme for modelling surface wave propagation in isotropic and anisotropic three-dimensional structures, *Geophysical Journal International*, **146**(2), 332–348.

Maupin, V., 2004. Comment on 'The azimuthal dependence of surface wave polarization in a slightly anisotropic medium' by T. Tanimoto, *Geophysical Journal International*, **159**(1), 365–368.

Montagner, J.-P. & Jobert, N., 1988. Vectorial tomography—ii. Application to the Indian Ocean, *Geophysical Journal International*, **94**(2), 309–344.

Montagner, J.-P. & Nataf, H.-C., 1986. A simple method for inverting the azimuthal anisotropy of surface waves, *Journal of Geophysical Research: Solid Earth*, **91**(B1), 511–520.

Montagner, J.-P. & Tanimoto, T., 1990. Global anisotropy in the upper mantle inferred from the regionalization of phase velocities, *Journal of Geophysical Research: Solid Earth*, **95**(B4), 4797–4819.

Nishimura, C. E. & Forsyth, D. W., 1988. Rayleigh wave phase velocities in the Pacific with implications for azimuthal anisotropy and lateral heterogeneities, *Geophysical Journal International*, **94**(3), 479–501.

Park, J., 1990. The subspace projection method for constructing coupled-mode synthetic seismograms, *Geophysical Journal International*, **101**(1), 111–123.

Russell, J. B., Gaherty, J. B., Lin, P.-Y. P., Lizarralde, D., Collins, J. A., Hirth, G., & Evans, R. L., 2019. High-resolution constraints on Pacific upper mantle petrofabric inferred from surface-wave anisotropy, *Journal of Geophysical Research: Solid Earth*, **124**(1), 631–657.

Sieminski, A., Liu, Q., Trampert, J., & Tromp, J., 2007. Finite-frequency sensitivity of surface waves to anisotropy based upon adjoint methods, *Geophysical Journal International*, **168**(3), 1153–1174.

Sieminski, A., Trampert, J., & Tromp, J., 2009. Principal component analysis of anisotropic finite-frequency sensitivity kernels, *Geophysical Journal International*, **179**(2), 1186–1198.

Smith, M. L. & Dahlen, F., 1973. The azimuthal dependence of Love and Rayleigh wave propagation in a slightly anisotropic medium, *Journal of Geophysical Research*, **78**(17), 3321–3333.

Snieder, R., 1986. 3-d linearized scattering of surface waves and a formalism for surface wave holography, *Geophysical Journal International*, **84**(3), 581–605.

Snieder, R., Nolet, G., et al., 1987. Linearized scattering of surface waves on a spherical Earth, *Journal of Geophysics*, **61**(1), 55–63.

Su, L., Park, J., & Yu, Y., 1993. Born seismograms using coupled free oscillations: the effects of strong coupling and anisotropy, *Geophysical Journal International*, **115**(3), 849–862.

Tanimoto, T., 2004. The azimuthal dependence of surface wave polarization in a slightly anisotropic medium, *Geophysical Journal International*, **156**(1), 73–78.

Tanimoto, T. & Anderson, D. L., 1985. Lateral heterogeneity and azimuthal anisotropy of the upper mantle: Love and Rayleigh waves 100–250 s, *Journal of Geophysical Research: Solid Earth*, **90**(B2), 1842–1858.

Thomsen, L., 1986. Weak elastic anisotropy, *Geophysics*, **51**(10), 1954–1966.

Trampert, J. & Woodhouse, J. H., 2003. Global anisotropic phase velocity maps for fundamental mode surface waves between 40 and 150 s, *Geophysical Journal International*, **154**(1), 154–165.

Tromp, J. & Dahlen, F., 1990. Summation of the Born series for the normal modes of the Earth, *Geophysical Journal International*, **100**(3), 527–533.

Xie, J., Ritzwoller, M. H., Brownlee, S., & Hacker, B., 2015. Inferring the oriented elastic tensor from surface wave observations: preliminary application across the western United States, *Geophysical Journal International*, **201**(2), 996–1021.

Xie, J., Ritzwoller, M. H., Shen, W., & Wang, W., 2017. Crustal anisotropy across eastern Tibet and surroundings modeled as a depth-dependent tilted hexagonally symmetric medium, *Geophysical Journal International*, **209**(1), 466–491.

Yao, H., van Der Hilst, R. D., & Montagner, J.-P., 2010. Heterogeneity and anisotropy of the lithosphere of SE Tibet from surface wave array tomography, *Journal of Geophysical Research: Solid Earth*, **115**(B12).

Supplementary Materials: The Effect of Rayleigh-Love Coupling in an Anisotropic Medium

S.1 The Body Wave B_{mn} Coefficients for a General Anisotropic Medium

In this section, we make frequent use of the following trigonometric identities:

$$
\begin{aligned}
\cos^4\psi &= \frac{1}{8}\left(3 + 4\cos(2\psi) + \cos(4\psi)\right) \qquad & \sin^4\psi = \frac{1}{8}\left(3 - 4\cos(2\psi) + \cos(4\psi)\right)\\
\cos^3\psi\sin\psi &= \frac{1}{8}\left(2\sin(2\psi) + \sin(4\psi)\right) \qquad & \cos\psi\sin^3\psi = \frac{1}{8}\left(2\sin(2\psi) - \sin(4\psi)\right)\\
\sin^2\psi\cos^2\psi &= \frac{1}{8}\left(1 - \cos(4\psi)\right) & \\
\cos^3\psi &= \frac{1}{4}\left(3\cos(\psi) + \cos(3\psi)\right) \qquad & \sin^3\psi = \frac{1}{4}\left(3\sin(\psi) - \sin(3\psi)\right)\\
\cos^2\psi\sin\psi &= \frac{1}{4}\left(\sin(\psi) + \sin(3\psi)\right) \qquad & \cos\psi\sin^2\psi = \frac{1}{4}\left(\cos(\psi) - \cos(3\psi)\right)
\end{aligned}
$$

The B_{mn} coefficients are defined by equation (4.12), where the Christoffel matrix M_{ik} is defined by equation (4.3). Specifying the horizontal direction of propagation ($n_1 = \cos\psi, n_2 = \sin\psi, n_3 = 0$), the Christoffel matrix in terms of the elastic moduli is

$$
\begin{aligned}
\rho M_{11} &= C_{11}\cos^2\psi + C_{66}\sin^2\psi + 2C_{16}\cos\psi\sin\psi\\
\rho M_{22} &= C_{66}\cos^2\psi + C_{22}\sin^2\psi + 2C_{26}\cos\psi\sin\psi\\
\rho M_{33} &= C_{55}\cos^2\psi + C_{44}\sin^2\psi + 2C_{45}\cos\psi\sin\psi\\
\rho M_{12} &= \rho\tilde{M}_{21} = C_{16}\cos^2\psi + C_{26}\sin^2\psi + (C_{12} + C_{66})\cos\psi\sin\psi\\
\rho M_{13} &= \rho\tilde{M}_{31} = C_{15}\cos^2\psi + C_{46}\sin^2\psi + (C_{14} + C_{56})\cos\psi\sin\psi\\
\rho M_{23} &= \rho\tilde{M}_{32} = C_{56}\cos^2\psi + C_{24}\sin^2\psi + (C_{25} + C_{46})\cos\psi\sin\psi
\end{aligned}
$$

Now we find B_{11}, B_{22}, B_{33} and B_{23} as follows.

$\mathbf{B_{11}}$: $\hat{\mathbf{a}}^{(1)} = (\cos\psi, \sin\psi, 0)^T$

$$
\begin{aligned}
B_{11}(\psi) = M_{jk}a_k^{(1)}a_j^{(1)} &= M_{11}a_1^{(1)}a_1^{(1)} + M_{22}a_2^{(1)}a_2^{(1)} + M_{33}a_3^{(1)}a_3^{(1)}\\
&\quad +2M_{12}a_2^{(1)}a_1^{(1)} + 2M_{13}a_3^{(1)}a_1^{(1)} + 2M_{23}a_3^{(1)}a_2^{(1)}\\
&= M_{11}\cos^2\psi + M_{22}\sin^2\psi + 2M_{12}\cos\psi\sin\psi
\end{aligned}
$$

$$\begin{aligned}
\rho B_{11}(\psi) &= C_{11}\cos^4\psi + 4C_{16}\cos^3\psi\sin\psi + 2(2C_{66}+C_{12})\cos^2\psi\sin^2\psi \\
&\quad +4C_{26}\cos\psi\sin^3\psi + C_{22}\sin^4\psi \\
&= \frac{1}{8}C_{11}\left(3+4\cos(2\psi)+\cos(4\psi)\right) + \frac{1}{4}(2C_{66}+\hat{C}_{12})\left(1-\cos(4\psi)\right) \\
&\quad +\frac{1}{8}C_{22}\left(3-4\cos(2\psi)+\cos(4\psi)\right) \\
&\quad +\frac{1}{2}C_{16}(2\sin(2\psi)+\sin(4\psi)) + \frac{1}{2}C_{26}(2\sin(2\psi)-\sin(4\psi)) \\
&= \left(A_0 + A_{2c}\cos(2\psi) + A_{2s}\sin(2\psi) + A_{4c}\cos(4\psi) + A_{4s}\sin(4\psi)\right) \qquad \text{(S1)}
\end{aligned}$$

where

$$A_0 = \frac{1}{8}\left(3C_{11}+3C_{22}+2C_{12}+4C_{66}\right) \equiv \mathcal{A} \qquad \text{(S2)}$$

$$A_{2c} = \frac{1}{2}(C_{11}-C_{22}) \equiv B_c \qquad \text{(S3)}$$

$$A_{2s} = C_{16}+2C_{26} \equiv -B_s \qquad \text{(S4)}$$

$$A_{4c} = \frac{1}{8}(C_{11}+C_{22}-2C_{12}-4C_{66}) \equiv E_c \qquad \text{(S5)}$$

$$A_{4s} = \frac{1}{2}(C_{16}-C_{26}) \equiv -E_s \qquad \text{(S6)}$$

where $\mathcal{A}$, B_c, B_s, E_c, and E_s are defined in Appendix B.

$\mathbf{B_{22}}$: $\hat{\mathbf{a}}^{(2)} = (-\sin\psi, \cos\psi, 0)^T$

$$\begin{aligned}
B_{22}(\psi) = M_{jk}a_k^{(2)}a_j^{(2)} &= M_{11}a_1^{(2)}a_1^{(2)} + M_{22}a_2^{(2)}a_2^{(2)} + M_{33}a_3^{(2)}a_3^{(2)} \\
&\quad +2M_{12}a_2^{(2)}a_1^{(2)} + 2M_{13}a_3^{(2)}a_1^{(2)} + 2M_{23}a_3^{(2)}a_2^{(2)} \\
&= M_{11}\sin^2\psi + M_{22}\cos^2\psi - 2M_{12}\cos\psi\sin\psi
\end{aligned}$$

$$
\begin{aligned}
\rho B_{22}(\psi) &= \rho\left(M_{11}\sin^2\psi + M_{22}\cos^2\psi - 2M_{12}\cos\psi\sin\psi\right) \\
&= C_{11}\cos^2\psi\sin^2\psi + C_{66}\sin^4\psi + 2C_{16}\cos\psi\sin^3\psi \\
&+ C_{66}\cos^4\psi + C_{22}\cos^2\psi\sin^2\psi + 2C_{26}\cos^3\psi\sin\psi \\
&- 2C_{16}\cos^3\psi\sin\psi - 2C_{26}\cos\psi\sin^3\psi - 2\left(C_{12}+C_{66}\right)\cos^2\psi\sin^2\psi \\
&= C_{66}\cos^4\psi + 2(-C_{16}+C_{26})\cos^3\psi\sin\psi + (C_{11}+C_{22}-2C_{12}-2C_{66})\cos^2\psi\sin^2\psi \\
&\quad +2(C_{16}-C_{26})\cos\psi\sin^3\psi + C_{66}\sin^4\psi \\
&= \frac{1}{8}C_{66}\left(3+4\cos(2\psi)+\cos(4\psi)\right) + \frac{1}{4}(-C_{16}+C_{26})\left(2\sin 2\psi + \sin 4\psi\right) \\
&\quad +\frac{1}{8}(C_{11}+C_{22}-2\hat{C}_{12}-2C_{66})\left(1-\cos(4\psi)\right) + \frac{1}{4}(C_{16}-C_{26})\left(2\sin 2\psi - \sin 4\psi\right) \\
&\quad +\frac{1}{8}C_{66}\left(3-4\cos(2\psi)+\cos(4\psi)\right) - \mu \\
&= A_0 + A_{2c}\cos(2\psi) + A_{2s}\sin(2\psi) + A_{4c}\cos(4\psi) + A_{4s}\sin(4\psi) \qquad \text{(S7)}
\end{aligned}
$$

$$A_0 = \frac{1}{8}\left(C_{11}+C_{22}-2C_{12}+4C_{66}\right) \equiv \mathcal{N} \qquad \text{(S8)}$$

$$A_{2c} = 0 \qquad \text{(S9)}$$

$$A_{2s} = 0 \qquad \text{(S10)}$$

$$A_{4c} = \frac{1}{8}(-C_{11}-C_{22}+2C_{12}+4C_{66}) = -E_c \qquad \text{(S11)}$$

$$A_{4s} = \frac{1}{2}(C_{26}-C_{16}) = E_s \qquad \text{(S12)}$$

where $\mathcal{N}$, E_c, and E_s are defined in Appendix B.

$\mathbf{B_{33}}$: $\hat{\mathbf{a}}^{(3)} = (0,0,1)^T$

$$
\begin{aligned}
B_{33}(\psi) = M_{jk}a_k^{(3)}a_j^{(3)} &= M_{11}a_1^{(3)}a_1^{(3)} + M_{22}a_2^{(3)}a_2^{(3)} + M_{33}a_3^{(3)}a_3^{(3)} \\
&\quad +2M_{12}a_2^{(3)}a_1^{(3)} + 2M_{13}a_3^{(3)}a_1^{(3)} + 2M_{23}a_3^{(3)}a_2^{(3)} \\
&= M_{33}
\end{aligned}
$$

$$
\begin{aligned}
\rho B_{33}(\psi) &= \rho M_{33} = C_{55}\cos^2\psi + C_{44}\sin^2\psi + 2C_{45}\cos\psi\sin\psi \\
&= \frac{1}{2}C_{55}(1+\cos(2\psi)) + \frac{1}{2}C_{44}(1-\cos(2\psi)) + C_{45}\sin(2\psi) \\
&= A_0 + A_{2c}\cos(2\psi) + A_{2s}\sin(2\psi) \qquad \text{(S13)}
\end{aligned}
$$

$$A_0 = \frac{1}{2}(C_{44}+C_{55}) \equiv \mathcal{L} \qquad \text{(S14)}$$

$$A_{2c} = \frac{1}{2}(C_{55}-C_{44}) \equiv G_c \qquad \text{(S15)}$$

$$A_{2s} = C_{45} \equiv -G_s \qquad \text{(S16)}$$

where $\mathcal{L}$, G_c, and G_s are defined in Appendix B.

$\mathbf{B_{23}}$: $\vec{\mathbf{a}}^{(2)} = (-\sin\psi, \cos\psi, 0)^T$, $\vec{\mathbf{a}}^{(3)} = (0, 0, 1)^T$

$$\begin{aligned} B_{23}(\psi) &= M_{jk}a_k^{(2)}a_j^{(3)} = M_{11}a_1^{(2)}a_1^{(3)} + M_{22}a_2^{(2)}a_2^{(3)} + M_{33}a_3^{(2)}a_3^{(3)} \\ &= M_{13}a_3^{(3)}a_1^{(2)} + M_{23}a_3^{(3)}a_2^{(2)} \\ &= -M_{13}\sin\psi + M_{23}\cos\psi \end{aligned}$$

$$\begin{aligned} \rho B_{23}(\psi) &= -\rho M_{13}\sin\psi + \rho M_{23}\cos\psi \\ &= \left[-C_{15}\cos^2\psi\sin\psi - C_{46}\sin^3\psi - (C_{14}+C_{56})\cos\psi\sin^2\psi\right] \\ &\quad + \left[C_{56}\cos^3\psi + C_{24}\cos\psi\sin^2\psi + (C_{25}+C_{46})\cos^2\psi\sin\psi\right] \\ &= C_{56}\cos^3\psi + (-C_{15}+C_{25}+C_{46})\cos^2\psi\sin\psi + (C_{24}-C_{14}-C_{56})\cos\psi\sin^2\psi \\ &\quad -C_{46}\sin^3\psi \\ &= A_{1c}\cos(\psi) + A_{1s}\sin(\psi) + A_{3c}\cos(3\psi) + A_{3s}\sin(3\psi) \end{aligned} \tag{S17}$$

$$A_{1c} = \frac{1}{4}(2C_{56} + C_{24} - C_{14}) \equiv -M_s \tag{S18}$$

$$A_{1s} = \frac{1}{4}(-C_{15} + C_{25} - 2C_{46}) \equiv -M_c \tag{S19}$$

$$A_{3c} = \frac{1}{4}(2C_{56} - C_{24} + C_{14}) \equiv D_s \tag{S20}$$

$$A_{3s} = \frac{1}{4}(-C_{15} + C_{25} + 2C_{46}) \equiv -D_c \tag{S21}$$

where M_c, M_s, D_c, and D_s are defined in Appendix B.

S.2 The B_{mn} Coefficients for a TTI Medium

Substitute the components of C_{mn}^{TTI} from Appendix A (equations (A.6) - (A.19)) into the definitions of the anisotropic parameters in Appendix B, to obtain:

$$2\mathcal{L} = E\sin^2\theta\cos^2\theta + N\sin^2\theta + L(1+\cos^2\theta) \tag{S22}$$

$$8\mathcal{N} = E\sin^4\theta + 8L\sin^2\theta + 8N\cos^2\theta \tag{S23}$$

$$8E_c = E\sin^4\theta \tag{S24}$$

$$2G_c = E\sin^2\theta\cos^2\theta + (L-N)\sin^2\theta \tag{S25}$$

$$4M_c = E\sin^3\theta\cos\theta + 4(L-N)\sin\theta\cos\theta \tag{S26}$$

$$4D_c = E\sin^3\theta\cos\theta \tag{S27}$$

where

$$E \equiv A + C - 2F - 4L \tag{S28}$$

and θ is the dip angle around the y-axis. In addition, for a TTI medium, $0 = G_s = E_s = M_s = D_s$.

Inserting equations (S22) - (S27) into equations (4.24)-(4.26) and equation (4.20), we get

$$\begin{aligned}
\rho(B_{22}+B_{33}) &= L+N+\sin^2\theta\cos^2\psi[E(\cos^2\theta+\sin^2\theta\sin^2\psi)+(L-N)] && \text{(S29)}\\
\rho(B_{22}-B_{33}) &= (\sin^2\theta\sin^2\psi-\cos^2\theta)[E\sin^2\theta\cos^2\psi+(L-N)] && \text{(S30)}\\
\rho B_{23} &= -\sin\theta\cos\theta\sin\psi[E\sin^2\theta\cos^2\psi+(L-N)] && \text{(S31)}\\
\rho B &= (\cos^2\theta+\sin^2\theta\sin^2\psi)[E\sin^2\theta\cos^2\psi+(L-N)] && \text{(S32)}
\end{aligned}$$

Note that in definition of equation (S32) there is a complication. At some azimuths quasi-S_1 may be faster than quasi-S_2 whereas at other azimuths it may be slower. To deal with this we remove the absolute value sign in the definition of B, i.e., we do not apply it, and then directly assign the minus sign to quasi-S_1 and the plus sign to quasi-S_2. Directly assigning a single sign without first removing the absolute value in B may be incorrect in some circumstances.

Inserting equations (S29) and (S32) into equation (4.19) and using the minus sign in (4.19) for the quasi-S_1 wave, we obtain

$$\begin{aligned}
\rho V_{qS_1}^2 &= \frac{\rho}{2}[B_{22}+B_{33}-B]\\
&= \frac{1}{2}[L+N+(\sin^2\theta\cos^2\psi-\cos^2\theta-\sin^2\theta\sin^2\psi)(L-N)]\\
&= \frac{1}{2}[L+N-\cos^2\theta(L-N)+\sin^2\theta(\cos^2\psi-\sin^2\psi)(L-N)]\\
&= \frac{1}{2}[L(1-\cos^2\theta)+N(1+\cos^2\theta)+\sin^2\theta\cos2\psi(L-N)] && \text{(S33)}
\end{aligned}$$

so we have

$$\rho V_{qS_1}^2 = C_0 + C_2\cos2\psi \tag{S34}$$

with

$$\begin{aligned}
C_0 &= \frac{1}{2}\left(L(1-\cos^2\theta)+N(1+\cos^2\theta)\right), && \text{(S35)}\\
C_2 &= \frac{1}{2}(L-N)\sin^2\theta && \text{(S36)}
\end{aligned}$$

The relative peak-to-peak amplitude of the 2ψ component of quasi-S_1 can be simplified further from equations (S35) and (S36). Temporarily define the small quantity $\epsilon \equiv (L-N)/(L+N)$, we find:

$$\frac{|C_2|}{C_0} = \frac{|L-N|\sin^2\theta}{(L+N)-(L-N)\cos^2\theta} \approx |\epsilon|\sin^2\theta(1+\epsilon\cos^2\theta) \approx \frac{|L-N|}{L+N}\sin^2\theta \tag{S37}$$

where we retain only first-order terms in ϵ.

For the quasi-S_2 wave, we use the plus sign in equation (4.19) to obtain

$$\begin{aligned}
\rho V_{qS_2}^2 &= \frac{\rho}{2}[B_{22} + B_{33} + B] \\
&= \frac{1}{2}[L + N + \sin^2\theta\cos^2\psi(\cos^2\theta + \sin^2\theta\sin^2\psi)E + \sin^2\theta\cos^2\psi(L - N) \\
&\quad + \sin^2\theta\cos^2\psi(\cos^2\theta + \sin^2\theta\sin^2\psi)E \\
&\quad + (\cos^2\theta + \sin^2\theta\sin^2\psi)(L - N)] \\
&= \frac{1}{2}[(L + N) + 2\sin^2\theta\cos^2\psi(\cos^2\theta + \sin^2\theta\sin^2\psi)E + (L - N)] \\
&= L + \sin^2\theta\cos^2\psi(\cos^2\theta + \sin^2\theta\sin^2\psi)E \\
&= L + \sin^2\theta\cos^2\theta\cos^2\psi E + \sin^4\theta\sin^2\psi\cos^2\psi E \\
&= L + \frac{1}{2}\sin^2\theta\cos^2\theta(1 + \cos 2\psi)E + \frac{1}{8}\sin^4\theta(1 - \cos 4\psi)E
\end{aligned} \tag{S38}$$

so we have

$$\rho V_{qS_2}^2 = B_0 + B_2\cos 2\psi + B_4\cos 4\psi, \tag{S39}$$

with

$$B_0 = L + \left(\frac{1}{2}\sin^2\theta\cos^2\theta + \frac{1}{8}\sin^4\theta\right)E \tag{S40}$$

$$B_2 = \frac{1}{2}\sin^2\theta\cos^2\theta E \tag{S41}$$

$$B_4 = -\frac{1}{8}\sin^4\theta E \tag{S42}$$

S.3 Eigenvectors for General Anisotropic and TTI Media

Specification of the eigenvectors requires knowledge of the polarization angle Φ. For example, the eigenvector $\tilde{\mathbf{a}}^{(2)}$ (equation (3.20)) satisfies (equation (4.17))

$$(B_{22} - V_2^2)\cos\Phi + B_{23}\sin\Phi = 0 \tag{S43}$$

Solving for $\tan\Phi$ and using equation (4.19), we have

$$\tan\Phi = \frac{V^2 - B_{22}}{B_{23}} = \frac{B_{33} - B_{22} \pm B}{2B_{23}} \tag{S44}$$

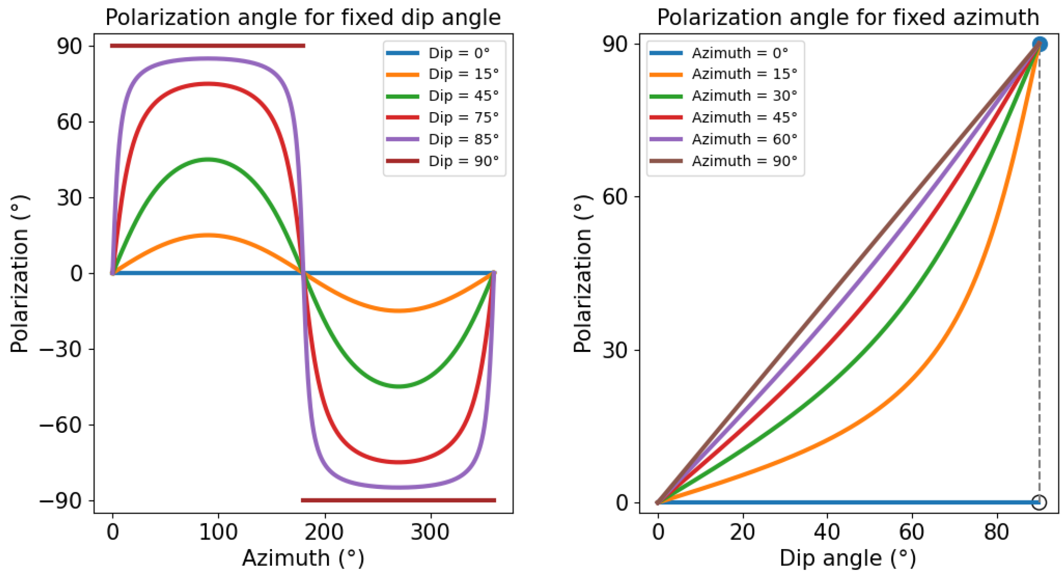

Figure S1. Polarization angle Φ of the eigenvectors presented as a function of azimuth of propagation ψ and dip angle θ using the transversely isotropic elastic tensor in **Table 1**, sample index #20 from the compilation of Brownlee *et al*. (2017).

Simplifying, we have

$$\begin{aligned}
\tan 2\Phi &= \frac{2\tan\Phi}{1-\tan^2\Phi} && \text{(S45)}\\
&= \frac{B_{33}-B_{22}\pm B_{22}}{B_{23}} \Big/ \left[1-\left(\frac{B_{33}-B_{22}\pm B}{2B_{23}}\right)^2\right] && \text{(S46)}\\
&= \frac{B_{33}-B_{22}\pm B_{22}}{B_{23}} \Big/ \left[\frac{4B_{23}^2}{4B_{23}^2}-\left(\frac{B_{33}-B_{22}\pm B}{2B_{23}}\right)^2\right] && \text{(S47)}\\
&= \frac{4B_{23}\left[(B_{33}-B_{22})\pm B_{22}\right]}{4B_{23}^2-(B_{33}-B_{22}\pm B)^2} && \text{(S48)}\\
&= \frac{4B_{23}\left[(B_{33}-B_{22})\pm B_{22}\right]}{[B^2-(B_{33}-B_{22})^2]-[(B_{33}-B_{22})^2\pm 2B(B_{33}-B_{22})+B^2]} && \text{(S49)}\\
&= \frac{4B_{23}\left[(B_{33}-B_{22})\pm B_{22}\right]}{-2(B_{33}-B_{22})^2\pm 2B(B_{33}-B_{22})} && \text{(S50)}\\
&= \frac{4B_{23}[(B_{33}-B_{22})\pm B]}{-2(B_{33}-B_{22})[(B_{33}-B_{22})\pm B]} = \frac{2B_{23}}{B_{22}-B_{33}} && \text{(S51)}
\end{aligned}$$

where in obtaining equation (S49) we used equation (4.20).

For a TTI medium, inserting equation (S30)-(S32) into equation (S44), we obtain Φ for the quasi-

S_1 wave by using the minus sign in equation (S44):

$$\tan\Phi = \frac{B_{33} - B_{22} - B}{2B_{23}} \tag{S52}$$

$$= \frac{\cos^2\theta - \sin^2\theta\sin^2\psi - (\cos^2\theta + \sin^2\theta\sin^2\psi)}{-2\sin\theta\cos\theta\sin\psi} \tag{S53}$$

$$= \tan\theta\sin\psi \tag{S54}$$

S.4 Ellipticity Parameter η_X

Historically, there have been a number of attempts to describe the shape of the slowness surface for $_qP$, $_qSV$, and $_qSH$ waves with a single parameter when anisotropy deviates from elliptical. The "shape factor" $\eta = F/(A-2L)$ has been used, but its definition is not physically motivated, it is very difficult to measure in the laboratory, and it can lead to aberrant behavior when it is varied independently from the other moduli. Formally, the condition for elliptical anisotropy in which the $_qSV$ phase surface will be circular and the $_qP$ and $_qSH$ phase surfaces will be elliptical is the following (Thomsen 1986):

$$(C_{13} + C_{44})^2 = (C_{11} - C_{44})(C_{33} - C_{44}) \tag{S55}$$

Notice that the $_qSH$ phase speed surface will be spherical because Thomsen (1986) is considering body waves propagating in the vertical plane. For a VTI medium (equation (A.4)) this reduces to

$$(F + L)^2 = (A - L)(C - L) \tag{S56}$$

Kawakatsu (2016) used this to define a physically motivated ellipticity parameter, η_K, by taking the square root of both sides

$$\eta_K \equiv \frac{F + L}{\sqrt{(C - L)(A - L)}} \tag{S57}$$

For weak anisotropy, it is useful to simplify by retaining only first-order perturbations. Let the moduli A, C, N, L and F deviate from isotropic moduli as follows

$$A = \lambda + 2\mu + \delta A \tag{S58}$$

$$C = \lambda + 2\mu + \delta C \tag{S59}$$

$$L = \mu + \delta L \tag{S60}$$

$$N = \mu + \delta N \tag{S61}$$

$$F = \lambda + \delta F \tag{S62}$$

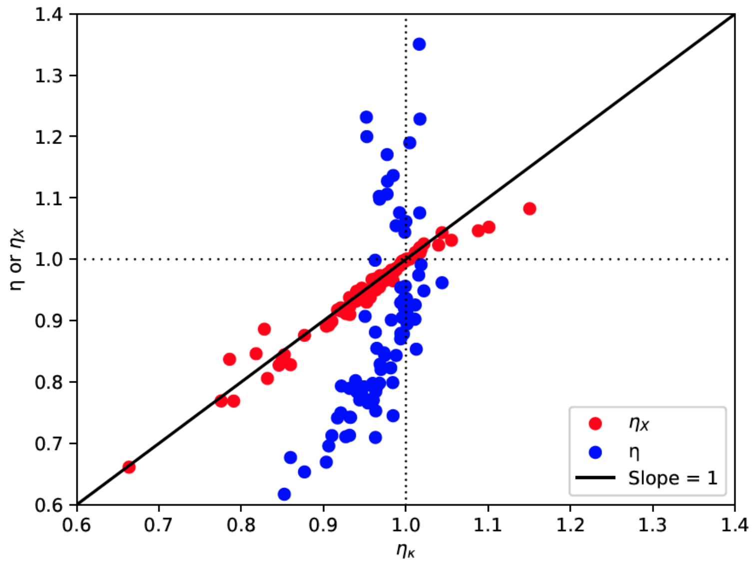

Figure S2. Comparison of η_X and η to η_K for all of the samples in the database of elastic tensors of Brownlee *et al*. (2017).

and substitute them into equation (S56):

$$(\lambda + \delta F + \mu + \delta L)^2 = (\lambda + 2\mu + \delta A - \mu - \delta L)(\lambda + 2\mu + \delta C - \mu - \delta L) \tag{S63}$$

$$((\lambda + \mu) + (\delta F + \delta L))^2 = ((\lambda + \mu) + (\delta A - \delta L))((\lambda + \mu) + (\delta C - \delta L)) \tag{S64}$$

$$(\lambda + \mu)^2 + 2(\lambda + \mu)(\delta F + \delta L) \approx (\lambda + \mu)^2 + (\lambda + \mu)(\delta A + \delta C - 2\delta L) \tag{S65}$$

$$2\delta F + 4\delta L \approx \delta A + \delta C \tag{S66}$$

$$2F + 4L \approx A + C \tag{S67}$$

where the third equality is approximate because we dropped second order terms (e.g. where perturbed quantities are multiplied by one another) and to get the last equality we added $2(\lambda + 2\mu)$ to both sides of the previous equation.

Equation (S67) defines an ellipticity parameter consistent with weak anisotropy. Rewriting it as $4L = A + C - 2F$, we define the weak anisotropy ellipticity parameter as

$$\eta_X \equiv \frac{4L}{A + C - 2F} \tag{S68}$$

which is approximately equal to η_K, as **Figure S2** shows, but allows simple expressions for the azimuthal variation of phase speed in terms of it, as follows.

We approximate the isotropic velocity of the quasi-S_2 wave (equation (S40)) as follows

$$B_0 \approx B_0^{HTI} = \frac{1}{8}(A + C - 2F)(1 + \eta_X) \tag{S69}$$

which introduces a second-order error compared to the variation in anisotropy. For anisotropy of the quasi-S_2 wave, we find that

$$B_2 = \frac{1}{2}(A+C-2F)(1-\eta_X)\sin^2\theta\cos^2\theta \tag{S70}$$

$$B_4 = -\frac{1}{8}(A+C-2F)(1-\eta_X)\sin^4\theta \tag{S71}$$

So the peak-to-peak amplitude of 2-ψ and 4-ψ anisotropy is

$$A_2 = \frac{|B_2|}{B_0} \approx \frac{4|1-\eta_X|\sin^2\theta\cos^2\theta}{1+\eta_X} \approx 2|1-\eta_X|\sin^2\theta\cos^2\theta \tag{S72}$$

$$A_4 = \frac{|B_4|}{B_0} \approx \frac{|1-\eta_X|\sin^4\theta}{1+\eta_X} \approx \frac{1}{2}|1-\eta_X|\sin^4\theta \tag{S73}$$

S.5 Hamilton's Principle for Body and Surface Waves

S.5.1 Body waves

In an elastic medium, the action for seismic waves is

$$I = \int_{t_1}^{t_2}\int L(\dot{\mathbf{u}}, \nabla\mathbf{u})dV\,dt \tag{S74}$$

where L is the Lagrangian density, given by the difference between the kinetic energy and elastic strain energy (in index notation)

$$L = T - V = \frac{1}{2}\rho\dot{u}_i\dot{u}_i^* - \frac{1}{2}c_{ijk\ell}\epsilon_{ij}\epsilon_{kl}^* \tag{S75}$$

where u_i is the displacement (which we use rather than $\tilde{u}_i$), $c_{ijk\ell}$ is the fourth-order elastic tensor, ϵ_{ij} is the strain tensor, and $*$ denotes complex conjugation. Hamilton's principle states that the action is stationary with respect to small perturbations to vector displacement $\mathbf{u}$, where $\delta\mathbf{u} = 0$ at $t = t_1, t = t_2$ and at the surface (Dahlen & Tromp 2020). This gives Lagrange's equation for a continuum

$$\frac{d}{dt}\frac{\partial L}{\partial \dot{u}_i} + \partial_j\frac{\partial L}{\partial u_{i,j}} = 0 \tag{S76}$$

where we have applied $\partial L/\partial u_i = 0$ because the Lagrangian density is independent of displacement.

$$u_i = \tilde{a}_i f = \alpha_m \hat{a}_i^{(m)} f \tag{S77}$$

where α_m is the coupling (expansion) coefficient, summation is over the repeated index m ranging from 2 to 3, $\tilde{a}_i$ is the i-th component of the perturbed polarization vector $\tilde{\mathbf{a}}$, $\hat{a}_i^{(m)}$ is the i-th component of basis vector $\hat{\mathbf{a}}^{(m)}$, and f is the propagation term. Then we have the following equalities (with index summation over q ranging from 1 to 2)

$$\begin{aligned}
\frac{d}{dt}\frac{\partial L}{\partial \dot{u}_i} &= \frac{\partial L}{\partial \dot{u}_i}(\partial_t f^*)f = -\frac{\partial L}{\partial \dot{u}_i}(\partial_t f)f^* && \text{(S78)}\\
\partial_q \frac{\partial L}{\partial u_{i,q}} &= \frac{\partial L}{\partial u_{i,q}}(\partial_q f^*)f = -\frac{\partial L}{\partial u_{i,q}}(\partial_q f)f^* && \text{(S79)}\\
\partial_q (f\hat{a}_i{}^{(m)}\frac{\partial L}{\partial u_{i,q}}) &= \hat{a}_i{}^{(m)}\partial_q\left(f\frac{\partial L}{\partial u_{i,q}}\right) = \hat{a}_i{}^{(m)}\left(\frac{\partial L}{\partial u_{i,q}}\right)\partial_q f + \hat{a}_i{}^{(m)} f\partial_q \frac{\partial L}{\partial u_{i,q}} && \text{(S80)}\\
&= \hat{a}_i{}^{(m)}\left[\left(\frac{\partial L}{\partial u_{i,q}}\right)\partial_q f - f\frac{\partial L}{\partial u_{i,q}}(\partial_q f)f^*\right] = 0
\end{aligned}$$

From equations (S76) and (S78), we can rewrite Lagrange's equation as

$$-\frac{\partial L}{\partial \dot{u}_i}(\partial_t f) + f\partial_j \frac{\partial L}{\partial u_{i,j}} = 0 \tag{S81}$$

Based on the chain role for partial derivatives, we have the following equation for the coupling coeff- cients α_m (eqn (S75)):

$$\frac{\partial L}{\partial \alpha_m} = \frac{\partial L}{\partial u_i}\frac{\partial u_i}{\partial \alpha_m} + \frac{\partial L}{\partial \dot{u}_i}\frac{\partial \dot{u}_i}{\partial \alpha_m} + \frac{\partial L}{\partial u_{i,j}}\frac{\partial u_{i,j}}{\partial \alpha_m} \tag{S82}$$

Based on equation (S75), we have

$$\begin{aligned}
\frac{\partial L}{\partial u_i} &= 0 && \text{(S83)}\\
\frac{\partial \dot{u}_i}{\partial \alpha_m} &= \frac{\partial[\alpha_m \hat{a}_i^{(m)}\partial_t f]}{\partial \alpha_m} = \hat{a}_i^{(m)}\partial_t f && \text{(S84)}\\
\frac{\partial u_{i,j}}{\partial \alpha_m} &= \frac{\partial[\alpha_m \partial_j(\hat{a}_i^{(m)} f)]}{\partial \alpha_m} = \partial_j(\hat{a}_i^{(m)} f) && \text{(S85)}
\end{aligned}$$

Inserting equations (S83)-(S85) into equation (S81) and based on equations (S80) and (S81), we obtain

$$\begin{aligned}
\frac{\partial L}{\partial \alpha_m} &= \frac{\partial L}{\partial \dot{u}_i}\left(\hat{a}_i^{(m)}\partial_t f) + \frac{\partial L}{\partial u_{i,j}}\partial_j(\hat{a}_i^{(m)} f\right) = \hat{a}_i^{(m)} f\partial_j \frac{\partial L}{\partial u_{i,j}} + \frac{\partial L}{\partial u_{i,j}}\partial_j(\hat{a}_i^{(m)} f) && \text{(S86)}\\
&= \partial_j\left(f\hat{a}_i^{(m)}\frac{\partial L}{\partial u_{i,j}}) = \partial_3(f\hat{a}_i^{(m)}\frac{\partial L}{\partial u_{i,3}}\right)
\end{aligned}$$

From the index notation of equation (S77), we can rewrite equation (S75) as

$$L_{BW} = \frac{1}{2}\rho\omega^2\alpha_m\alpha_m^* - \frac{1}{2}\rho k^2\alpha_m\alpha_n^* B_{mn} \tag{S87}$$

Finally, assuming the body wave polarization vector is not a function of depth, we have the eigenvalue problem for body waves from Hamilton's principle

$$\frac{\partial L_{BW}}{\partial \alpha_m} = 0 \tag{S88}$$

S.5.2 Surface waves

The derivation of Hamilton's Principle for surface waves is slightly different from body waves since the polarization vector is a function of depth. For surface waves, we first integrate equation (S86)over depth, to obtain

$$\begin{aligned}\int_0^\infty \frac{\partial L}{\partial \alpha_m} dz &= \frac{\partial[\int_0^\infty L dz]}{\partial \alpha_m} = \int_0^\infty \partial_3 \left(f \hat{a}_i^{(m)} \frac{\partial L}{\partial u_{i,3}} \right) dz \\ &= f \hat{a}_i^{(m)} \frac{\partial L}{\partial u_{i,3}} \Big|_0^\infty = 0\end{aligned} \tag{S89}$$

The last equation in equation (S89) results from the boundary conditions (Aki & Richards 2002).

$$\hat{a}_i^{(m)}(z) = 0, z \to \infty \tag{S90}$$

$$\frac{\partial L}{\partial u_{i,3}} \approx \tau_{i3} = 0, z = 0 \tag{S91}$$

where τ_{i3} is the component of stress tensor in the third column. So for surface wave, we define the Lagrangian density as

$$L_{SW} = T - V = \int_0^\infty \frac{1}{2} \rho \dot{u}_i \dot{u}_i^* dz - \int_0^\infty \frac{1}{2} C_{ijkl} \epsilon_{ij} \epsilon_{kl}^* dz \tag{S92}$$

and for the coupling problem in surface waves, we also have

$$\frac{\partial L_{SW}}{\partial \alpha_m} = 0 \tag{S93}$$

S.6 Surface waves

The Lagrangian density L is defined as

$$L = T - V = \frac{1}{2} \omega^2 \int_0^\infty \rho u_i u_i^* dz - \frac{1}{2} \int_0^\infty c_{ijkl} \epsilon_{ij} \epsilon_{kl}^* dz \tag{S94}$$

where * denontes complex conjugation, $\epsilon_{ij} = (u_{i,j} + u_{j,i})/2$ is the strain tensor, T is the kinetic energy per unit area, V is the potential energy per unit area, and the summation convention is assumed.

Before computing L, we introduce the following notational simplification to equation (3.8) for displacement:

$$\vec{\mathbf{u}}(\vec{\mathbf{r}}, z, t) = \hat{\mathbf{s}}(z) f(\vec{\mathbf{r}}, t) \tag{S95}$$

where $\hat{\mathbf{s}}(z)$ is the vector displacement eigenfunction

$$\hat{\mathbf{s}}(z) = (\alpha a_R V(z) - \beta a_L W(z), \beta a_R V(z) + \alpha a_L W(z), i a_R U(z))^T \tag{S96}$$

and f is defined in equation (3.4) and we introduced $\alpha \equiv \cos \psi$ and $\beta \equiv \sin \psi$.

For the kinetic energy, from equations (S96), we have

$$\begin{aligned}
T &= \frac{1}{2}\omega^2 \int_0^\infty \rho u_i u_i^* dz = \frac{1}{2}w^2 \int_0^\infty \rho(|-\beta a_L W + \alpha a_R V|^2 + |\alpha a_L W + \beta a_R V|^2 + |i a_R U|^2) dz \\
&= \frac{1}{2}\omega^2 \int_0^\infty \rho[(-\beta a_L W + \alpha a_R V) * (-\beta a_L^* W + \alpha a_R^* V) \\
&+ (\alpha a_L W + \beta a_R V) * (\alpha a_L^* W + \beta a_R^* V) + a_R a_R^* U^2] dz \\
&= \frac{1}{2}\omega^2 \int_0^\infty \rho \left(a_L a_L^* W^2 + a_R a_R^* (U^2 + V^2) \right) dz \\
&= \frac{1}{2}\omega^2 \left(a_L a_L^* + a_R a_R^* \right) \qquad \text{(S97)}
\end{aligned}$$

where in the final step we used $\alpha^2 + \beta^2 = 1$. The coupling coefficients a_L and a_R are complex numbers, while Tanimoto (2004) implicitly assumed they are real, which inaccurately represents the coupling strength between Rayleigh wave and Love wave.

The potential energy is

$$V = \frac{1}{2} \int_0^\infty c_{ijkl} \epsilon_{ij} \epsilon_{kl}^* dz \qquad \text{(S98)}$$

Computing the strain tensor ϵ_{ij} requires the following spatial derivatives

$$\begin{aligned}
u_{1,1} &= ik\alpha(-\beta a_L W + \alpha a_R V) f && \text{(S99)} \\
u_{1,2} &= ik\beta(-\beta a_L W + \alpha a_R V) f && \text{(S100)} \\
u_{1,3} &= (-\beta a_L W' + \alpha a_R V') f && \text{(S101)} \\
u_{2,1} &= ik\alpha(\alpha a_L W + \beta a_R V) f && \text{(S102)} \\
u_{2,2} &= ik\beta(\alpha a_L W + \beta a_R V) f && \text{(S103)} \\
u_{2,3} &= (\alpha a_L W' + \beta a_R V') f && \text{(S104)} \\
u_{3,1} &= -k\alpha a_R U f && \text{(S105)} \\
u_{3,2} &= -k\beta a_R U f && \text{(S106)} \\
u_{3,3} &= i a_R U' f && \text{(S107)}
\end{aligned}$$

Based on eq. S99 - S107, the strain tensor is

$$\begin{aligned}
\epsilon_{11} &= ik(-\alpha\beta a_L W + \alpha^2 a_R V) f && \text{(S108)} \\
\epsilon_{12} &= \frac{i}{2} k(-\beta^2 a_L W + 2\alpha\beta a_R V + \alpha^2 a_L W) f && \text{(S109)} \\
\epsilon_{13} &= \frac{1}{2}(-\beta a_L W' + \alpha a_R V' - k\alpha a_R U) f && \text{(S110)} \\
\epsilon_{22} &= ik(\alpha\beta a_L W + \beta^2 a_R V) f && \text{(S111)} \\
\epsilon_{23} &= \frac{1}{2}(\alpha a_L W' + \beta a_R V' - k\beta a_R U) f && \text{(S112)} \\
\epsilon_{33} &= i a_R U' f && \text{(S113)}
\end{aligned}$$

There are 21 elastic constants for a general anisotropic medium, therefore there are 21 components in potential energy (eqn (S98)). Using the abbreviated or Voigt notation, these are

$$C_{11}\epsilon_{11}\epsilon_{11}^* = C_{11}k^2[\alpha^2\beta^2 a_L a_L^* W^2 - (a_L a_R^* + a_L^* a_R)\alpha^3\beta WV + \alpha^4 a_R a_R^* V^2] \tag{S114}$$

$$2C_{16}\epsilon_{11}\epsilon_{12}^* + 2C_{16}\epsilon_{12}\epsilon_{11}^* = C_{16}k^2[4\alpha^3\beta a_R a_R^* V^2 - 2\alpha\beta(\alpha^2-\beta^2)a_L a_L^* W^2 + (a_L^* a_R + a_L a_R^*)(\alpha^4 - 3\alpha^2\beta^2)WV] \tag{S115}$$

$$2C_{15}\epsilon_{11}\epsilon_{13}^* + 2C_{15}\epsilon_{13}\epsilon_{11}^* = C_{15}ik\alpha^2\beta(a_L a_R^* - a_L^* a_R)(VW' - WV' + kWU) \tag{S116}$$

$$C_{12}\epsilon_{11}\epsilon_{22}^* + C_{12}\epsilon_{22}\epsilon_{11}^* = C_{12}k^2[2\alpha^2\beta^2 a_R a_R^* V^2 - 2\alpha^2\beta^2 a_L a_L^* W^2 + (a_L^* a_R + a_L a_R^*)(\alpha^3\beta - \alpha\beta^3)WV] \tag{S117}$$

$$2C_{14}\epsilon_{11}\epsilon_{23}^* + 2C_{14}\epsilon_{23}\epsilon_{11}^* = -C_{14}ik(a_L a_R^* - a_L^* a_R)(\alpha^3 VW' + \alpha\beta^2 WV' - k\alpha\beta^2 WU) \tag{S118}$$

$$C_{13}\epsilon_{11}\epsilon_{33}^* + C_{13}\epsilon_{33}\epsilon_{11}^* = C_{13}k[2\alpha^2 a_R a_R^* VU' - \alpha\beta(a_L a_R^* + a_L^* a_R)WU'] \tag{S119}$$

$$C_{22}\epsilon_{22}\epsilon_{22}^* = C_{22}k^2[\alpha^2\beta^2 a_L a_L^* W^2 + \beta^4 a_R a_R^* V^2 + \alpha\beta^3(a_L a_R^* + a_L^* a_R)WV] \tag{S120}$$

$$C_{23}\epsilon_{22}\epsilon_{33}^* + C_{23}\epsilon_{33}\epsilon_{22}^* = C_{23}k[\alpha\beta(a_L a_R^* + a_L^* a_R)WU' + 2\beta^2 a_R a_R^* VU'] \tag{S121}$$

$$2C_{24}\epsilon_{22}\epsilon_{23}^* + 2C_{24}\epsilon_{23}\epsilon_{22}^* = -C_{24}ik\alpha\beta^2(a_L a_R^* - a_L^* a_R)(VW' - WV' + kWU) \tag{S122}$$

$$2C_{26}\epsilon_{22}\epsilon_{12}^* + 2C_{26}\epsilon_{12}\epsilon_{22}^* = C_{26}k^2[4\alpha\beta^3 a_R a_R^* V^2 + 2\alpha\beta(\alpha^2-\beta^2)a_L a_L^* W^2 + (3\alpha^2\beta^2 - \beta^4)(a_L a_R^* + a_L^* a_R)WV] \tag{S123}$$

$$2C_{25}\epsilon_{22}\epsilon_{13}^* + 2C_{25}\epsilon_{13}\epsilon_{22}^* = C_{25}ik(a_L a_R^* - a_L^* a_R)(\alpha^2\beta WV' + \beta^3 VW' - k\alpha^2\beta WU) \tag{S124}$$

$$C_{33}\epsilon_{33}\epsilon_{33} = C_{33}a_R a_R^* U'^2 \tag{S125}$$

$$2C_{34}\epsilon_{33}\epsilon_{23}^* + 2C_{34}\epsilon_{23}\epsilon_{33}^* = -C_{34}i\alpha(a_L a_R^* - a_L^* a_R)W'U' \tag{S126}$$

$$2C_{35}\epsilon_{33}\epsilon_{13}^* + 2C_{35}\epsilon_{13}\epsilon_{33}^* = C_{35}i\beta(a_L a_R^* - a_L^* a_R)W'U' \tag{S127}$$

$$2C_{36}\epsilon_{33}\epsilon_{12}^* + 2C_{36}\epsilon_{12}\epsilon_{33}^* = C_{36}k[(\alpha^2-\beta^2)(a_L a_R^* + a_L^* a_R)WU' + 4\alpha\beta a_R a_R^* VU'] \tag{S128}$$

$$4C_{44}\epsilon_{23}\epsilon_{23}^* = C_{44}[\alpha^2 a_L a_L^* W'^2 + \beta^2 a_R a_R^*(kU - V')^2 - \alpha\beta(a_L a_R^* + a_L^* a_R)(kU - V')W'] \tag{S129}$$

$$4C_{45}\epsilon_{23}\epsilon_{13}^* + 4C_{45}\epsilon_{13}\epsilon_{23}^* = C_{45}[-2\alpha\beta a_L a_L^* W'^2 + 2\alpha\beta a_R a_R^*(kU - V')^2 + (\beta^2 - \alpha^2)(a_L a_R^* + a_L^* a_R)(kU - V')W' \tag{S130}$$

$$4C_{46}\epsilon_{23}\epsilon_{12}^* + 4C_{46}\epsilon_{12}\epsilon_{23}^* = C_{46}ik(a_L a_R^* - a_L^* a_R)[\beta(\alpha^2-\beta^2)WV' - k\beta(\alpha^2-\beta^2)WU - 2\alpha^2\beta W'V] \tag{S131}$$

$$4C_{55}\epsilon_{13}\epsilon_{13}^* = C_{55}[\beta^2 a_L a_L^* W'^2 + \alpha^2 a_R a_R^*(kU - V')^2 + \alpha\beta(a_L a_R^* + a_L^* a_R)(kU - V')W'] \tag{S132}$$

$$4C_{56}\epsilon_{13}\epsilon_{12}^* + 4C_{56}\epsilon_{12}\epsilon_{13}^* = C_{56}ik(a_L a_R^* - a_L^* a_R)[\alpha(\alpha^2-\beta^2)WV' + 2\alpha\beta^2 W'V - k\alpha(\alpha^2-\beta^2)WU] \tag{S133}$$

$$4C_{66}\epsilon_{12}\epsilon_{12}^* = C_{66}k^2[(\alpha^2-\beta^2)a_L a_L^* W^2 + 2\alpha\beta(\alpha^2-\beta^2)(a_L a_R^* + a_L^* a_R)WV + 4\alpha^2\beta^2 a_R a_R^* V^2] \tag{S134}$$

where we used $ff^* = 1$. The terms colored with blue are the weak coupling between Rayleigh wave and Love wave, proposed by Tanimoto (2004), while the terms colored with red are the strong coupling proposed by us, summarized in (**Table A1**).

Tanimoto (2004) implicitly assumed that a_L and a_R are real, which will cause $a_L a_R^* - a_L^* a_R = 0$,

Table A1. Rayleigh-Love coupling terms.

Rayleigh wave	Love wave	Weak Rayleigh-Love coupling	Strong Rayleigh-Love coupling
$a_R a_R^*$	$a_L a_L^*$	$a_L a_R^* + a_L^* a_R$	$\mathrm{i}(a_L a_R^* - a_L^* a_R)$

resulting in no strong coupling between Rayleigh and Love waves. As a result, the phase speeds of his results are nearly the same as those of Smith & Dahlen (1973) and Montagner & Nataf (1986).

Summing equations (S114)-(S134) and rearanging by eigenfunctions and types (as in **Table A1**), we have the following 12 integral kernels

$$K_1 = (\mathcal{A} + B_c \cos 2\psi - B_s \sin 2\psi + E_c \cos 4\psi - E_s \sin 4\psi) a_R a_R^* k^2 V^2 \tag{S135}$$

$$K_2 = (\mathcal{L} + G_c \cos 2\psi - G_s \sin 2\psi) a_R a_R^* k^2 (U - \frac{V'}{k})^2 \tag{S136}$$

$$K_3 = 2(\mathcal{F} + H_c \cos 2\psi - H_s \sin 2\psi) a_R a_R^* k U' V \tag{S137}$$

$$K_4 = \mathcal{C} a_R a_R^* U'^2 \tag{S138}$$

$$K_5 = (\mathcal{N} - E_c \cos 4\psi + E_s \sin 4\psi) a_L a_L^* k^2 W^2 \tag{S139}$$

$$K_6 = (\mathcal{L} - G_c \cos 2\psi + G_s \sin 2\psi) a_L a_L^* W'^2 \tag{S140}$$

$$K_7 = (-\frac{1}{2} B_c \sin 2\psi - \frac{1}{2} B_s \cos 2\psi - E_c \sin 4\psi - E_s \cos 4\psi)(a_L a_R^* + a_L^* a_R) k^2 W V \tag{S141}$$

$$K_8 = (G_c \sin 2\psi + G_s \cos 2\psi)(a_L a_R^* + a_L^* a_R) k (U - \frac{V'}{k}) W' \tag{S142}$$

$$K_9 = (-H_c \sin 2\psi - H_s \cos 2\psi)(a_L a_R^* + a_L^* a_R) k W U' \tag{S143}$$

$$K_{10} = [2(J_c - M_c) \sin \psi - 2(J_s + M_s) \cos \psi + D_c \sin 3\psi - D_s \cos 3\psi] i (a_L a_R^* - a_L^* a_R) k W' V \tag{S144}$$

$$K_{11} = (M_c \sin \psi + M_s \cos \psi + D_c \sin 3\psi - D_s \cos 3\psi) i (a_L a_R^* - a_L^* a_R) k^2 W (U - \frac{V'}{k}) \tag{S145}$$

$$K_{12} = 2[(J_c - K_c) \sin \psi - (J_s - K_s) \cos \psi] i (a_L a_R^* - a_L^* a_R) W' U' \tag{S146}$$

where the anisotropy parameters are given in appendix B. So the potential energy is (equations (S98), (S135)-(S146)):

$$V = \frac{1}{2} \int_0^\infty (K_1 + K_2 + K_3 + K_4 + K_5 + K_6 + K_7 + K_8 + K_9 + K_{10} + K_{11} + K_{12})\, dz \tag{S147}$$

Now, combine the kernels such that A is for Love waves, B for Rayleigh waves, E for weak Rayleigh-Love coupling arising from the real part of the coupling coeffcients, and X is for strong Rayleigh-Love coupling arising from the imaginary part of the coeffcients. We have, therefore:

$$V = \frac{1}{2}[A a_L a_L^* + B a_R a_R^* + E(a_L a_R^* + a_L^* a_R) + iX(a_L a_R^* - a_L^* a_R)] \tag{S148}$$

where A, B, E, and X are

$$
\begin{aligned}
A =& k^2 \int_0^\infty dz[(\mathcal{N} - E_c \cos 4\psi + E_s \sin 4\psi)W^2 \\
&+ (\mathcal{L} - G_c \cos 2\psi + G_s \sin 2\psi)W'^2/k^2]
\end{aligned}
\tag{S149}
$$

$$
\begin{aligned}
B =& k^2 \int_0^\infty dz[(\mathcal{A} + B_c \cos 2\psi - B_s \sin 2\psi + E_c \cos 4\psi - E_s \sin 4\psi)V^2 \\
&+ (\mathcal{L} + G_c \cos 2\psi - G_s \sin 2\psi)(U - \frac{V'}{k})^2 \\
&+ 2(\mathcal{F} + H_c \cos 2\psi - H_s \sin 2\psi)VU'/k \\
&+ CU'^2/k^2]
\end{aligned}
\tag{S150}
$$

$$
\begin{aligned}
E =& k^2 \int_0^\infty dz[(-\frac{1}{2}B_c \sin 2\psi - \frac{1}{2}B_s \cos 2\psi - E_c \sin 4\psi - E_s \cos 4\psi)WV \\
&+ (G_c \sin 2\psi + G_s \cos 2\psi)(U - \frac{V'}{k})W'/k \\
&+ (-H_c \sin 2\psi - H_s \cos 2\psi)WU'/k]
\end{aligned}
\tag{S151}
$$

$$
\begin{aligned}
X =& k^2 \int_0^\infty dz[[2(J_c - M_c)\sin\psi - 2(J_s + M_s)\cos\psi + D_c \sin 3\psi - D_s \cos 3\psi]VW'/k \\
&+ (M_c \sin\psi + M_s \cos\psi + D_c \sin 3\psi - D_s \cos 3\psi)W(U - \frac{V'}{k}) \\
&+ 2[(J_c - K_c)\sin\psi - (J_s - K_s)\cos\psi]W'U'/k^2]
\end{aligned}
\tag{S152}
$$

Hamilton's principle states that the Lagrangian is stationary with respect to first-order perturbations of the eigenfunctions, namely a_L and a_R in this case. Therefore,

$$
\frac{\partial L}{\partial a_L} = 0, \tag{S153}
$$

$$
\frac{\partial L}{\partial a_R} = 0. \tag{S154}
$$

Using the following quantities are needed in the derivation

$$\frac{\partial a_L a_L^*}{\partial a_L} = a_L^* \quad \text{(S155)}$$
$$\frac{\partial a_L a_L^*}{\partial a_R} = 0 \quad \text{(S156)}$$
$$\frac{\partial a_R a_R^*}{\partial a_L} = 0 \quad \text{(S157)}$$
$$\frac{\partial a_R a_R^*}{\partial a_R} = a_R^* \quad \text{(S158)}$$
$$\frac{\partial a_L a_R^*}{\partial a_L} = a_R^* \quad \text{(S159)}$$
$$\frac{\partial a_L a_R^*}{\partial a_R} = 0 \quad \text{(S160)}$$
$$\frac{\partial a_L^* a_R}{\partial a_L} = 0 \quad \text{(S161)}$$
$$\frac{\partial a_L^* a_R}{\partial a_R} = a_L^* \quad \text{(S162)}$$

From equations (S94,) (S97), (S148), (S153), and (S155) - (S162), we have

$$0 = \frac{\partial L}{\partial a_L} = \frac{1}{2} a_L^* \omega^2 \int_0^\infty \rho W^2 dz - \frac{1}{2}[A a_L^* + (E + iX) a_R^*] = 0 \quad \text{(S163)}$$

Applying the normalization of the Love wave eigenfunction (eqn (3.8)), this reduces to

$$A a_L^* + (E + iX) a_R^* = \omega^2 a_L^* \quad \text{(S164)}$$

Similarly, from equations (S94), (S97), (S148), (S154), and (S155) - (S162), we obtain

$$0 = \frac{\partial L}{\partial a_R} = \frac{1}{2} a_R^* \omega^2 \int_0^\infty \rho (U^2 + V^2) dz - \frac{1}{2}[(E - iX) a_L^* + B a_R^*] \quad \text{(S165)}$$

From the normalization of Rayleigh wave eigenfunctions (eqn (3.5)), this simplifies to

$$(E - iX) a_L^* + B a_R^* = \omega^2 a_R^* \quad \text{(S166)}$$

Equations (S164) and (S169) combine to produce an eigenvalue-eigenvector problem that governs Rayleigh-Love coupling:

$$\begin{pmatrix} A & E + iX \\ E - iX & B \end{pmatrix} \begin{pmatrix} a_L^* \\ a_R^* \end{pmatrix} = \omega^2 \begin{pmatrix} a_L^* \\ a_R^* \end{pmatrix} \quad \text{(S167)}$$

The 2 $\times$ 2 matrix on the left hand side of equation (S167) is Hermitian, which guarantees the eigenvalues will be real and the eigenvectors will form a complete orthogonal set. Ignoring the term X would prevent strong coupling between Rayleigh and Love waves and would result in the same phase velocity results as reported by Tanimoto (2004) and, to first-order, by Smith & Dahlen (1973).

The solvability condition yields the coupled quasi-Love ($m = 1$) and quasi-Rayleigh wave ($m =$

2) eigenfrequencies

$$\omega^2 = \frac{A + B \pm \sqrt{(A-B)^2 + 4(E^2 + X^2)}}{2} \equiv \frac{1}{2}\left[A + B \pm D\right] \tag{S168}$$

where we assign the higher frequency (i.e., faster wave speed) to the quasi-Love wave and the slower one to the quasi-Rayleigh wave. The strength of coupling depends on the relative size of $4(E^2 + X^2)$ and $(A - B)^2$ in D. We define the coupling strength as follows

$$S = \frac{4(E^2 + X^2)}{(A-B)^2} \tag{S169}$$

To find the eigenvectors of equation (S167) for the quasi-Love wave, associated with eigenvalue $\omega^2 = (A + B + D)/2$, let $a_L^* = 1$ and we find

$$\begin{aligned}
(A - \omega^2) &= -(E + iX)a_R^* \\
a_R^* &= \frac{\omega^2 - A}{E + iX} \cdot \frac{E - iX}{E - iX} = \frac{E(\omega^2 - A)}{E^2 + X^2} - i\frac{X(\omega^2 - A)}{E^2 + X^2} \\
a_R &= \frac{E(B + D - A)}{2(E^2 + X^2)} + i\frac{X(B + D - A)}{2(E^2 + X^2)} = \frac{B + D - A}{2(E^2 + X^2)}(E + iX) = \frac{B - A + D}{2(E^2 + X^2)^{1/2}} e^{i\phi} \\
&= \Gamma e^{i\phi}
\end{aligned} \tag{S170}$$

where $\phi = \tan^{-1}(X/E)$ is the phase lag between the Rayleigh and Love wave components of the quasi-Love wave, which determines whether the particle motion is elliptical or linear. Therefore, we have the following unnormalized eigenvector, which is the polarization vector for the quasi-Love wave;

$$(a_L, a_R)_{qL} = (1, e^{i\phi}(B - A + D)/2(E^2 + X^2)^{1/2})^T \equiv (1, \Gamma e^{i\phi})^T \tag{S171}$$

The vector displacement eigenfunction, therefore, for the quasi-Love wave is

$$\hat{\mathbf{s}}_{qL}(z) = (-\beta W(z) + \alpha\Gamma e^{i\phi}V(z), \alpha W(z) + \beta\Gamma e^{i\phi}V(z) + \alpha W(z), \Gamma e^{i(\phi+\pi/2)}U(z))^T \tag{S172}$$

The polarization vector at the surface ($z = 0$) for the quasi-Love wave is rotated relative to the reference (horizontal, transverse) Love wave polarization by angle Φ in the vertical direction by angle Φ:

$$\tan\Phi = \Gamma\frac{U(0)}{W(0)} = \frac{B - A + D}{2(E^2 + X^2)^{1/2}}\frac{U(0)}{W(0)} \tag{S173}$$

This is directly analogous to the tilt angle for the quasi-S waves given by equation (S44), except for the factor $U(0)/W(0)$ at the end. It can be similarly simplified following equations (S45) - (S51) as

$$\tan 2\Phi = \frac{2(E^2 + X^2)^{1/2}}{A - B}\frac{W(0)}{U(0)} = \sqrt{S}\frac{W(0)}{U(0)} \tag{S174}$$

where S is the coupling strength defined in equation (S169).

To find the eigenvectors for equation (S167) for the quasi-Rayleigh wave, associated with eigenvalue $\omega^2 = (A + B - D)/2$, let $a_R^* = 1$ and we find

$$\begin{aligned}
(B - \omega^2) &= -(E - iX)a_L^* \\
a_L^* &= \frac{\omega^2 - B}{E - iX} \cdot \frac{E + iX}{E + iX} = \frac{E(\omega^2 - B)}{E^2 + X^2} + i\frac{X(\omega^2 - B)}{E^2 + X^2} \\
a_L &= \frac{E(A - D - B)}{2(E^2 + X^2)} - i\frac{X(A - D - B)}{2(E^2 + X^2)} = \frac{A - D - B}{2(E^2 + X^2)}(E - iX) = -\frac{B - A + D}{2(E^2 + X^2)^{1/2}} e^{-i\phi} \\
&= -\Gamma e^{-i\phi}
\end{aligned} \tag{S175}$$

So

$$(a_L, a_R)_{qR} = (-\Gamma e^{-i\phi}, 1) \tag{S176}$$

Therefore, the vector displacement eigenfunction for the quasi-Rayleigh wave is

$$\hat{\mathbf{s}}_{qR}(z) = (\alpha V(z) + \Gamma e^{-i\phi} \beta W(z), \beta V(z) - \alpha \Gamma e^{-i\phi} W(z), iU(z))^T \tag{S177}$$

which is rotated out of the vertical by angle Φ.